RAI Volume 3, Chapter 2.2.1.3.7, First Set, Number 1:

Describe how UZ transport model results support the integration of transport processes in terms of the UZ barrier components and the relative importance of the transport processes.

Basis: Additional information is needed from model results to compare the activity releases from the matrix continuum, the fracture continuum, and faults at the water table and at intermediate locations within the UZ (e.g., base of the TSw, base of the CHn (vitric facies), base of the CHn (zeolitic facies)). The information is needed to verify compliance with 10 CFR 63.114(a) and (b).

1. RESPONSE

The effectiveness of the Lower Natural Barrier is reflected in its capacity to delay the migration of radionuclides through retarding processes such as matrix diffusion, matrix sorption and colloid filtration. The only process within the TSPA-LA model that permanently removes radionuclides from the Lower Natural Barrier is radionuclide decay, which is more effective for those radionuclides with short half-lives. Advection within the unsaturated zone and saturated zone controls the migration of radionuclides through the Lower Natural Barrier and it is the coupling of the aforementioned retarding processes with the advective process that ultimately determines the peak levels of radionuclide releases, the timing of the releases, and the degree to which the mass of radionuclides is reduced by decay. The relative importance of these various unsaturated zone transport processes and their relationship to the capability of the unsaturated zone is described in depth in RAI 3.2.2.1.1-006, which consists of a synthesis of information contained within SAR Section 2.3.8, supplemented by results from TSPA-LA model simulations performed in support of *Total System Performance Assessment Model/Analysis for the License Application (TSPA-LA)* (SNL 2008a). RAI 3.2.2.1.1-006 describes the integration of transport processes in terms of the unsaturated zone barrier components and the relative importance of the transport processes. This RAI response presents additional material that supplements the information presented in RAI 3.2.2.1.1-006 and gives additional insight into the effectiveness of the Lower Natural Barrier and the processes that control it. Specifically, it focuses more on the relative contributions of the unsaturated zone fracture continuum versus the unsaturated zone matrix continuum, as well as how faults and spatial variability of the CHn facies influence radionuclide transport.

This response synthesizes information contained in SAR Sections 2.3.2, 2.3.8, and 2.4, supplemented by results from TSPA-LA model simulations performed in support of *Total System Performance Assessment Model/Analysis for the License Application (TSPA-LA)* (SNL 2008a), but not explicitly presented in the report. The supplemental material is extracted from TSPA-LA model files used to generate results presented in the TSPA-LA (SNL 2008a). Results are extracted for four representative radionuclides, ^{99}Tc, ^{237}Np, ^{242}Pu, and ^{230}Th, representing a broad range of transport characteristics that demonstrate the integration of unsaturated zone transport processes. The extracted results consist of cumulative radionuclide activity releases from the unsaturated zone at the water table separated into releases from unsaturated zone rock matrix versus unsaturated zone fractures to each of the four saturated zone source regions (northeast,

northwest, southeast, and southwest). Cumulative radionuclide activity releases from the Engineered Barrier System (EBS) above the four saturated zone source regions are also presented for comparison with unsaturated zone releases to help discern the directional aspect of radionuclide transport in the unsaturated zone, which is controlled to a large extent by spatial variability in the CHn rock facies. The information presented in the plots contained in this response (Figures 1 through 16) and in the tables (Tables 1 to 5) has not been presented previously, but the results used to generate these figures and tables are available from the TSPA-LA report (SNL 2008a). Additional information, such as particle tracking studies and maps depicting geologic stratigraphy and faults, is included from SAR Section 2.3.8, Section 6 of *Particle Tracking Model and Abstraction of Transport Processes* (SNL 2008c), and Section 6 and Appendix C of *Development for Numerical Grids for UZ Flow and Transport Modeling* (BSC 2004). This additional information is presented to help support conclusions regarding the relative importance of the fracture and matrix continua, as well as the influence of faults and the spatially variable CHn facies.

To show how the unsaturated zone transport model results support the integration of transport processes in terms of the unsaturated zone feature components of the Lower Natural Barrier and the relative importance of the transport processes, activity release plots were generated from EBS and unsaturated zone radionuclide release results that were saved in TSPA-LA Model single-realization simulations (SNL 2008a, Section 7.7.1[a]). The choice to use single-realization simulation files was based on the desire to separate the releases into: (1) results sorted by the four saturated zone source regions (SNL 2008c, Section 6.5.16), and (2) results sorted by the unsaturated zone continua (fracture versus matrix). Single-realization results as described in this response are not representative of the mean system response but are representative of the physical behavior of the system. Therefore, they are appropriate for describing the interaction of the various unsaturated zone components such as the matrix and fracture continua. However, because they are derived from single realizations, the activity releases in the tables and figures of this response cannot be directly compared to the mean activity releases described in SAR Section 2.1 or the different single realizations discussed in RAI 3.2.2.1.1-006. In particular, these realizations are not weighted by probability, so they are not representative of "expected" repository behavior unless the probability of occurrence is considered. It should also be noted that for the specific single realizations discussed below, colloid filtration is not shown to be a controlling process. A more complete discussion of colloid filtration and the nature of its importance in unsaturated zone transport, especially with respect to uncertainty in the fracture retardation coefficient, can be found in RAI 3.2.2.1.1-006.

In the TSPA-LA Model, radionuclide releases from the unsaturated zone are generated and stored as fracture and matrix releases to four saturated zone source regions, northwest, northeast, southwest, and southeast (SNL 2008c, Section 6.5.16 and Figure 6-16, where "1" = NW, "2" = NE, "3" = SW, and "4" = SE). These four saturated zone source regions can be used to evaluate the spatial aspects of the radionuclide transport processes in the unsaturated zone. Based on the areal footprints of the saturated zone source regions described in Section 6.5.16 (SNL 2008c, Figure 6-16), 41% of the repository release nodes are located above the northwest saturated zone release region, 30% of the repository release nodes are located above the northeast saturated zone release region, 28% of the repository release nodes are located above the southwest

saturated zone release region, and 1% of the repository release nodes are located above the southeast saturated zone release region. The repository nodes corresponding to the two southern saturated zone source regions generally overlie the vitric CHn facies (SNL 2008c, Figure 6-16 and BSC 2004, Figures 6-7 and 6-8), which means that repository releases to the southern regions are generally controlled by matrix flow in the CHn vitric rock units. Similarly, the repository nodes corresponding to the northern saturated zone source regions generally overlie the zeolitic CHn facies (SNL 2008c, Figure 6-16 and BSC 2004, Figures 6-7 and 6-8) and repository releases to the northern region are generally controlled by fracture flow to the CHn zeolitic facies, lateral flow to faults and vertical flow in faults. The correspondence between the areal extent of the CHn zeolitic facies and the two northern saturated zone source regions is not exact, since there is small segment of repository release nodes corresponding to the northern saturated zone source regions that overlie the vitric CHn facies (SNL 2008c, Section 6.5.16 and Figure 6-16 and BSC 2004 Figures 6-7 and 6-8). However, the transport processes associated with the relatively larger CHn zeolitic area will overshadow the effects of releases to the small area of repository nodes corresponding to CHn vitric facies above the northern saturated zone source regions

Radionuclide releases from the EBS into the unsaturated zone are presented by percolation subregion or bin (SAR Figure 2.3.8-25). The percolation bins are based on glacial-transition, 10th percentile infiltration map percolation flux rates. Bins based on the glacial-transition, 10^{th} percentile infiltration map percolation flux rates are used because they best represented all the possible infiltration maps (SNL 2008c, Addendum 1, Section 6.5.15). The spatial distribution of the percolation bins with respect to repository release nodes is presented in SAR Figure 2.3.8-25. The bins are defined by percolation rates for the repository horizon of 0.15 to 0.82 mm/yr for Bin 1, 0.82 to 4.55 mm/yr for Bin 2, 4.55 to 14.06 mm/yr for Bin 3, 14.06 to 26.16 mm/yr for Bin 4, and 26.16 to 36.19 mm/yr Bin 5. Because the percolation bins are not confined to contiguous areas, for the following analysis the EBS release results for the five percolation bins are redistributed to four bins that correspond areally to the four saturated zone source regions.

Three of the single realization simulations presented in TSPA-LA (SNL 2008a) analyses were chosen for this analysis: (1) the Igneous Intrusion 1,000,000-Year modeling case (GoldSim realization 2855 of 3000; epistemic realization 286), (2) the Seismic Ground Motion 1,000,000-Year modeling case (GoldSim realization 4641 of 9000; epistemic realization 155), and (3) the Seismic Ground Motion 10,000-Year modeling case (GoldSim realization 4641 of 9000; epistemic realization 155). The specified uncertain transport parameters sampled for these three single-realization cases are presented in Tables 5 and 6. These parameters can be compared to the parameter uncertainty distributions presented in Section 6.5 of *Particle Tracking Model and Abstraction of Transport Processes* (SNL 2008c). In the Igneous Intrusion modeling case studied, all of the waste packages are damaged at the time of the event at 10,000 years, so that the number of waste package failures contributing to releases is 11,629 (SNL 2008a, Section 7.7.1.3[a]). In the 1,000,000-year Seismic Ground Motion modeling case, a seismic event at 24,100 years damages all of the 3,416 codisposal waste packages (SNL 2008a, Section 7.7.1.4[a]). Similarly, all 3,416 codisposal waste packages fail at 1,000 years in the 10,000-year Seismic Ground Motion modeling case (SNL 2008a, Section 7.7.1.7[a]).

The Igneous Intrusion 1,000,000-Year modeling case was chosen because it represents a case where virtually all of the activity released from the EBS enters the unsaturated zone fracture continuum. This is because it is assumed that the drifts are filled with magma and no longer act as a capillary diversion barrier, so that percolation flux is assumed to flow through every waste package. In the EBS flow model all advective flux through the waste package and invert is assumed to enter the fracture continuum. A very small amount of imbibition flux can enter the invert and is assumed to enter the unsaturated zone matrix, which implies that a very small quantity of radionuclide releases from the waste form can enter the unsaturated zone matrix continuum in the Igneous Intrusion case. The Seismic Ground Motion 1,000,000-Year modeling case was chosen because it represents a case where activity releases from the EBS enter the unsaturated zone fracture and matrix continuum. For radionuclides that do not sorb in the invert, the fraction that enters the unsaturated zone fractures is effectively equal to the seepage fraction, which is approximately 70% in this case (compare Table 3a and SAR Table 2.1-9). (Note that the fracture fractions in the northern (69%) and southern (75%) regions are not exactly the same because of the variability in the distribution of the five percolation subregions, as shown in SAR Figure 2.3.8-25.)

The Seismic Ground Motion 10,000-Year modeling case was chosen because it represents a case where, for nonsorbing species (e.g., ^{99}Tc), activity releases from the EBS to the unsaturated zone matrix are larger in magnitude than the releases to the fracture continuum, and are again approximately equal to the seepage fraction, which is 31% before 10,000 years (compare Table 4a and SAR Table 2.1-8). Unlike ^{99}Tc, which does not sorb in the invert, ^{237}Np is weakly sorbing in the invert, with a value equal to the devitrified K_d in Table 6 for this particular realization. Although only weakly sorbing, sorption of ^{237}Np reduces aqueous concentrations in the invert, thereby reducing the rate of diffusion from the invert. As a result, advection of ^{237}Np away from the invert is more prominent, which increases the fraction of the releases that enter the unsaturated zone fractures compared to a nonsorbing species such as ^{99}Tc. In addition, because the simulation time and associated time steps are shorter than for the 1,000,000-year cases, the Seismic Ground Motion 10,000-Year modeling case also allows for an examination of processes affecting the rapid transport times of radionuclides released from the northern part of the repository.

The representative set of radionuclides discussed in this response reflects four groups of radionuclides with varying properties including: (1) highly soluble, nonsorbing radionuclides, with long half-lives represented by ^{99}Tc, (2) low to moderately soluble, weakly sorbing radionuclides, with long half-lives represented by ^{237}Np, (3) low to moderately soluble, moderately-to-strongly sorbing radionuclides, with long half-lives represented by ^{240}Pu, and (4) low-solubility, very strongly sorbing radionuclides, with moderately long half-lives represented by ^{230}Th.

1.1 COMPARISON OF ACTIVITY RELEASES FROM THE EBS WITH ACTIVITY RELEASES AT THE WATER TABLE

This section summarizes the differences in radionuclide transport between the fracture and matrix continua and describes the influence of faults and the spatial distribution of the CHn vitric/zeolitic facies on the fate and transport of radionuclides in the unsaturated zone. The

tabulation of EBS and unsaturated zone activity releases (Tables 2 through 4) presented in this section is based on the cumulative releases at the end of the simulation time, either 10,000 or 1,000,000 years. The complete time histories of cumulative releases for each of the representative radionuclides are presented in Figures 1 through 16. A detailed discussion of the transport of each of these radionuclides through the unsaturated zone for each of the three single-realization cases is presented in Appendix A. Note that in the discussion that follows the EBS releases for the igneous intrusion simulation are not separated by fracture and matrix continua. This is because for the igneous intrusion simulation, the percentage of mass going into the fractures is close to 100%, for the reasons described above. For the igneous intrusion realization, the 500,000-year values for fraction of mass released to the fractures by percolation subregion bin and radionuclide are presented in Table 1.

Table 1. Fraction of Radionuclide Mass from the EBS Going into Unsaturated Zone Fractures at 500,000 Years for the Igneous Intrusion Modeling Case

	Species					
Percolation Subregion	**^{99}Tc**	**^{237}Np**	**^{242}Pu**	**Ic^{242}Pu**	**If^{242}Pu**	**^{230}Th**
Bin 1	1	0.981	0.961	0.997	0.997	0.989
Bin 2	1	0.997	0.997	0.999	0.999	0.998
Bin 3	1	0.998	1	0.999	0.999	0.998
Bin 4	1	0.998	1	0.999	0.999	0.999
Bin 5	1	0.999	1	0.999	0.999	0.999

An examination of EBS and unsaturated zone activity releases with respect to the four saturated zone source regions (northwest, northeast, southwest, and southeast), presented in Figures 1 to 16, shows how structural features within the unsaturated zone control radionuclide migration from the repository to the water table. It also reflects how the influence of transport processes such as advection, matrix diffusion, matrix sorption, and reversible filtration of colloids varies with respect to the spatial distribution of controlling features. Immediately below the repository, radionuclide transport is controlled by fracture flow through the TSw units. Below the northern half of the repository, at the base of the TSw and through the Calico Hills (CHn), the flow domain is controlled by a relatively low-permeability (SNL 2007, Section 6.6.3) zeolitic tuff that supports perched water zones and lateral diversion to faults, which leads to fault dominated vertical flow (SAR Figure 2.1-31 and BSC 2004, Figure 6-7). For releases in the northern half of the repository the lateral transport of the particles to and then through fault zones, such as the Drillhole Wash Fault, Pagany Wash Fault, and Sever Wash Fault, can be inferred by comparing SAR Figure 2.3.8-37a with SAR Figure 2.3.8-37b (SAR Figure 2.3.9-8 to see the fault locations). This lateral transport of radionuclides to and then through the fault zones is also reflected in SAR Table 2.3.2-7, which shows the relative percentages of water flux flowing through the matrix, fracture, and fault continua. In particular, a comparison of the water flux through faults at the repository horizon versus at the water table (as shown in SAR Table 2.3.2-7) indicates the large amount of lateral diversion that happens below the repository.

In the southern half of the repository, at the base of the TSw and through much of the Calico Hills (CHn), the flow process is dominated by matrix flow (SAR Figure 2.1-31 and BSC 2004, Figure 6-7) through vitric nonwelded tuff. In addition, structural features control western to eastern migration of radionuclides. For releases in the southern section of the repository, there exists some structural control via the dipping CHn vitric facies (BSC 2004, Figure C3-2) with a west to east component of flow. This west to east component of flow and transport is found in the central part of the southern region (SAR Figure 2.3.8-37; SNL 2008c, Figure 6.6.2-2) and is reflected in radionuclides moving eastward to a region where transport to the water table is dominantly vertical and generally is not fault controlled, with the exception of some radionuclide transport through the western branch of the Ghost Dance Fault at the southern tip of the repository ("GhostW" in SAR Figure 2.3.9-8).

1.1.1 Northern Releases (Northwest and Northest Regions)

All northern releases (for all three simulations) of ^{99}Tc, ^{237}Np, ^{242}Pu (dissolved and reversibly sorbed onto colloids), ^{230}Th, and ^{242}Pu (irreversible sorbed onto colloids) show that most of the mass from the EBS enters the northwest region repository nodes, and most of the mass leaving the unsaturated zone in the north leaves from the northeast region through the fracture continuum in the fault zones (Figures 1 through 16). This pattern of EBS release and unsaturated zone release is consistent with the conceptual model of fracture transport through the TSw, lateral transport to faults (which mainly traverse the northeast region) due to the low-permeability underlying zeolitic CHn rock units, and vertical transport through the faults to the water table (SAR Section 2.3.8.4.5.1 and associated Figure 2.3.8-37).

For the 1,000,000-year igneous intrusion and seismic ground motion simulations, most of the nonsorbing ^{99}Tc (99% to 100%) and weakly sorbing ^{237}Np (92% to 99%) released from the EBS reaches the water table (Tables 2a, 2b, 3a, and 3b). In addition, there is little retardation seen when comparing the EBS release and unsaturated zone release breakthrough curves for the two species (Figures 1, 2, 7, and 8). These results indicate that the processes of matrix diffusion for ^{99}Tc and coupled matrix diffusion and matrix sorption for ^{237}Np are not important in the north, because advection dominates the transport process. For the moderately-to-strongly sorbing species ^{242}Pu, most of the activity (84% to 92%) reaches the water table within 1,000,000 years (Tables 2a, 2b, 3a, and 3b). In comparison to ^{99}Tc and ^{237}Np transport, the transport of ^{242}Pu through the unsaturated zone reflects an increase in the influence of coupled matrix diffusion and matrix sorption, but advection is still shown to be the dominant controlling factor. For the very strongly sorbing species, ^{230}Th, coupled matrix diffusion and sorption is more effective in delaying and reducing releases to the water table (i.e., only 72% to 77% of EBS activity releases reach the water table within 1,000,000 years) (Tables 2a, 2b, 3a, and 3b). In contrast, most of the ^{242}Pu attached to fast and slow irreversible colloids released from the EBS reaches the water table (Tables 2a, 2b, 3a, and 3b), with little retardation (Figures 5, 6, 11, and 12). This indicates that advection dominates the transport of ^{242}Pu attached to irreversible colloids in the north. The influence of more of the EBS radionuclide release to the unsaturated zone matrix continuum in the 1,000,000-year seismic simulation is not reflected in the comparisons between the igneous and seismic simulations (Tables 2a, 2b, 3a, and 3b) (i.e., the partitioning of unsaturated zone releases between the fracture and matrix continua is about the same for these two modeling cases and almost all of the mass is transported to the water table through the fracture continuum).

Table 2. Total Northern and Southern Activity Released from (a) EBS and (b) Unsaturated Zone for Igneous Intrusion 1,000,000-Year Case at 1,000,000-Years

(a)	Northern Source Regions			Southern Source Regions		
	Total Activity (Ci)	**Fracture**	**Matrix**	**Total Activity (Ci)**	**Fracture**	**Matrix**
^{99}Tc	8.64×10^{5}	99%	1%	3.52×10^{5}	99%	1%
^{237}Np	5.56×10^{4}	100%	0%	2.54×10^{4}	100%	0%
^{242}Pu	2.02×10^{4}	100%	0%	8.96×10^{3}	100%	0%
^{230}Th	2.81×10^{4}	100%	0%	1.48×10^{4}	100%	0%
Slow Irrev ^{242}Pu	6.94×10^{1}	100%	0%	2.23×10^{1}	100%	0%
Fast Irrev ^{242}Pu	1.17×10^{-1}	100%	0%	3.75×10^{-2}	100%	0%

(b)	Northern Source Regions			Southern Source Regions		
	Percent of EBS Activity	**Fracture**	**Matrix**	**Percent of EBS Activity**	**Fracture**	**Matrix**
^{99}Tc	100%	96%	4%	99%	72%	28%
^{237}Np	99%	97%	3%	99%	72%	28%
^{242}Pu	92%	99%	1%	39%	82%	18%
^{230}Th	77%	100%	0%	2%	100%	0%
Slow Irrev ^{242}Pu	100%	98%	2%	99%	74%	26%
Fast Irrev ^{242}Pu	100%	98%	2%	98%	74%	26%

Table 3. Total Northern and Southern Activity Released from (a) EBS and (b) Unsaturated Zone for Seismic Ground Motion 1,000,000-Year Case at 1,000,000-Years

(a)	Northern Source Regions			Southern Source Regions		
	Total Activity (Ci)	**Fracture**	**Matrix**	**Total Activity (Ci)**	**Fracture**	**Matrix**
^{99}Tc	3.21×10^{5}	69%	31%	1.28×10^{5}	75%	25%
^{237}Np	1.69×10^{2}	93%	7%	7.04×10^{1}	94%	6%
^{242}Pu	1.66×10^{3}	95%	5%	6.77×10^{2}	96%	4%
^{230}Th	3.07×10^{1}	100%	0%	1.62×10^{1}	100%	0%
Slow Irrev ^{242}Pu	4.64×10^{2}	100%	0%	2.04×10^{2}	100%	0%
Fast Irrev ^{242}Pu	7.81×10^{-1}	100%	0%	3.44×10^{-1}	100%	0%

(b)	Northern Source Regions			Southern Source Regions		
	Percent of EBS Activity	**Fracture**	**Matrix**	**Percent of EBS Activity**	**Fracture**	**Matrix**
^{99}Tc	99%	95%	5%	98%	74%	26%
^{237}Np	92%	99%	1%	87%	76%	24%
^{242}Pu	84%	100%	0%	19%	80%	20%
^{230}Th	72%	100%	0%	1%	100%	0%
Slow Irrev ^{242}Pu	100%	99%	1%	98%	76%	24%
Fast Irrev ^{242}Pu	100%	99%	1%	98%	76%	24%

Conclusions based upon the results of the 10,000-year seismic ground motion simulation will differ from those for the 1,000,000-year simulations due to the shorter time period and the increased percentage of the EBS releases to the unsaturated zone matrix continuum, as described earlier. Only about 73% of the nonsorbing ^{99}Tc released from the northern repository nodes reaches the water table (Tables 4a and 4b). This moderate reduction in mass over 10,000 years reflects the strong influence of releasing 70% of the radionuclide activity into the unsaturated zone matrix continuum (Table 4a). For the weakly sorbing ^{237}Np, 81% of the mass entering the repository nodes reaches the water table (Tables 4a and 4b). It first seems counterintuitive that there is a higher mass release to the water table for a sorbing radionuclide ^{237}Np (81%) compared to a nonsorbing radionuclide ^{99}Tc (73%); however, the difference is due to the fact that much more of the ^{237}Np EBS mass is released to the fractures (79%) compared to ^{99}Tc EBS releases (only 30% to the fractures), which is caused by ^{237}Np sorption in the invert, as described above.

For the moderately-to-strongly sorbing ^{242}Pu release, which has even more of the total EBS release into the unsaturated zone fractures (90%), 76% of the total EBS activity releases reach the water table in 10,000 years (Tables 4a and 4b). Although a greater percentage of EBS ^{242}Pu goes into the fracture compared to ^{237}Np (90% versus 79%), less ^{242}Pu reaches the water table relative to ^{237}Np. This indicates that the coupled matrix diffusion and matrix sorption process more effectively retards ^{242}Pu compared to ^{237}Np over the 10,000-year time period. For the very strongly sorbing ^{230}Th, most of the mass that reaches the water table is a result of ingrowth from ^{234}U. This is reflected in Tables 4a and 4b, which show a greater total activity reaching the water table (136%) compared to the activity released from the EBS. A more in-depth analysis (Section A.4.4) indicates that for ^{230}Th release alone, with no ingrowth, 57% of the total EBS release reaches the water table. This moderate reduction reflects a smaller influence of applying part of the release to the matrix (relative to^{237}Np and ^{242}Pu) and a greater influence of coupled matrix diffusion and matrix sorption over the shorter time period.

Table 4. Total Northern and Southern Activity Released from the (a) EBS and (b) Unsaturated Zone for Seismic Ground Motion 10,000-Year Case at 10,000-Years[a]

(a)	Northern Source Regions			Southern Source Regions		
	Total Activity (Ci)	**Fracture**	**Matrix**	**Total Activity (Ci)**	**Fracture**	**Matrix**
^{99}Tc	2.57×10^{4}	30%	70%	1.07×10^{4}	32%	68%
^{237}Np	5.24×10^{-4}	79%	21%	2.69×10^{-4}	80%	20%
^{242}Pu	5.59×10^{-4}	90%	10%	2.92×10^{-4}	91%	9%
^{230}Th	5.84×10^{-8}	94%	6%	3.12×10^{-8}	94%	6%

(b)	Northern Source Regions			Southern Source Regions		
	Percent of EBS Activity	**Fracture**	**Matrix**	**Percent of EBS Activity**	**Fracture**	**Matrix**
^{99}Tc	73%	98%	2%	78%	77%	23%
^{237}Np	81%	100%	0%	26%	81%	19%

Table 4. Total Northern and Southern Activity Released from the (a) EBS and (b) Unsaturated Zone for Seismic Ground Motion 10,000-Year Case at 10,000-Years[a] (Continued)

(b)	Northern Source Regions			Southern Source Regions		
	Percent of EBS Activity	Fracture	Matrix	Percent of EBS Activity	Fracture	Matrix
^{242}Pu	76%	100%	0%	2%	100%	0%
^{230}Th	136%	42%	58%	23%	0%	100%

[a] In the single realization study of the 10,000-year Seismic Ground Motion modeling case, the ionic strength inside the failed waste packages generally exceeds 1 molal, which results in unstable colloid suspensions. As a result, colloidal transport in the waste package is limited, and colloid releases from the EBS are not significant from this modeling case. Therefore, for this case colloid releases from the EBS were not partitioned by saturated zone region.

1.1.2 Southern Releases (Southwest and Southest Regions)

All southern releases (for all three simulations) of ^{99}Tc, ^{237}Np, ^{242}Pu (dissolved and reversibly sorbed onto colloids), ^{230}Th, and ^{242}Pu (irreversibly sorbed onto colloids) reflect a pattern of EBS release and unsaturated zone release that indicates that there is a large migration of radionuclides from the southwest to the southeast region during transport through the unsaturated zone (Figures 1 to 16). This migration is reflected in the fact that all releases of radionuclides at the water table from the southeast region are larger in magnitude than the EBS releases to the unsaturated zone in the southeast region. This pattern of EBS release and unsaturated zone release is consistent with the conceptual model of structurally controlled matrix transport through the dipping vitric CHn facies discussed in Section 1.1. Another important facet of radionuclide transport in the southern regions is the dominance of fracture releases compared to matrix releases at the water table (Tables 2 to 4), particularly in the SW. This is because radionuclide mass reaches the water table via downdip transport in the fractured rock underlying the CHn vitric facies (i.e., in the Prow Pass and Bullfrog units). Thus, although the mass exits the CHn vitric into underlying fractured units in the southern region, most of the transport time is spent in the CHn vitric matrix units, so retardation due to matrix diffusion from fractures to matrix does not play a large role in the south.

For the 1,000,000-year igneous intrusion and seismic ground motion single-realization simulations, 98–100% of the nonsorbing ^{99}Tc released from the EBS reaches the water table (Tables 2a, 2b, 3a, and 3b). In addition, there is little retardation seen when comparing the EBS release and unsaturated zone release breakthrough curves for ^{99}Tc (Figures 1 and 7). These results indicate that the process of matrix diffusion for ^{99}Tc is not very important in the south and advection dominates the transport process. This is as expected because in the south, unsaturated zone transport is dominated by matrix flow in the vitric CHn units.

For the 1,000,000-year igneous intrusion simulation, 99% of the weakly sorbing ^{237}Np released from the EBS reaches the water table (Tables 2a and 2b). In addition, there is only a small retardation seen when comparing the EBS release and unsaturated zone release breakthrough curves for ^{237}Np (Figure 2). These results indicate that the process of matrix sorption for ^{237}Np is not very important in the south for this realization, and advection dominates the transport process.

For the 1,000,000-year seismic ground motion simulation, it can be seen that 87% of the weakly sorbing ^{237}Np released from the EBS reaches the water table (Tables 3a and 3b). In addition, there is only a small retardation seen when comparing the EBS release and unsaturated zone release breakthrough curves for ^{237}Np (Figure 8). These results indicate that the process of matrix sorption for ^{237}Np has a minor influence for this realization where the sampled neptunium K_d is higher (Table 6) than for the sampled neptunium K_d in the igneous intrusion case.

For the moderately-to-strongly sorbing species ^{242}Pu in the 1,000,000-year igneous intrusion and seismic ground motion simulations, matrix sorption is more effective in delaying and reducing releases to the water table, with only about 19% to 39% of the total EBS release reaching the water table within 1,000,000 years (Tables 2a, 2b, 3a, and 3b). The release of ^{242}Pu into the southwest region of the unsaturated zone is highly retarded (Figures 3 and 9). This reduction in activity and delay of the release reflects a strong influence of coupled matrix diffusion and matrix sorption.

In the 1,000,000-year igneous and seismic simulations for the very strongly sorbing species ^{230}Th, matrix sorption is very effective in reducing and delaying activity releases to the water table, with only about 1% to 2% of the EBS activity reaching the water table within 1,000,000 years (Tables 2a, 2b, 3a, and 3b). Like ^{242}Pu, the release of ^{230}Th mass into the southwest region of the unsaturated zone is highly retarded (Figures 4 and 10), reflecting the strong influence of matrix sorption on the transport.

Most of the ^{242}Pu attached to irreversible colloids released from the EBS, whether subject to colloid filtration (slow colloids) or not (fast colloids), reaches the water table (Tables 2a, 2b, 3a, and 3b). In addition there is little retardation seen when comparing the EBS release and unsaturated zone release breakthrough curves for either the slow or fast colloids (Figures 5, 6, 11, and 12). This indicates that advection through the CHn vitric matrix dominates the transport of ^{242}Pu attached to irreversible colloids in the south because there is no filtration or retardation of colloids in the matrix units.

For the southern releases, conclusions based upon the results of the 10,000-year seismic ground motion simulation will differ from those for the 1,000,000-year simulations due to the shorter time period of the analysis. In contrast to releases in the north, the increased percentage of the EBS releases entering the unsaturated zone matrix continuum is not important in the south, as shown in SAR Figure 2.3.8-49. About 78% of the nonsorbing ^{99}Tc release from the southern repository nodes reaches the water table (Tables 4a and 4b). This moderate reduction in activity reaching the water table over 10,000 years reflects the slower interstitial flow rates in the CHn vitric unit matrix. For the weakly sorbing ^{237}Np release in the south, only 26% of the activity entering the repository nodes reaches the water table (Tables 4a and 4b). This large reduction reflects a moderate to strong influence of matrix sorption over the shorter 10,000-year time period. The influence of matrix sorption can also be seen in a small delay between the EBS and unsaturated zone release breakthrough curves (Figure 14). For the moderately-to-strongly sorbing ^{242}Pu release, only 2% of the activity entering the repository nodes reaches the water table (Tables 4a and 4b). This large reduction, along with a large delay in the unsaturated zone breakthrough curve in the southwest region (Figure 15), reflects the large influence of matrix sorption over the shorter 10,000-year time period. For the very strongly sorbing ^{230}Th, only

about 0.03% of the EBS activity released reaches the water table, if the effects of ingrowth are removed (Section A.2.4). This large reduction, along with a large delay in the unsaturated zone breakthrough curve in the southwest region (Figure 16), reflects the large influence of matrix sorption over the shorter 10,000-year time period.

1.2 SUMMARY

The relative importance of the various unsaturated zone transport processes and their relationship to the capability of the unsaturated zone is described in depth in RAI 3.2.2.1.1-006. RAI 3.2.2.1.1-006 describes the integration of transport processes in terms of the unsaturated zone barrier components and the relative importance of the transport processes. This RAI response presents additional material that supplements the information presented in RAI 3.2.2.1.1-006 and gives additional insight into the effectiveness of the Lower Natural Barrier and the processes that control it. Specifically, it focuses more on the relative contributions of the unsaturated zone fracture continuum versus the unsaturated zone matrix continuum, as well as how faults and spatial variability of the CHn facies influence radionuclide transport. It is based on results from three TSPA-LA Model single-realization simulations (SNL 2008a, Section 7.7.1[a]), which are representative of the physical behavior of the system. However, because they are derived from single realizations, the activity releases in the tables and figures of this response cannot be directly compared to the mean activity releases described in SAR Section 2.1 or the different single realizations discussed in RAI 3.2.2.1.1-006.

An examination of EBS and unsaturated zone activity releases from the fracture and matrix continua with respect to the four saturated zone source regions (northwest, northeast, southwest, and southeast), presented in Figures 1 to 16, shows how structural features within the unsaturated zone control radionuclide migration from the repository to the water table. It also reflects how the influence of transport processes such as advection, matrix diffusion, and matrix sorption varies with respect to the spatial distribution of controlling features. Immediately below the repository, radionuclide transport is controlled by fracture flow through the TSw units. Below the northern half of the repository, at the base of the TSw and through the Calico Hills (CHn), the flow domain is controlled by a relatively low-permeability zeolitic tuff that supports perched water zones and lateral diversion to faults, which leads to fault-dominated vertical flow. In the southern half of the repository, at the base of the TSw and through much of the Calico Hills (CHn), the flow process is dominated by matrix flow through vitric nonwelded tuff. In addition, structural features in the south control western to eastern migration of radionuclides (e.g., there exists some structural control via the dipping CHn vitric facies). Note that that for the specific single realizations examined here, colloid filtration was not shown to be a controlling process. As mentioned above, a more complete discussion of colloid filtration and the nature of its importance in unsaturated zone transport, especially with respect to uncertainty in the fracture retardation coefficient, can be found in RAI 3.2.2.1.1-006.

Table 5. Sampled Uncertain Parameter Values for the Selected Scenarios

Uncertain Parameter Description	Seismic Ground Motion 10,000-Year[a] 1,000,000-Year[b]	Igneous Intrusion 1,000,000-Year[c]
Infiltration State	30th percentile Infiltration Scenario	50th percentile Infiltration Scenario
Unsaturated Zone Colloid Retardation Factor	35.778	19.275
Unsaturated Zone Active Fracture Model Gamma Parameter	0.48074	0.35724
Fracture Aperture for Group 1 (chnf) rock units	0.0063289	0.0026041
Fracture Aperture for Group 2 (tswf) Rock Units	0.016973	0.01737
Fracture Aperture for Group 3 (ch[2,3,4,5]fz, pcf[2,5]z, pp4fz, pp1fz, bf2fz, tr2fz) Rock Units	0.0042274	0.010931
Fracture Aperture for Group 4 (pp3fd, pp2fd, bf3fd, tr3fd) rock units	0.023736	0.013363
Fracture Aperture for Group 5 (ch1fz, pcf1z, ch6fz, pcf6z) Rock Units	0.0028411	0.0077021
Fracture Aperture for Group 6 (ch[1,2,3,4,5,6]fv) Rock Units	0.0041046	0.003766
Fracture Aperture for Group 7 (tswf9, pcf39, tswfv, tswfz) Rock Units	0.0030229	0.0045382
Fracture Aperture for Group 8 (tswf[4,5], tswf[6,7], tswf8, pcf38) Rock Units	0.0040874	0.011267
Fracture Aperture for Group 9 (tswf3) Rock Units	0.033976	0.0025931

Table 6. Sampled Uncertain Parameter Values for Various Radionuclides for the Selected Scenarios

Species (Decay Rate)	Parameter	Rock Type	Seismic Ground Motion 10,000-Year[a] and 1,000,000-Year[b] Sampled Value	Igneous Intrusion 1,000,000-Year[c] Sampled Value
^{99}Tc (2.13×10^5 yrs)	Sorption Coefficient (ml/g)	Zeolitic Rock	0.0	0.0
		Devitrified Rock	0.0	0.0
		Vitric Rock	0.0	0.0
	Matrix Diffusion Coefficient (m^2/s)	Rock Group 1	2.27×10^{-10}	2.52×10^{-10}
		Rock Group 2	1.07×10^{-10}	1.84×10^{-11}
		Rock Group 3	1.85×10^{-11}	2.78×10^{-11}
^{237}Np (2.14×10^6 yrs)	Sorption Coefficient (ml/g)	Zeolitic Rock	3.643	1.4717
		Devitrified Rock	3.643	1.4717
		Vitric Rock	2.1429	1.3534
	Matrix Diffusion Coefficient (m^2/s)	Rock Group 1	7.21×10^{-11}	7.98×10^{-11}
		Rock Group 2	3.41×10^{-11}	5.83×10^{-12}
		Rock Group 3	5.88×10^{-12}	8.80×10^{-12}
^{242}Pu (3.75×10^5 yrs)	Sorption Coefficient (ml/g)	Zeolitic Rock	137.56	180.32
		Devitrified Rock	118.83	174.41
		Vitric Rock	137.56	180.32
	Matrix Diffusion Coefficient (m^2/s)	Rock Group 1	1.52×10^{-10}	1.68×10^{-10}
		Rock Group 2	7.17×10^{-11}	1.23×10^{-11}
		Rock Group 3	1.24×10^{-11}	1.85×10^{-11}
^{230}Th (7.54×10^4 yrs)	Sorption Coefficient (ml/g)	Zeolitic Rock	19760	23914
		Devitrified Rock	6822.1	8111.4
		Vitric Rock	6822.1	8111.4
	Matrix Diffusion Coefficient (m^2/s)	Rock Group 1	6.96×10^{-11}	7.71×10^{-11}
		Rock Group 2	3.29×10^{-11}	5.63×10^{-12}
		Rock Group 3	5.68×10^{-12}	8.50×10^{-12}

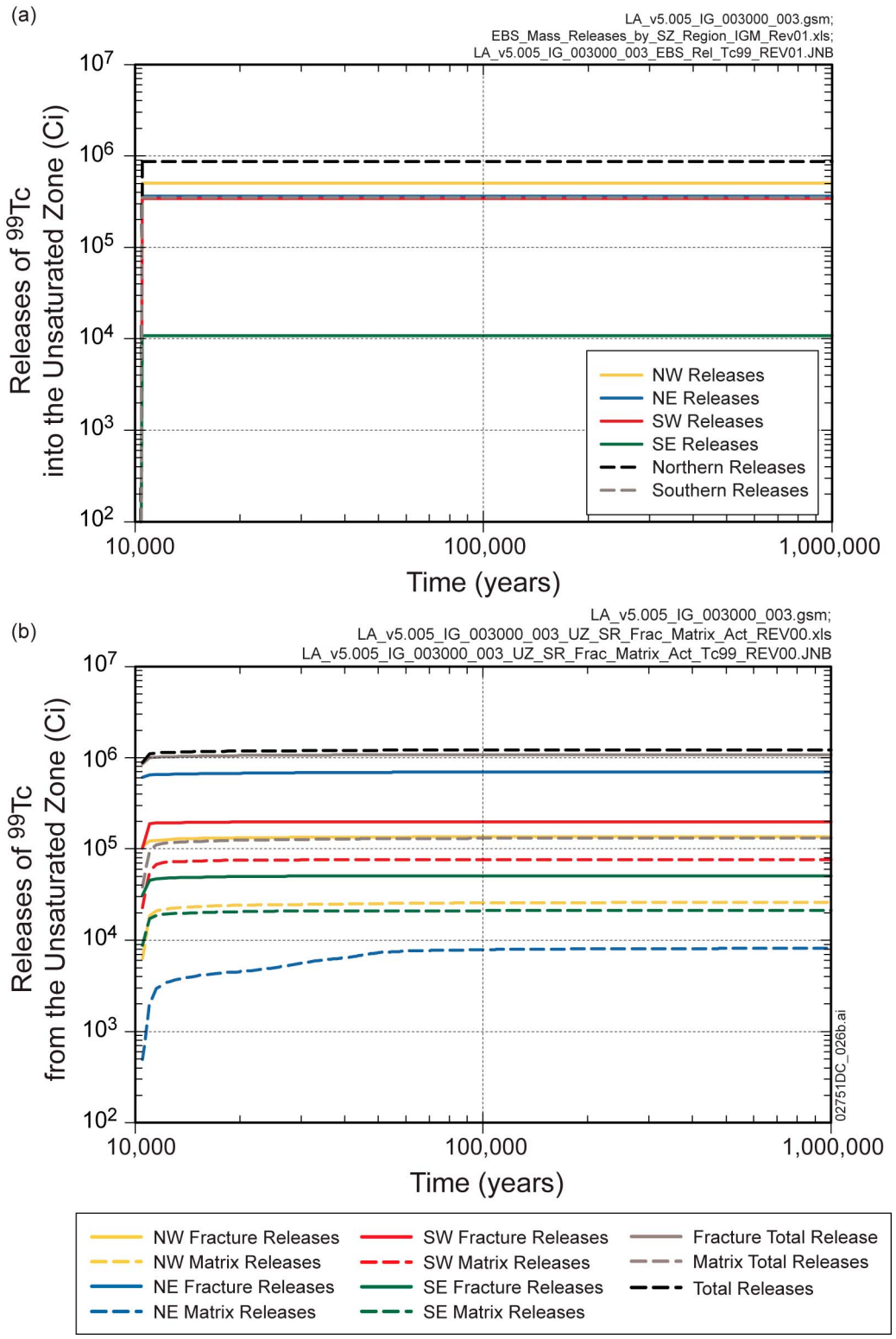

Figure 1. Total ^{99}Tc Activity Released for the Igneous Intrusion 1,000,000-Year Single-Realization Case from the (a) NW, NE, SW, SE, Combined Northern, and Combined Southern Regions of the Repository, and (b) NW, NE, SW, and SE Saturated Zone Source Regions Divided into Unsaturated Zone Fracture and Matrix Continua

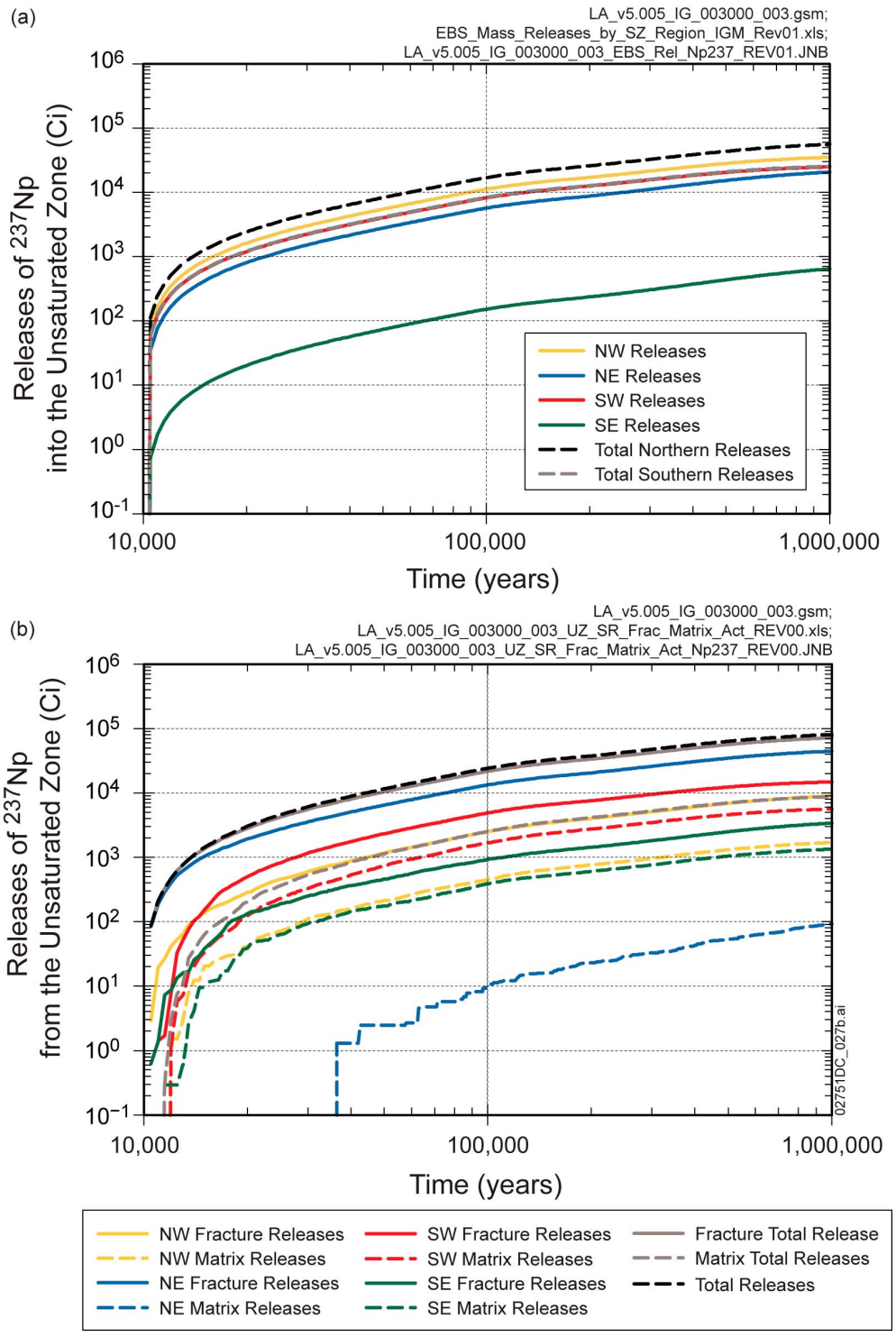

Figure 2. Total ^{237}Np Activity Released for the Igneous Intrusion 1,000,000-Year Single-Realization Case from the (a) NW, NE, SW, SE, Combined Northern, and Combined Southern Regions of the Repository, and (b) NW, NE, SW, and SE Saturated Zone Source Regions Divided into Unsaturated Zone Fracture and Matrix Continua

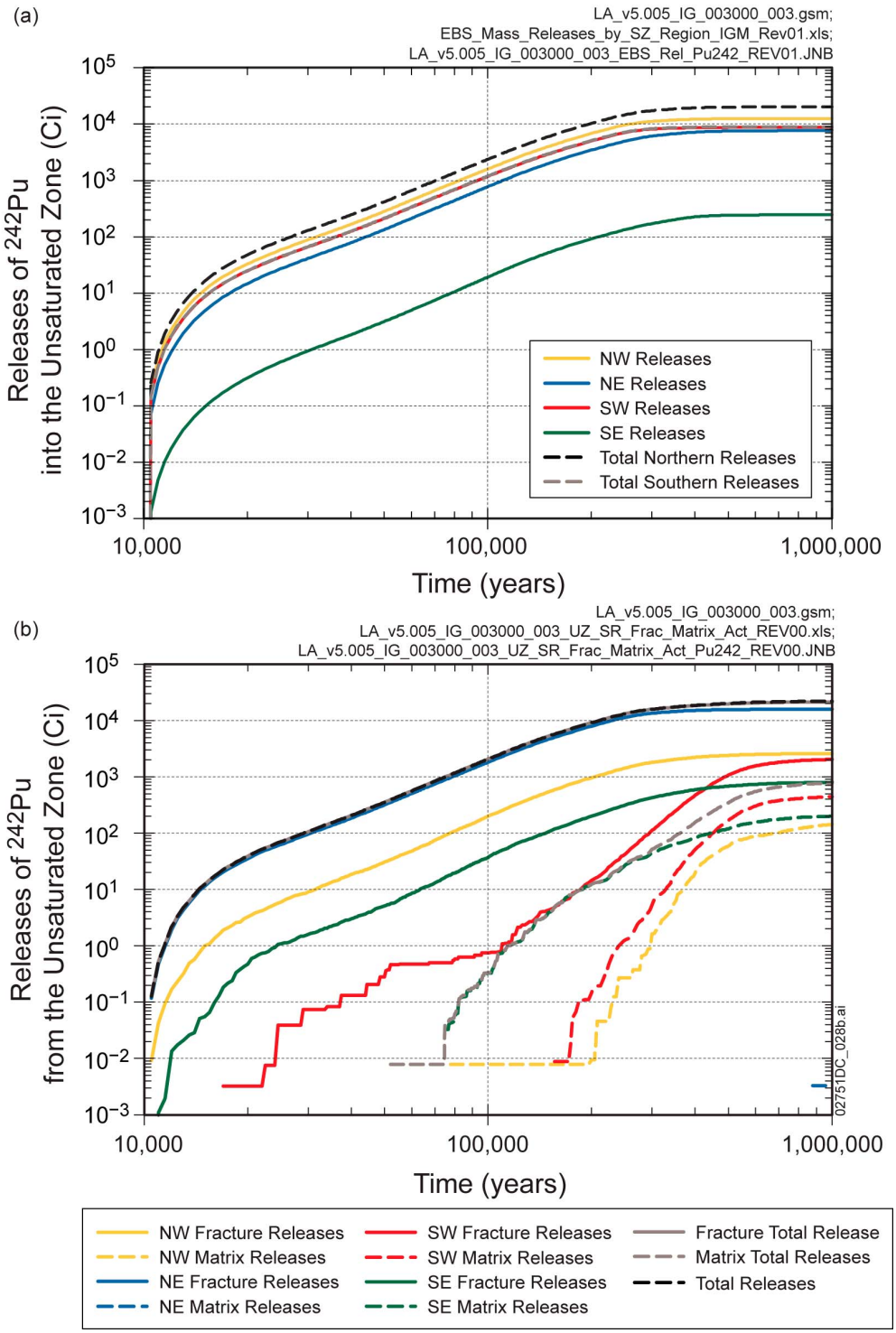

Figure 3. Total ^{242}Pu Activity Released for the Igneous Intrusion 1,000,000-Year Single-Realization Case from the (a) NW, NE, SW, SE, Combined Northern, and Combined Southern Regions of the Repository, and (b) NW, NE, SW, and SE Saturated Zone Source Regions Divided into Unsaturated Zone Fracture and Matrix Continua

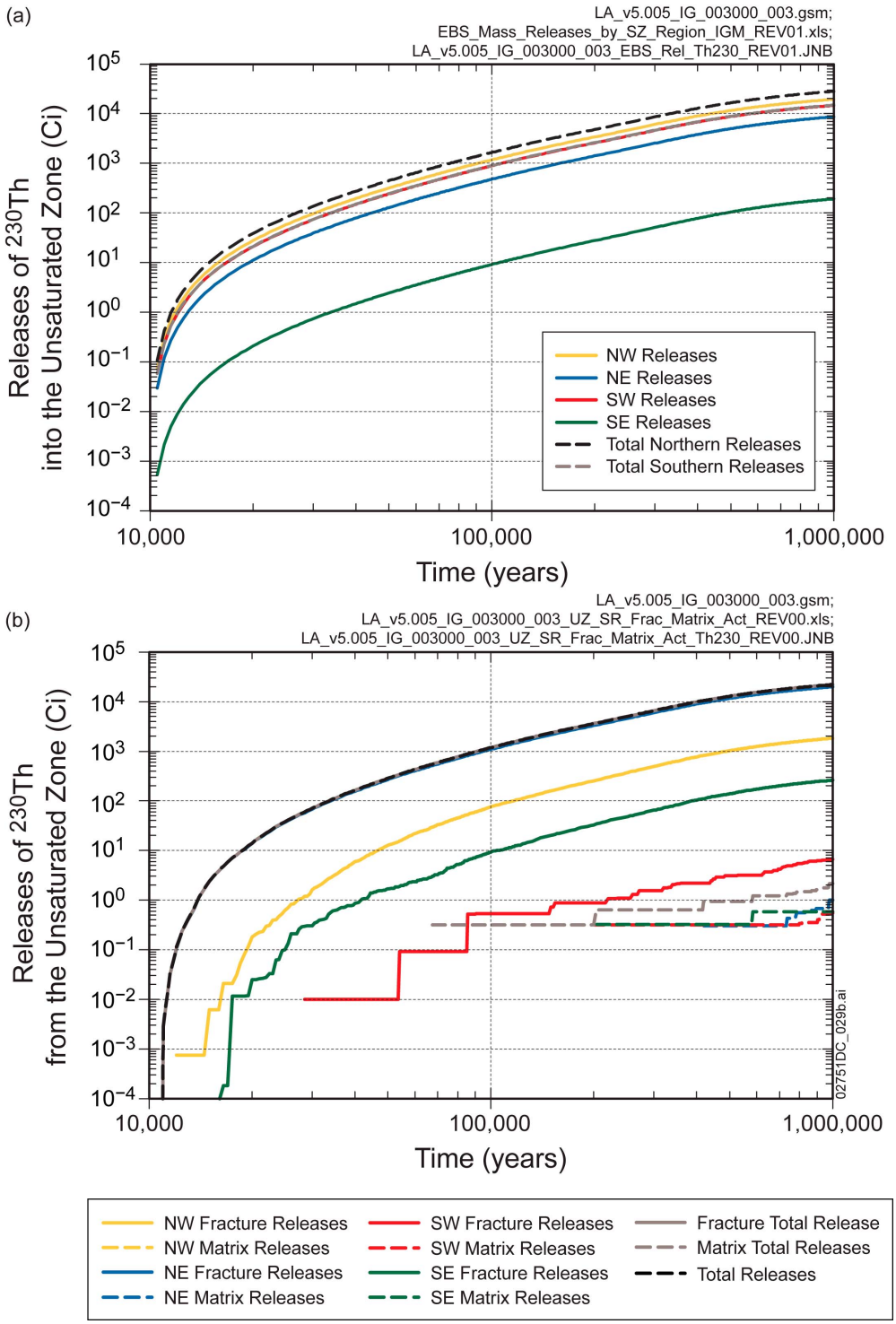

Figure 4. Total ^{230}Th Activity Released for the Igneous Intrusion 1,000,000-Year Single-Realization Case from the (a) NW, NE, SW, SE, Combined Northern, and Combined Southern Regions of the Repository, and (b) NW, NE, SW, and SE Saturated Zone Source Regions Divided into Unsaturated Zone Fracture and Matrix Continua

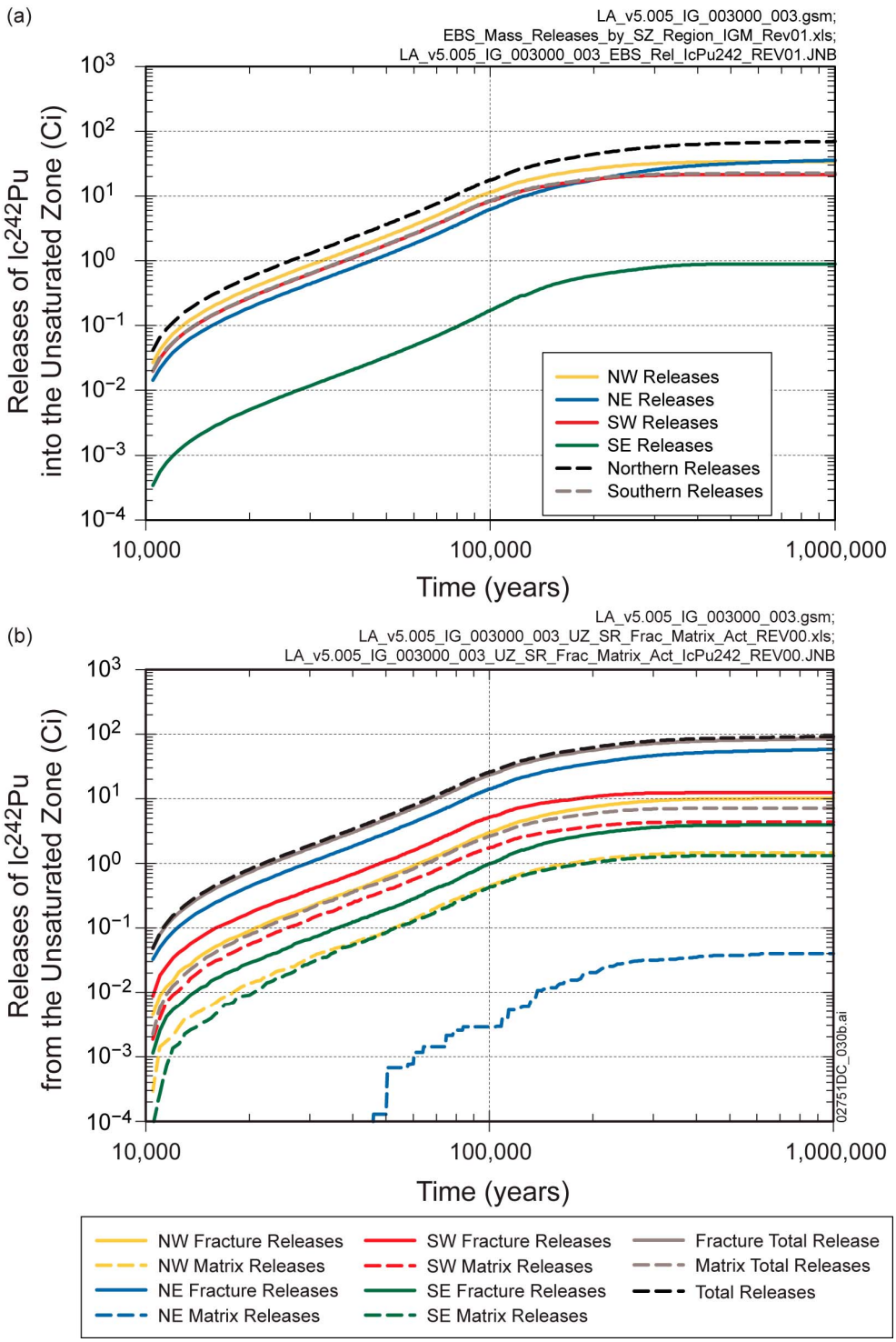

Figure 5. Total ^{242}Pu (irreversibly sorbed onto colloids and subject to filtration) Activity Released for the Igneous Intrusion 1,000,000-Year Single-Realization Case from the (a) NW, NE, SW, SE, Combined Northern, and Combined Southern Regions of the Repository, and (b) NW, NE, SW, and SE Saturated Zone Source Regions Divided into Unsaturated Zone Fracture and Matrix Continua

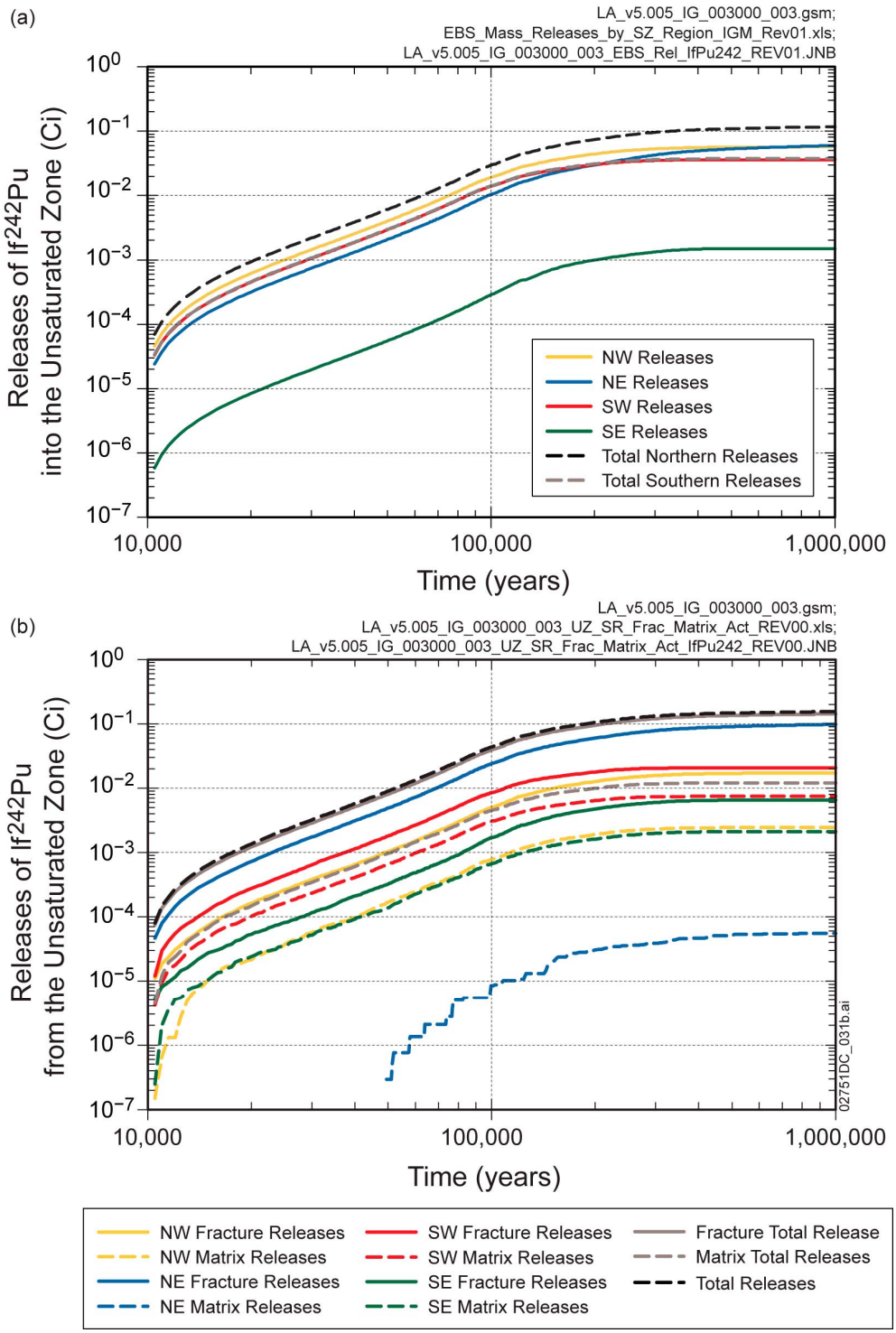

Figure 6. Total ^{242}Pu (irreversibly sorbed onto colloids and not subject to filtration) Activity Released for the Igneous Intrusion 1,000,000-Year Single-Realization Case from the (a) NW, NE, SW, SE, Combined Northern, and Combined Southern Regions of the Repository, and (b) NW, NE, SW, and SE Saturated Zone Source Regions Divided into Unsaturated Zone Fracture and Matrix Continua

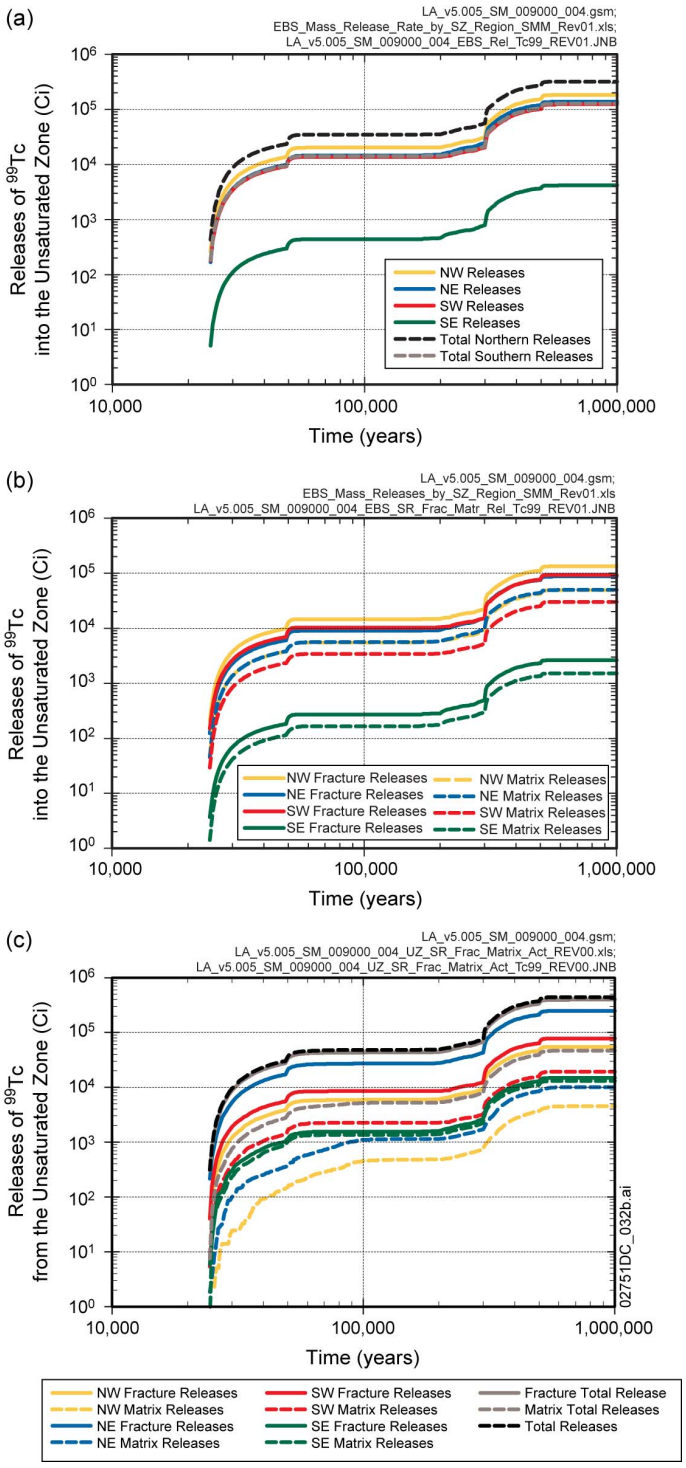

Figure 7. Total ^{99}Tc Activity Released for the Seismic Ground Motion 1,000,000-Year Single-Realization Case from the (a) NW, NE, SW, SE, Combined Northern, and Combined Southern Regions of the Repository, (b) NW, NE, SW, and SE Regions of the Repository Divided into Unsaturated Zone Fracture and Matrix Continuums, and (c) NW, NE, SW, and SE Saturated Zone Source Regions Divided into Unsaturated Zone Fracture and Matrix Continua

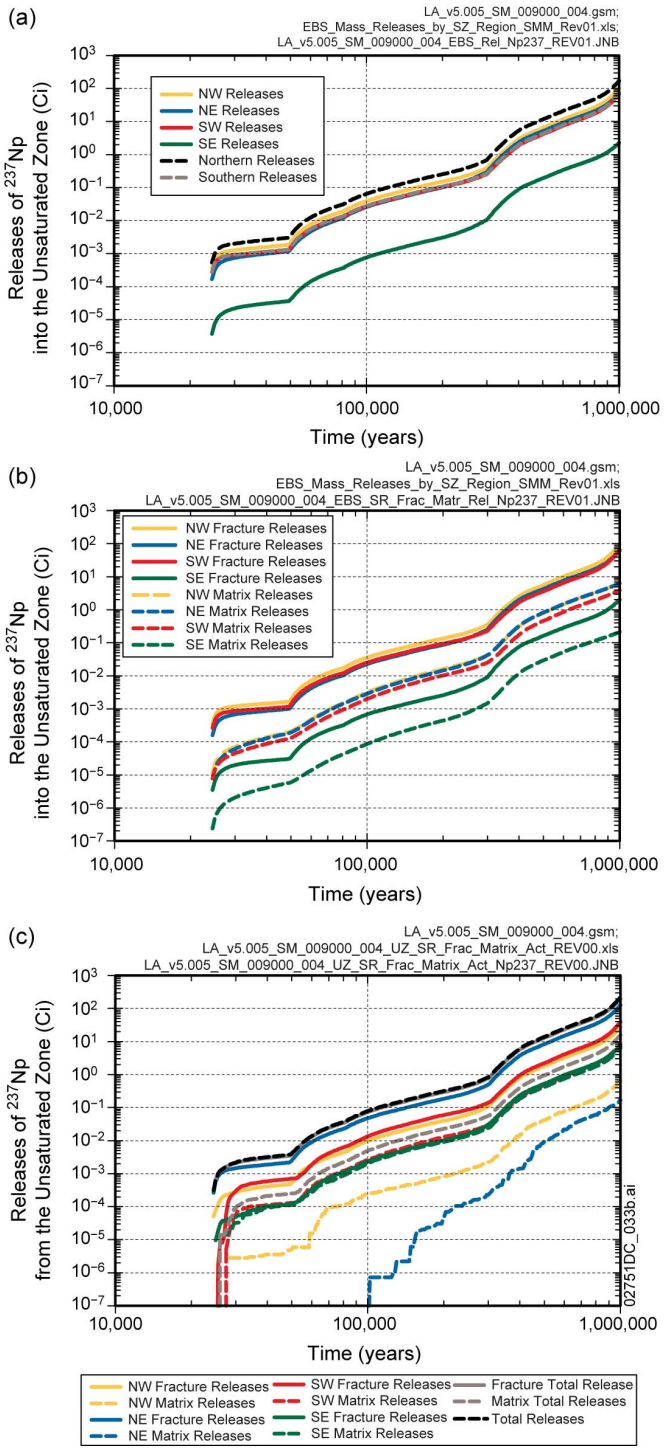

Figure 8. Total ^{237}Np Activity Released for the Seismic Ground Motion 1,000,000-Year Single-Realization Case from the (a) NW, NE, SW, SE, Combined Northern, and Combined Southern Regions of the Repository, (b) NW, NE, SW, and SE Regions of the Repository Divided into Unsaturated Zone Fracture and Matrix Continuums, and (c) NW, NE, SW, and SE Saturated Zone Source Regions Divided into Unsaturated Zone Fracture and Matrix Continua

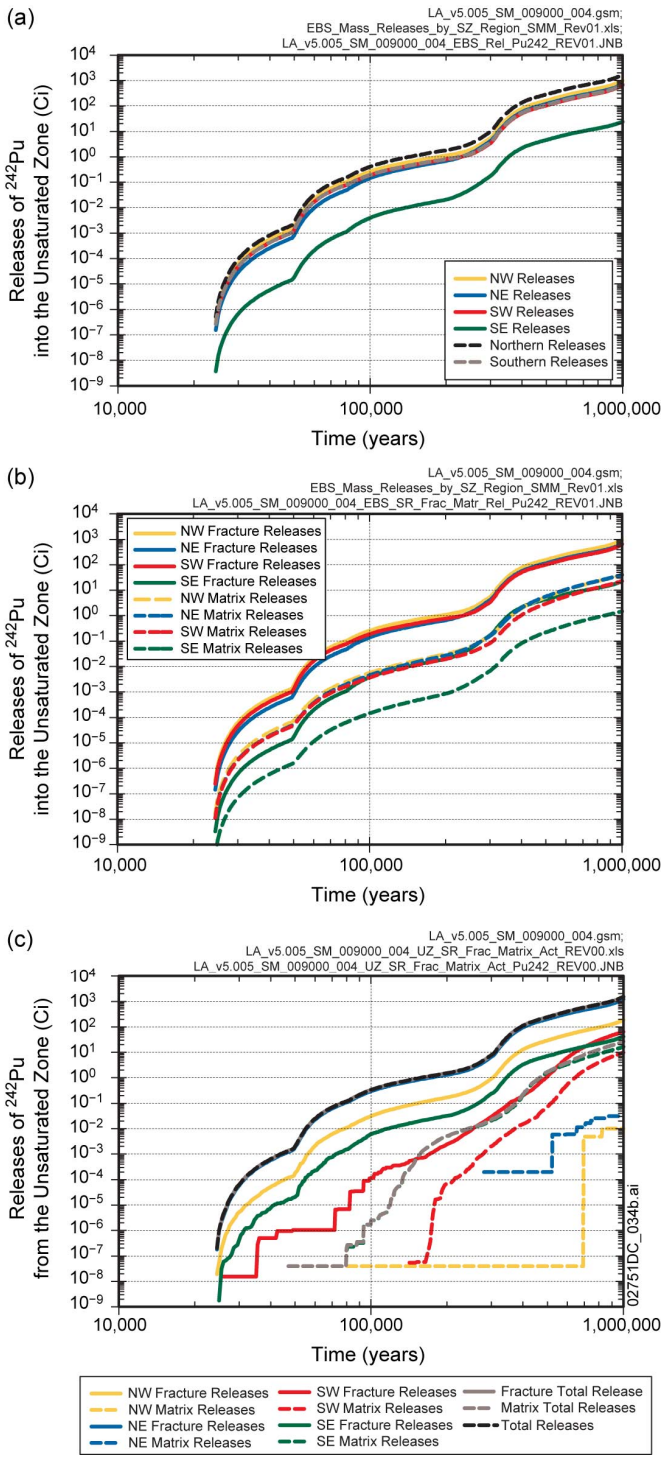

Figure 9. Total ^{242}Pu Activity Released for the Seismic Ground Motion 1,000,000-Year Single-Realization Case from the (a) NW, NE, SW, SE, Combined Northern, and Combined Southern Regions of the Repository, (b) NW, NE, SW, and SE Regions of the Repository Divided into Unsaturated Zone Fracture and Matrix Continuums, and (c) NW, NE, SW, and SE Saturated Zone Source Regions Divided into Unsaturated Zone Fracture and Matrix Continua

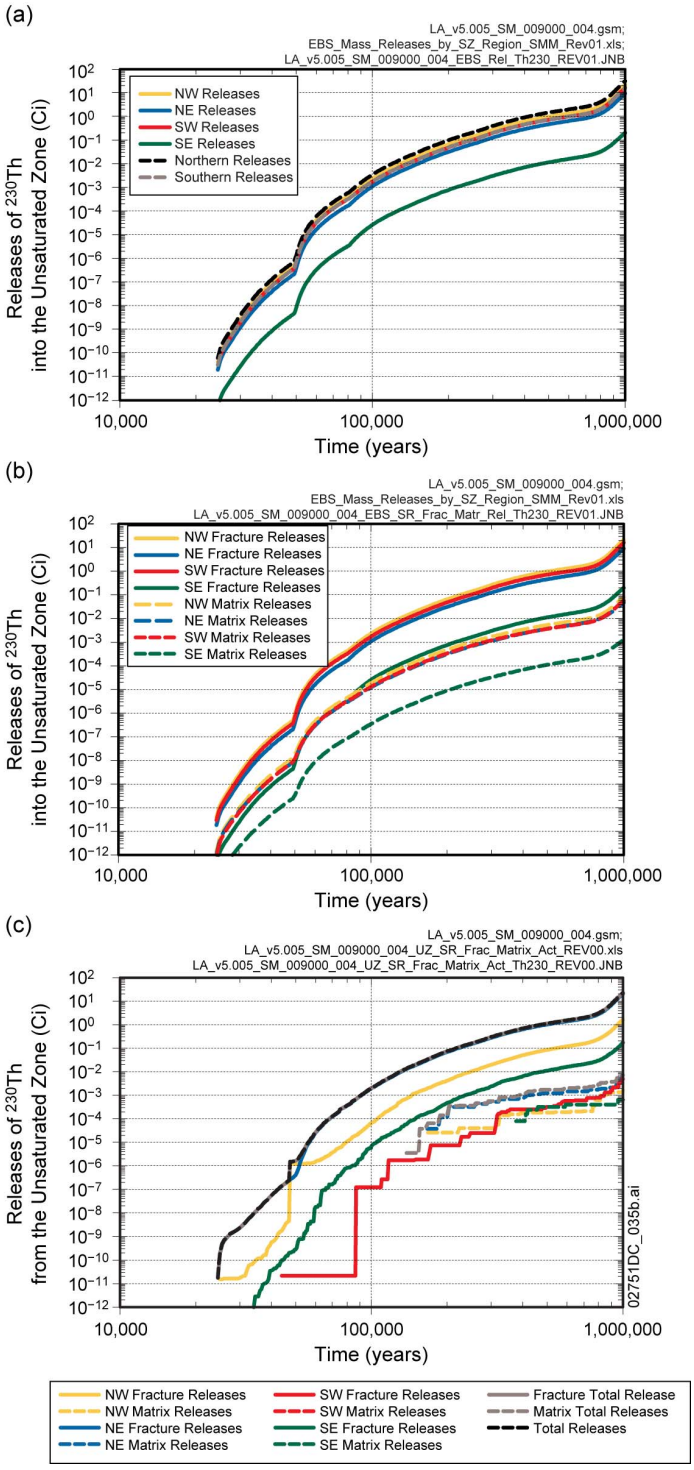

Figure 10. Total ^{230}Th Activity Released for the Seismic Ground Motion 1,000,000-Year Single-Realization Case from the (a) NW, NE, SW, SE, Combined Northern, and Combined Southern Regions of the Repository, (b) NW, NE, SW, and SE Regions of the Repository Divided into Unsaturated Zone Fracture and Matrix Continuums, and (c) NW, NE, SW, and SE Saturated Zone Source Regions Divided into Unsaturated Zone Fracture and Matrix Continua

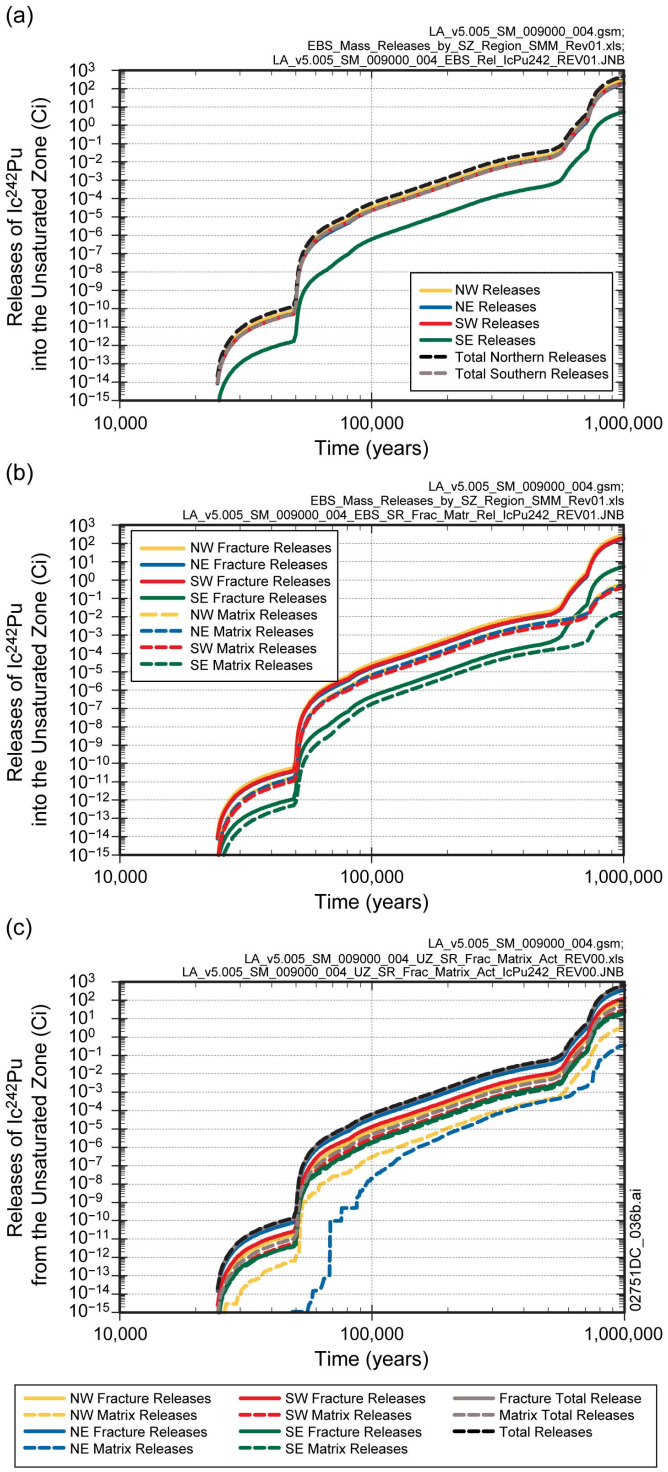

Figure 11. Total ^{242}Pu (irreversibly sorbed onto colloids and subject to filtration) Activity Released for the Seismic Ground Motion 1,000,000-Year Single-Realization Case from the (a) NW, NE, SW, SE, Combined Northern, and Combined Southern Regions of the Repository, (b) NW, NE, SW, and SE Regions of the Repository Divided into Unsaturated Zone Fracture and Matrix Continuums, and (c) NW, NE, SW, and SE Saturated Zone Source Regions Divided into Unsaturated Zone Fracture and Matrix Continua

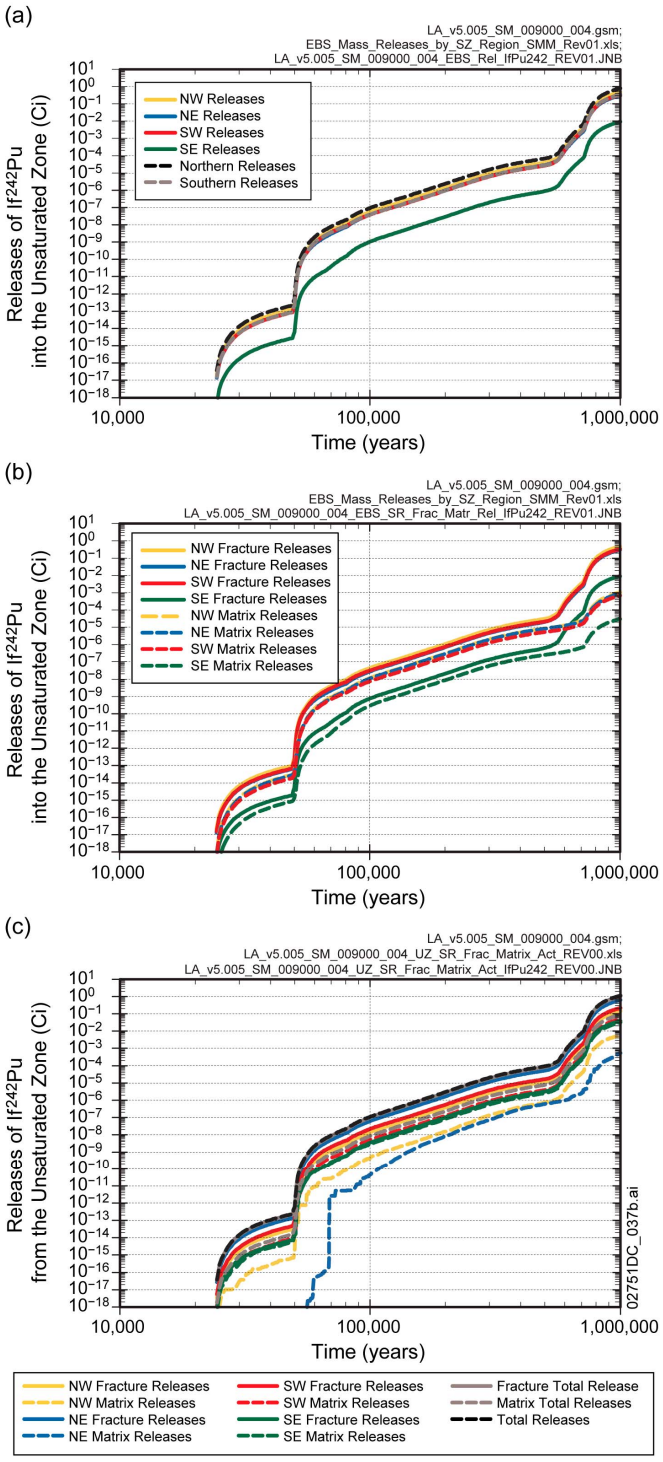

Figure 12. Total ^{242}Pu (irreversibly sorbed onto colloids and not subject to filtration) Activity Released for the Seismic Ground Motion 1,000,000-Year Single-Realization Case from the (a) NW, NE, SW, SE, Combined Northern, and Combined Southern Regions of the Repository, (b) NW, NE, SW, and SE Regions of the Repository Divided into Unsaturated Zone Fracture and Matrix Continuums, and (c) NW, NE, SW, and SE Saturated Zone Source Regions Divided into Unsaturated Zone Fracture and Matrix Continua

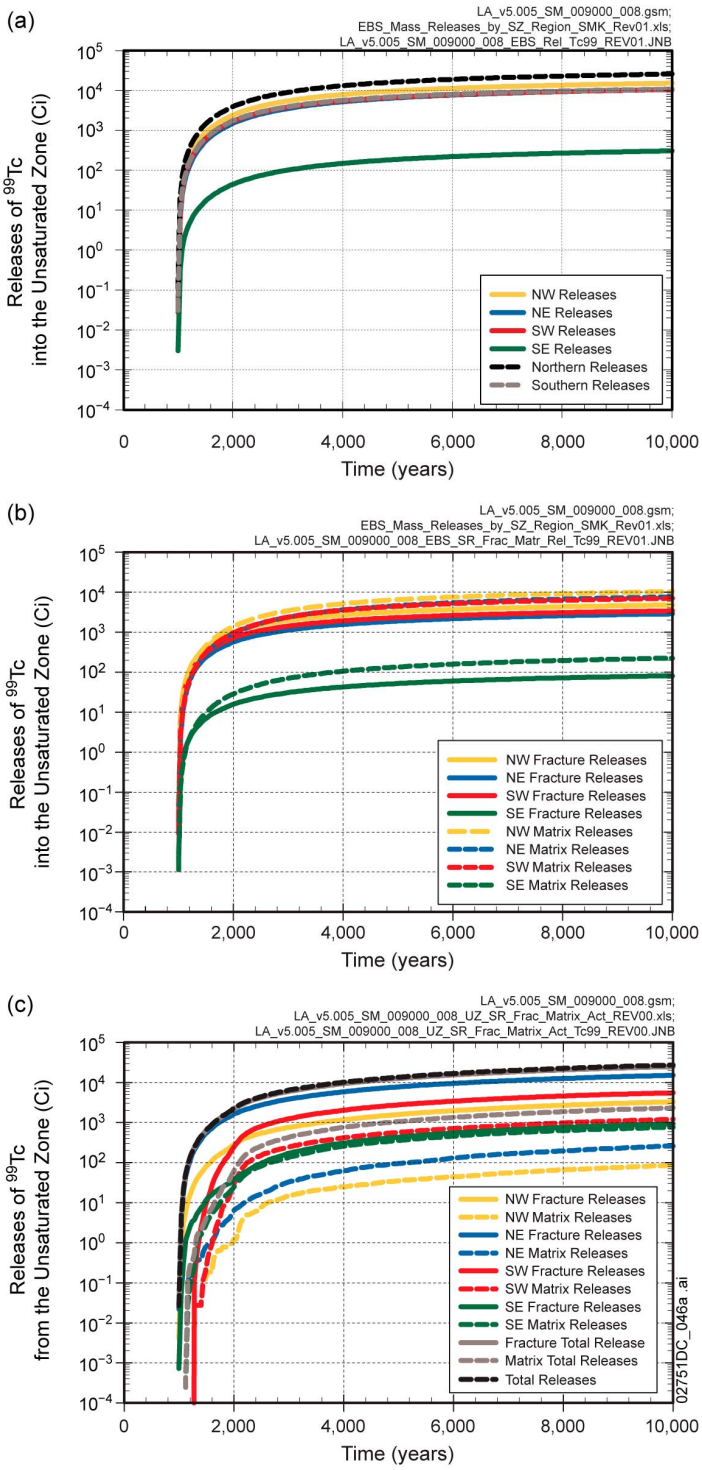

Figure 13. Total ^{99}Tc Activity Released for the Seismic Ground Motion 10,000-Year Single-Realization Case from the (a) NW, NE, SW, SE, Combined Northern, and Combined Southern Regions of the Repository, (b) NW, NE, SW, and SE Regions of the Repository Divided into Unsaturated Zone Fracture and Matrix Continuums, and (c) NW, NE, SW, and SE Saturated Zone Source Regions Divided into Unsaturated Zone Fracture and Matrix Continua

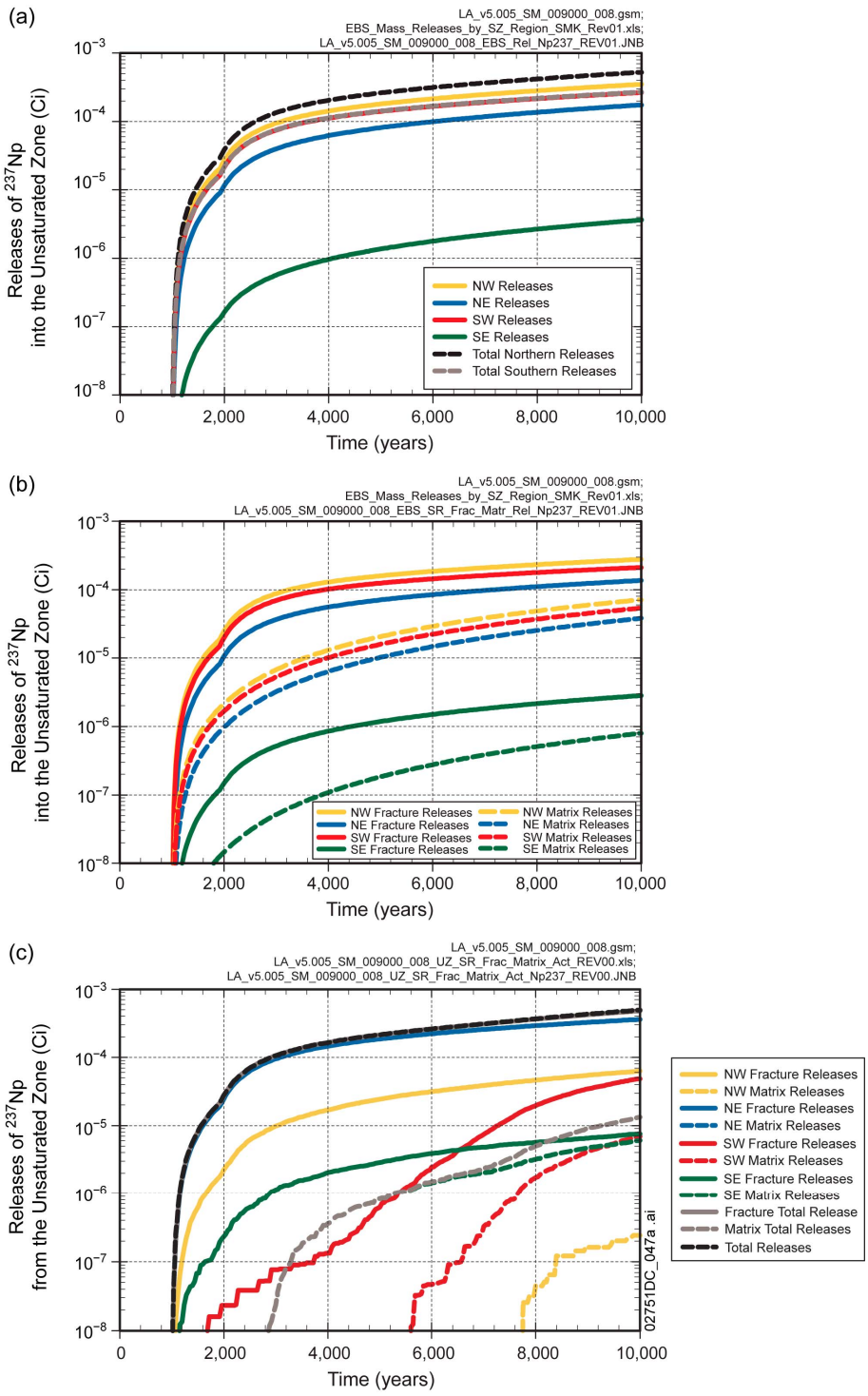

Figure 14. Total ^{237}Np Activity Released for the Seismic Ground Motion 10,000-Year Single-Realization Case from the (a) NW, NE, SW, SE, Combined Northern, and Combined Southern Regions of the Repository, (b) NW, NE, SW, and SE Regions of the Repository Divided into Unsaturated Zone Fracture and Matrix Continuums, and (c) NW, NE, SW, and SE Saturated Zone Source Regions Divided into Unsaturated Zone Fracture and Matrix Continua

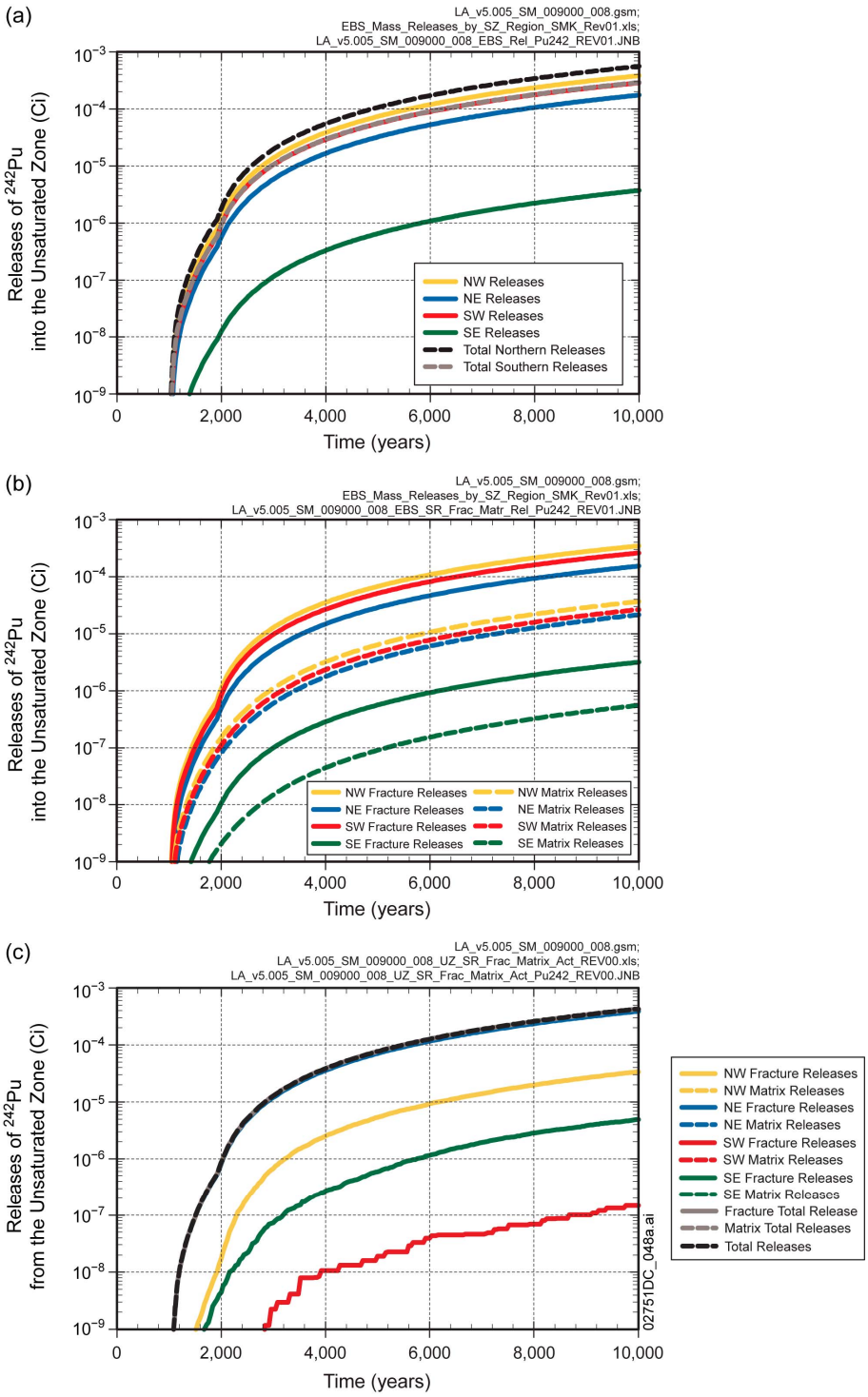

Figure 15. Total ^{242}Pu Activity Released for the Seismic Ground Motion 10,000-Year Single-Realization Case from the (a) NW, NE, SW, SE, Combined Northern, and Combined Southern Regions of the Repository, (b) NW, NE, SW, and SE Regions of the Repository Divided into Unsaturated Zone Fracture and Matrix Continuums, and (c) NW, NE, SW, and SE Saturated Zone Source Regions Divided into Unsaturated Zone Fracture and Matrix Continua

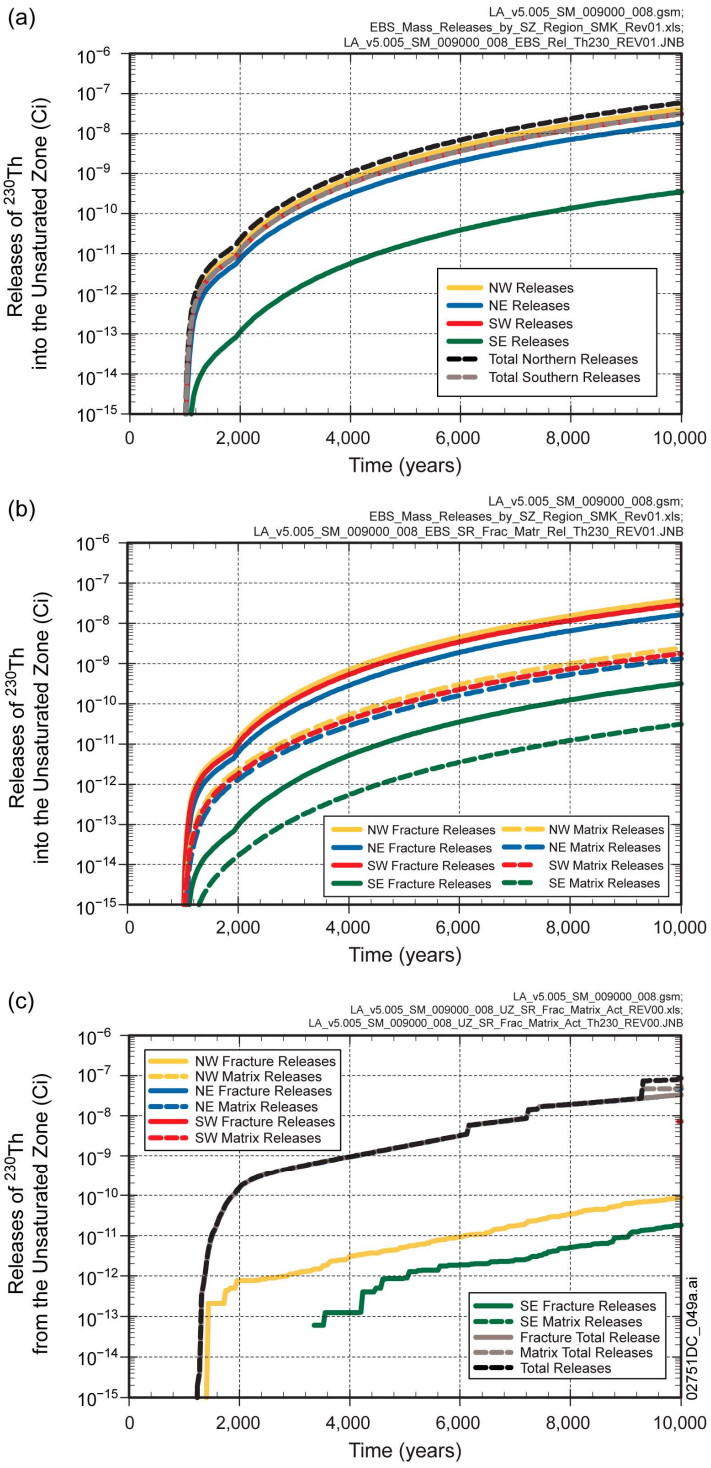

Figure 16. Total ^{230}Th Activity Released for the Seismic Ground Motion 10,000-Year Single-Realization Case from the (a) NW, NE, SW, SE, Combined Northern, and Combined Southern Regions of the Repository, (b) NW, NE, SW, and SE Regions of the Repository Divided into Unsaturated Zone Fracture and Matrix Continuums, and (c) NW, NE, SW, and SE Saturated Zone Source Regions Divided into Unsaturated Zone Fracture and Matrix Continua

2. COMMITMENTS TO NRC

None.

3. DESCRIPTION OF PROPOSED LA CHANGE

None.

4. REFERENCES

BSC (Bechtel SAIC Company) 2004. *Development of Numerical Grids for UZ Flow and Transport Modeling.* ANL-NBS-HS-000015 REV 02. Las Vegas, Nevada: Bechtel SAIC Company. ACC: DOC.20040901.0001; LLR.20080522.0082.

SNL (Sandia National Laboratories) 2007. *UZ Flow Models and Submodels.* MDL-NBS-HS-000006 REV 03 AD 01. Las Vegas, Nevada: Sandia National Laboratories. ACC: DOC.20080108.0003; DOC.20080114.0001; LLR.20080414.0007; LLR.20080414.0033; LLR.20080522.0086.

SNL 2008a. *Total System Performance Assessment Model /Analysis for the License Application.* MDL-WIS-PA-000005 REV 00 AD 01. Las Vegas, Nevada: Sandia National Laboratories. ACC: DOC.20080312.0001; LLR.20080414.0037; LLR.20080507.0002; LLR.20080522.0113.

SNL 2008c. *Particle Tracking Model and Abstraction of Transport Processes.* MDL-NBS-HS-000020 REV 02 AD 02. Las Vegas, Nevada: Sandia National Laboratories. ACC: DOC.20080129.0008; DOC.20070920.0003; LLR.20080325.0287; LLR.20080522.0170.

APPENDIX A
DETAILED ANALYSIS FOR EACH REPRESENTATIVE RADIONUCLIDE

Three of the single-realization simulations presented in the TSPA-LA (SNL 2008a) single-realization analyses were chosen for this RAI response: (1) the Igneous Intrusion 1,000,000-Year modeling case (GoldSim realization 2855 of 3000; epistemic realization 286), (2) the Seismic Ground Motion 1,000,000-Year modeling case (GoldSim realization 4641 of 9000; epistemic realization 155), and (3) the Seismic Ground Motion 10,000-Year modeling case (GoldSim realization 4641 of 9000; epistemic realization 155). The specified uncertain transport parameters sampled for these three single-realization cases are presented in Tables 5 and 6. These parameters can be compared to the parameter uncertainty distributions presented in Section 6.5 of *Particle Tracking Model and Abstraction of Transport Processes* (SNL 2008c). This appendix contains a detailed discussion of the transport of each of the representative radionuclides discussed in Section 1, for each of the three single-realization cases.

A.1 IGNEOUS INTRUSION 1,000,000-YEAR MODELING CASE

A.1.1 ^{99}Tc RELEASES

EBS releases of the nonsorbing ^{99}Tc for the Igneous Intrusion 1,000,000-Year modeling case, broken down by saturated zone source region, are presented in Figure 1a. As can be seen in the figure, the EBS release above the northwest saturated zone source region is the highest release for the Igneous Intrusion 1,000,000-Year modeling case. This is followed by the northeast and southwest regions with similar releases and the southeast region where only a small release occurs. This is consistent with the distribution of repository release nodes presented in Section 1.

The releases of ^{99}Tc at the water table for the Igneous Intrusion 1,000,000-Year modeling case are presented in Figure 1b. As can be seen by comparing the EBS and unsaturated zone releases of ^{99}Tc from the northwest and northeast regions, most of the activity released to the unsaturated zone in the northwest region ultimately leaves the unsaturated zone from the northeast saturated zone source region. This pattern of EBS release and unsaturated zone release is consistent with the conceptual model of fracture transport through the TSw, lateral transport to faults (which mainly traverse the northeast region) and vertical transport through the faults to the water table (SAR Section 2.3.8.4.5.1 and associated Figure 2.3.8-37). As can be seen in Tables 2a and 2b, virtually all of the activity entering the unsaturated zone from the EBS in the northern regions, reaches the water table within the 1,000,000-year simulation length. In addition, the magnitudes of matrix releases from the unsaturated zone in the northwest and northeast regions indicate that little ^{99}Tc activity released from the northwest and northeast regions is transported through the unsaturated zone matrix in the northern regions. In the northern region, the lack of delay time seen when comparing the EBS activity release curves to the unsaturated zone activity release curves, indicates that advection is dominating the transport of ^{99}Tc through the unsaturated zone and matrix diffusion is not playing a large role.

As can be seen by comparing the EBS and unsaturated zone releases of ^{99}Tc from the southwest and southeast regions, most of the activity released to the unsaturated zone in the southwest

region ultimately leaves the unsaturated zone from the southwest saturated zone source region. There is enough migration of ^{99}Tc from the southwest to the southeast region during transport through the unsaturated zone that the activity leaving the unsaturated zone from the southeast Region is markedly increased. This pattern of EBS release and unsaturated zone release is consistent with the conceptual model of structurally controlled matrix transport through the dipping vitric CHn facies discussed in Section 1.1. The large difference in magnitude of unsaturated zone releases from the fracture continuum relative to releases from the matrix continuum in the southwest region is caused by a change from a matrix-controlled transport regime to fracture-controlled transport before the water table is reached (BSC 2004, Figures 6-7, 6-8, and C3-2). There is also a small area of fault zone in the southern part of the Ghost Dance (west) fault that also has some control (SAR Figure 2.3.9-8). As can be seen in Tables 2a and 2b virtually all of the activity entering the unsaturated zone from the EBS in the southern regions, reaches the water table within the 1,000,000-year simulation length. The approximately 28% of the ^{99}Tc release from the matrix at the water table in the combined southwest and southeast regions is reflecting the contact of the CHn vitric facies with the water table (BSC 2004, Figure C3-2). The other 72% of the ^{99}Tc release reaches the water table via downdip transport in the fractured rock underlying the CHn vitric facies (i.e., in the Prow Pass and Bullfrog units). In the southern region, because most flow goes through the CHn vitric matrix units, retardation due to matrix diffusion from fractures to matrix does not play a large role on the transport of ^{99}Tc in the south (SNL 2008c, Addendum 1, Section 6.8.2.2).

A.1.2 ^{237}Np RELEASES

EBS releases of weakly sorbing ^{237}Np for the Igneous Intrusion 1,000,000-Year modeling case, broken down by saturated zone source region, are presented in Figure 2a. As can be seen in the figure, the EBS release above the northwest saturated zone source region is the highest release for the Igneous Intrusion 1,000,000-Year modeling case. This is followed by the northeast and southwest regions with similar releases and the southeast region where only a small release is depicted.

The releases of ^{237}Np at the water table for the Igneous Intrusion 1,000,000-Year modeling case are presented in Figure 2b. As can be seen by comparing the EBS and unsaturated zone releases of ^{237}Np from the northwest and northeast regions, most of the ^{237}Np released to the unsaturated zone in the northwest region ultimately leaves the unsaturated zone from the northeast saturated zone source region. This pattern of EBS release and unsaturated zone release in the north again reflects the conceptual model of fracture transport through the TSw, lateral transport to faults and vertical transport through the faults to the water table. The magnitudes of matrix releases from the unsaturated zone in the northwest and northeast regions indicate that little ^{237}Np activity released from the northwest and northeast regions is transported through the unsaturated zone matrix in the northern regions. In the northern region, the lack of delay time seen when comparing the EBS activity release curves to the unsaturated zone activity release curves indicates that advection is dominating the transport of ^{237}Np through the unsaturated zone and coupled matrix diffusion/matrix sorption does not have a large influence on the transport. The 1,000,000-year release results for the combined northern regions (Tables 2a and 2b) does show a small decrease in total activity leaving the unsaturated zone which reflects a small effect of matrix diffusion/matrix sorption.

As can be seen by comparing the EBS and unsaturated zone releases of ^{237}Np from the southwest and southeast regions, much of the ^{237}Np released to the unsaturated zone in the southwest region ultimately leaves the unsaturated zone from the southwest saturated zone source region (Figures 2a and 2b and Tables 2a and 2b). There is enough migration of ^{237}Np from the southwest to the southeast region during transport through the unsaturated zone that the activity leaving the unsaturated zone from the southeast Region is much greater than the magnitude the activity released to the southeast region. This pattern of EBS release and unsaturated zone release is consistent with the conceptual model of structurally controlled matrix transport through the dipping vitric CHn facies discussed in Section 1.1. About 28% of the ^{237}Np release in the southwest and southeast regions combined (Table 2b) is from the matrix reflecting the influence of the CHn vitric facies (BSC 2004, Figure C3-2). In the southern regions, virtually all of the activity released from the EBS is released from the unsaturated zone over the course of 1,000,000 years. Note also that the southwest fracture releases from the unsaturated zone show a slight delay relative to the southeast fracture releases.

A.1.3 RELEASES OF ^{242}Pu TRANSPORTED AS A DISSOLVED SPECIES SUBJECT TO COLLOID TRANSPORT

EBS releases of moderately-to-strongly sorbing ^{242}Pu transported as a dissolved species subject to reversible colloid transport for the Igneous Intrusion 1,000,000-Year modeling case are presented in Figure 3a. As can be seen in the figure, the EBS release above the northwest region is the highest release for the Igneous Intrusion 1,000,000-Year modeling case. This is followed by the northeast and southwest regions with similar releases and the southeast region with a relatively small release.

The releases of ^{242}Pu at the water table for the Igneous Intrusion 1,000,000-Year modeling case are presented in Figure 3b. As can be seen by comparing the EBS and unsaturated zone releases of ^{242}Pu from the northwest and northeast regions (Figures 3a and 3b), most of the ^{242}Pu released to the unsaturated zone in the northwest region ultimately leaves the unsaturated zone from the northeast saturated zone source region as was the case with ^{99}Tc and ^{237}Np. The magnitudes of matrix releases from the unsaturated zone in the northwest and northeast regions indicate that little ^{242}Pu activity released from the northwest and northeast regions is transported through the unsaturated zone matrix in the northern regions. In the northern region, the lack of delay time seen when comparing the EBS activity release curves to the unsaturated zone activity release curves indicates that advection is dominating the transport of ^{242}Pu through the unsaturated zone. The 1,000,000-year release results for the combined northern regions (Tables 2a and 2b) does show a 8% decrease in total activity leaving the unsaturated zone which reflects a small to moderate influence of matrix diffusion/matrix sorption.

As can be seen by comparing the EBS and unsaturated zone releases of ^{242}Pu for the southwest and southeast regions, 71% of the ^{242}Pu released to the unsaturated zone above the southern regions does not make it out of the unsaturated zone (Table 2 and Figure 3). There is enough migration of ^{242}Pu from the southwest to the southeast region during transport through the unsaturated zone that the activity leaving the unsaturated zone from the southeast region is much greater than the magnitude the activity released to the southeast region. In the southern regions, over 60% of the activity released from the EBS is not released from the unsaturated zone

indicating that matrix sorption has a moderately high effect on transport of the ^{242}Pu in the southern regions. In addition, comparing the EBS and the unsaturated zone releases of ^{242}Pu in the southwest and southeast regions shows that ^{242}Pu released from the southwest fractures was retarded more than ^{242}Pu released from the southeast fractures. This reflects a longer travel pathway to the water table in the southwest or a faster track to the water table in the southeast region associated with the Ghost Dance Fault (SAR Figure 2.3.9-8) or. Either way, the higher sorption coefficient for plutonium accentuates the delay relative to transport of nonsorbing ^{99}Tc and weakly sorbing ^{237}Np. The delay in the southern regions is also long enough that despite the moderately long half-life of ^{242}Pu (3.75×10^5 yrs), decay becomes a factor in reducing the overall activity released.

A.1.4 RELEASES OF ^{230}Th TRANSPORTED AS A DISSOLVED SPECIES SUBJECT TO COLLOID TRANSPORT

EBS releases of very strongly sorbing ^{230}Th transported as a dissolved species subject to reversible colloid transport for the Igneous Intrusion 1,000,000-Year modeling case are presented in Figure 4a. As can be seen in the figure, the EBS release above the northwest saturated zone source region is the highest release for the Igneous Intrusion 1,000,000-Year modeling case. This is followed by the southwest and northeast regions with similar releases and the southeast region with a relatively small release.

The releases of ^{230}Th at the water table for the Igneous Intrusion 1,000,000-Year modeling case are presented in Figure 4b. As can be seen by comparing the EBS and unsaturated zone releases of ^{230}Th from the northwest and northeast regions (Figures 4a and 4b), most of the ^{230}Th released to the unsaturated zone in the northwest region ultimately leaves the unsaturated zone from the northeast saturated zone source region. The magnitudes of matrix releases from the unsaturated zone in the northwest and northeast regions indicate that little ^{230}Th activity released from the northwest and northeast regions is transported through the unsaturated zone matrix in the northern regions. In the combined northern regions, there is an almost 23% reduction in activity between the EBS and unsaturated zone releases over 1,000,000 years (Tables 2a and 2b) reflecting a moderate influence of coupled matrix diffusion/matrix sorption.

As can be seen by comparing the EBS and unsaturated zone releases of ^{230}Th from the southwest and southeast regions (Figures 4a and 4b), most of the ^{230}Th released from the unsaturated zone is from the southeast region. This reversal from releases of ^{99}Tc, ^{237}Np, and ^{242}Pu reflects the highly sorptive nature of ^{230}Th and the strong influence of sorption in much of the southwest region. In the southern regions, an almost two orders of magnitude difference between the EBS and unsaturated zone activity releases indicates that matrix sorption in the CHn vitric facies strongly controls the amount of mass of low solubility, very strongly sorbing radionuclides that can leave the system. The delay in the southern regions is also long enough that despite the moderately long half-life of ^{230}Th (7.54×10^4 yrs), decay becomes a factor in reducing the overall activity released.

A.1.5 RELEASES OF ^{242}Pu IRREVERSIBLY ATTACHED TO COLLOIDS

EBS releases of ^{242}Pu irreversibly attached to colloids for the Igneous Intrusion 1,000,000-Year modeling case, broken down by saturated zone source region, are presented in Figures 5a and 6a for the slow (subject to filtration as simulated using a retardation coefficient) and fast colloids (not subject to filtration), respectively. As can be seen in the figures, the EBS release above the northwest saturated zone source region is the highest release for the Igneous Intrusion 1,000,000-Year modeling case. This is followed by the northeast and southwest regions with similar releases and the southeast region where only a small release is depicted. In addition the releases for the slow and fast colloids differ only in magnitude, where the slow colloids represent 99.8% of the release and the fast colloids represent 0.168% of the release. The releases at the water table of ^{242}Pu irreversibly attached to colloids for the Igneous Intrusion 1,000,000-Year modeling case are presented in Figures 5b and 6b. As can be seen by comparing the EBS and unsaturated zone releases of ^{242}Pu irreversibly attached to colloids for either case, from the northwest and northeast regions, most of the activity released to the unsaturated zone in the northwest region ultimately leaves the unsaturated zone from the northeast saturated zone source region reflecting the conceptual model of fracture transport through the TSw, lateral transport to faults (which mainly traverse the northeast region as shown in SAR Figure 2.3.9-8) and vertical transport through the faults to the water table (SAR Section 2.3.8.4.5.1 and associated Figure 2.3.8-37). As can be seen in Tables 2a and 2b, virtually all of the activity from ^{242}Pu irreversibly attached to colloids entering the unsaturated zone from the EBS in the northern regions, reaches the water table within the 1,000,000-year simulation length. In addition, the magnitudes of matrix releases from the unsaturated zone in the northwest and northeast regions indicate that little of the ^{242}Pu irreversibly attached to colloids released from the northwest and northeast regions is transported through the unsaturated zone matrix in the northern regions.

As can be seen by comparing the EBS and unsaturated zone releases of ^{242}Pu irreversibly attached to slow and fast colloids from the southwest and southeast regions (Figures 5a, 5b, 6a, and 6b), 98% to 99% of the activity released to the unsaturated zone in the southwest region ultimately leaves the unsaturated zone from the southwest saturated zone source region (Table 2b). But again, there is enough migration of ^{242}Pu irreversibly attached to colloids from the southwest to the southeast region during transport through the unsaturated zone that the activity leaving the unsaturated zone from the southeast region is much greater than the activity released to the southeast region. As can be seen in Tables 2a and 2b, virtually all of the ^{242}Pu activity entering the unsaturated zone from the EBS in the southern regions, reaches the water table within the 1,000,000-year simulation length.

In the northern regions, the lack of differences between delay time seen when comparing the slow and fast colloid unsaturated zone activity release curves (Figures 5a, 5b, 6a, and 6b), indicates that advection is dominating the transport of ^{242}Pu irreversibly attached to colloids through the unsaturated zone and the rapid transport rate in the north offsets the influence of reversible colloid filtration of the slow fraction of irreversible colloids. Little difference is also seen in the south, but this lack of influence of reversible colloid filtration in the south is a reflection of the dominance of matrix flow and transport in the CHn vitric facies where reversible filtration is not modeled (reversible filtration is confined to the fractures).

A.2 SEISMIC 1,000,000-YEAR GROUND MOTION MODELING CASE

A.2.1 ^{99}Tc RELEASES

EBS releases of the nonsorbing ^{99}Tc for the Seismic Ground Motion 1,000,000-Year modeling case, broken down by saturated zone source region, are presented in Figure 7a. As can be seen in the figure, the EBS release above the northwest saturated zone source region is the highest release for the Seismic Ground Motion 1,000,000-Year modeling case. This is followed by the northeast and southwest regions with similar releases and the southeast region where only a small release is depicted. This is consistent with the distribution of repository release nodes presented in Section 1. The EBS releases of ^{99}Tc separated with respect to unsaturated zone continuum and saturated zone source region are presented in Figure 7b. As can be seen in Figure 7b, the majority of the ^{99}Tc release to the unsaturated zone enters the fractures for each of the four regions (northwest, northeast, southwest, and southeast). It can also be seen in Figure 7b, the ratio of fracture release to matrix release in the northwest and southwest regions is greater than in the northeast and southeast regions reflecting that a higher percentage of nodes from the higher percolation rate bins is found in the northwest and southwest regions, as depicted in SAR Figure 2.3.8-25.

The releases of ^{99}Tc at the water table for the Seismic Ground Motion 1,000,000-Year modeling case are presented in Figure 7c. As can be seen by comparing the EBS and unsaturated zone releases of ^{99}Tc from the northwest and northeast regions, most of the activity released to the unsaturated zone in the northwest region ultimately leaves the unsaturated zone from the northeast saturated zone source region reflecting the fault controlled conceptual model. As can be seen in Tables 3a and 3b, most of the activity entering the unsaturated zone from the EBS in the northern regions reaches the water table within the 1,000,000-year simulation length. In addition, the magnitudes of matrix releases from the unsaturated zone in the northwest and northeast regions indicate that little ^{99}Tc activity released from the northwest and northeast regions is transported through the unsaturated zone matrix in the northern regions.

As can be seen by comparing the EBS and unsaturated zone releases of ^{99}Tc from the southwest and southeast regions (Figures 7a and 7b), most of the activity released to the unsaturated zone in the southwest region leaves the unsaturated zone from the southwest saturated zone source region. There is enough migration of ^{99}Tc from the southwest to the southeast region during transport through the unsaturated zone that the activity leaving the unsaturated zone from the southeast region is more than a factor of six times the activity released to the southeast region. This pattern of EBS release and unsaturated zone release is consistent with the conceptual model of structurally controlled matrix transport through the dipping vitric CHn facies discussed in Section 1.1. As can be seen in Tables 3a and 3b, most of the activity entering the unsaturated zone from the EBS in the southern regions reaches the water table within the 1,000,000-year simulation length. The large difference in magnitude of unsaturated zone releases from the fracture continuum relative to releases from the matrix continuum in the southwest region is consistent with a change from a matrix controlled transport regime to a fractured media controlled transport before the water table is reached (BSC 2004, Figures 6-7, 6-8, and C3-2). The more balanced ratio of unsaturated zone releases from the fracture continuum relative to

releases from the matrix continuum in the southeast is indicative of contact between the CHn vitric facies and the water table (BSC 2004, Figure C3-2).

In the northern and southern regions, the lack of delay time seen when comparing the EBS activity release curves to the unsaturated zone activity release curves (Figures 7a and 7b), indicates that advection is dominating the transport of ^{99}Tc through the unsaturated zone and matrix diffusion does not play a large role on the transport highly soluble, nonsorbing radionuclides within the unsaturated zone.

A.2.2 ^{237}Np RELEASES

EBS releases of weakly sorbing ^{237}Np for the Seismic Ground Motion 1,000,000-Year modeling case, broken down by saturated zone source region, are presented in Figure 8a. As can be seen in the figure, the EBS release above the northwest saturated zone source region is the highest release for the Seismic Ground Motion 1,000,000-Year modeling case. This is followed by the northeast and southwest regions with similar releases and the southeast region where only a small release is depicted. This is again consistent with the distribution of repository release nodes presented in Section 1. The EBS releases of ^{237}Np broken down with respect to unsaturated zone continuum and saturated zone source region are presented in Figure 8b. As can be seen in Figure 8b, the majority of the ^{237}Np release to the unsaturated zone enters the fractures for each of the four regions (northwest, northeast, southwest, and southeast).

The releases of ^{237}Np at the water table for the Seismic Ground Motion 1,000,000-Year modeling case are presented in Figure 8c. Figures 8b and 8c of the EBS and unsaturated zone releases of ^{237}Np from the northwest and northeast regions show that most of the ^{237}Np released to the unsaturated zone in the northwest region ultimately leaves the unsaturated zone from the northeast saturated zone source region. This pattern of EBS release and unsaturated zone release in the north again reflects the conceptual model of fracture transport through the TSw, lateral transport to faults and vertical transport through the faults to the water table. The magnitudes of matrix releases from the unsaturated zone in the northwest and northeast regions indicate that little ^{237}Np activity released from the northwest and northeast regions is transported through the unsaturated zone matrix in the northern regions. In the northern region, the lack of delay time seen when comparing the EBS activity release curves to the unsaturated zone activity release curves indicates that advection is dominating the transport of ^{237}Np through the unsaturated zone and coupled matrix diffusion/matrix sorption does not have a large influence on the transport. The 1,000,000-year release results for the combined northern regions (Tables 3a and 3b) does show a small decrease in total activity leaving the unsaturated zone which reflects a small effect of matrix diffusion/matrix sorption.

As can be seen by comparing the EBS and unsaturated zone releases of ^{237}Np from the southwest and southeast regions (Figures 8a and 8b), much of the ^{237}Np released to the unsaturated zone in the southwest region ultimately leaves the unsaturated zone from the southwest saturated zone source region. There is enough migration of ^{237}Np from the southwest to the southeast region during transport through the unsaturated zone that the activity leaving the unsaturated zone from the southeast region is much greater than the magnitude of the activity released to the southeast region. This pattern of EBS release and unsaturated zone release is consistent with the

conceptual model of structurally controlled matrix transport through the dipping vitric CHn facies discussed in Section 1.1. The large difference in magnitude of unsaturated zone releases from the fracture continuum relative to releases from the matrix continuum in the southwest region is consistent with a change from a matrix controlled transport regime to a fractured media controlled transport before the water table is reached (BSC 2004, Figures 6-7, 6-8, and C3-2) or the influence of Ghost Dance (west) fault. The more balanced ratio of unsaturated zone releases from the fracture continuum relative to releases from the matrix continuum in the southeast is indicative of the importance of the area of contact between the CHn vitric facies and the water table (BSC 2004, Figure C3-2). In the southern regions, over 12% of the activity released from the EBS is not released from the unsaturated zone indicating that matrix sorption has a low to moderate effect on transport of low to moderately soluble, weakly sorbing radionuclides in the southern regions which are dominated by the matrix transport in the CHn vitric units. Note that this decrease in the activity release is greater than for the igneous simulation because this simulation has a higher sampled K_d for ^{237}Np, showing the influence of matrix sorption in the resutls. Also note that the southwest fracture releases from the unsaturated zone show a slight delay relative to the southeast fracture releases, reflecting a longer travel distance to the water table.

A.2.3 RELEASES OF ^{242}Pu TRANSPORTED AS A DISSOLVED SPECIES SUBJECT TO COLLOID TRANSPORT

EBS releases of moderately-to-strongly sorbing ^{242}Pu transported as a dissolved species subject to reversible colloid transport for the Seismic Ground Motion 1,000,000-Year modeling case, broken down by saturated zone source region, are presented in Figure 9a. As can be seen in the figure, the EBS release above the northwest saturated zone source region is the highest release for the Seismic Ground Motion 1,000,000-Year modeling case. This is followed by the northeast and southwest regions with similar releases and the southeast region with a relatively small release. The EBS releases of ^{242}Pu broken down with respect to unsaturated zone continuum and saturated zone source region are presented in Figure 9b. As can be seen in Figure 9b, the majority of the ^{242}Pu is released to the unsaturated zone fractures for each of the four regions (northwest, northeast, southwest, and southeast).

The releases of ^{242}Pu at the water table for the Seismic Ground Motion 1,000,000-Year modeling case are presented in Figure 9c. As can be seen by comparing the EBS and unsaturated zone releases of ^{242}Pu from the northwest and northeast regions, most of the ^{242}Pu released to the unsaturated zone in the northwest region ultimately leaves the unsaturated zone from the northeast saturated zone source region. This pattern of EBS release and unsaturated zone release reflects the fault controlled transport in the north. The magnitudes of matrix releases from the unsaturated zone in the northwest and northeast regions indicate that little ^{242}Pu activity released from the northwest and northeast regions is transported through the unsaturated zone matrix in the northern regions. In the northern region, the lack of delay time seen when comparing the EBS activity release curves to the unsaturated zone activity release curves indicates that advection is dominating the transport of ^{242}Pu through the unsaturated zone. The 1,000,000-year release results for the combined northern regions (Tables 3a and 3b) does show a 16% decrease in total activity leaving the unsaturated zone which reflects a small to moderate influence of matrix diffusion/matrix sorption for moderately-to-strongly sorbing radionuclides.

As can be seen by comparing the EBS and unsaturated zone releases of ^{242}Pu from the southwest and southeast regions, most of the ^{242}Pu released to the unsaturated zone in the southwest region does not make it out of the unsaturated zone (Figure 9). There is still enough migration of ^{242}Pu from the southwest to the southeast region during transport through the unsaturated zone (Figures 9a and 9b) that the activity leaving the unsaturated zone from the southeast region is much greater than the magnitude the activity released to the southeast region. In the southern regions, over 80% of the activity released from the EBS is not released from the unsaturated zone indicating that matrix sorption has a large effect on transport of the ^{242}Pu in the southern regions which are dominated by the matrix transport in the CHn vitric units. In addition comparing the EBS and the unsaturated zone releases of ^{242}Pu in the southwest and southeast regions shows that ^{242}Pu released from the southwest fractures was retarded more than ^{242}Pu released from the southeast fractures. This reflects a longer travel pathway to the water table in the southwest or a faster track to the water table in the southeast region associated with the Ghost Dance Fault (SAR Figure 2.3.9-8) or both. Either way, the higher sorption coefficient for plutonium accentuates the delay relative to transport of nonsorbing ^{99}Tc and weakly sorbing ^{237}Np. The delay in the southern regions is also long enough that despite the moderately long half-life of ^{242}Pu (3.75×10^5 yrs), decay becomes a factor in reducing the overall activity released.

A.2.4 RELEASES OF ^{230}Th TRANSPORTED AS A DISSOLVED SPECIES SUBJECT TO COLLOID TRANSPORT

EBS releases of very strongly sorbing ^{230}Th transported as a dissolved species subject to reversible colloid transport for the Seismic Ground Motion 1,000,000-Year modeling case, broken down by saturated zone source region, are presented in Figure 10a. As can be seen in Figure 10a, the EBS release above the northwest saturated zone source region is the highest release for the Seismic Ground Motion 1,000,000-Year modeling case. This is followed by the southwest and northeast regions with similar releases and the southeast region with a relatively small release. The EBS releases of ^{230}Th broken down with respect to unsaturated zone continuum and saturated zone source region are presented in Figure 10b. As can be seen in Figure 10b, the majority of the ^{230}Th is released to the unsaturated zone fractures for each of the four regions (northwest, northeast, southwest, and southeast).

The releases of ^{230}Th at the water table for the Seismic Ground Motion 1,000,000-Year modeling case are presented in Figure 10c. As can be seen by comparing the EBS and unsaturated zone releases of ^{230}Th from the northwest and northeast regions (Figures 10b and 10c), most of the ^{230}Th released to the unsaturated zone in the northwest region ultimately leaves the unsaturated zone from the northeast saturated zone source region. This pattern of EBS release and unsaturated zone release again reflects the fault controlled transport beneath the northern part of the repository. The magnitudes of matrix releases from the unsaturated zone in the northwest and northeast regions indicate that little ^{230}Th activity released from the northwest and northeast regions is transported through the unsaturated zone matrix in the northern regions. In the northern region, the almost 30% reduction in activity between the EBS and unsaturated zone releases over 1,000,000 years in the combined northern regions (Tables 3a and 3b) reflects a moderate influence of coupled matrix diffusion/matrix sorption on low solubility, very strongly sorbing radionuclides. (At 47,500 years, a step release of ^{230}Th from the unsaturated zone

occurs, which goes higher than the cumulative release from the EBS at that same time. This sudden release is associated with ingrowth (i.e., decay of ^{230}Th's parent ^{234}U). The step nature of the unsaturated zone cumulative release curve at 47,500 years is because unsaturated zone mass transport is represented by finite particles, each representing a specified amount of ^{230}Th. Because of the large ^{234}U initial inventory relative to ^{230}Th, it would only take the release of one decayed ^{234}U particle to cause the step change seen in Figure 10c.)

As can be seen by comparing the EBS and unsaturated zone releases of ^{230}Th from the southwest and southeast regions, most of the ^{230}Th released from the unsaturated zone is from the southeast region (Figure 10). This reversal from releases of ^{99}Tc, ^{237}Np, and ^{242}Pu (in later times) reflects the highly sorptive nature of ^{230}Th and the added effectiveness of the sorption in much of the southwest region. In the southern regions, a two orders of magnitude differences in the EBS and unsaturated zone activity releases indicates that matrix sorption in conjunction with dominantly matrix flow through the CHn vitric facies strongly controls the amount of mass from low solubility, very strongly sorbing radionuclides that can leave the unsaturated zone. The delay in the southern regions is also long enough that despite the moderately long half-life of ^{230}Th (7.54×10^4 yrs), decay becomes a factor in reducing the overall activity released.

A.2.5 RELEASES OF ^{242}Pu IRREVERSIBLY ATTACHED TO COLLOIDS

EBS releases of ^{242}Pu irreversibly attached to colloids for the Seismic Ground Motion 1,000,000-Year modeling case, broken down by saturated zone source region, are presented in Figures 11a and 12a for the slow (subject to filtration as simulated using a retardation coefficient) and fast colloids (not subject to filtration), respectively. As can be seen in the figures, the EBS release above the northwest saturated zone source region is the highest release for the Seismic Ground Motion 1,000,000-Year modeling case. This is followed by the northeast and southwest regions with similar releases and the southeast region where only a small release is depicted. In addition the releases for the slow and fast colloids differ only in magnitude, where the slow colloids represent 99.8% of the release and the fast colloids represent 0.168% of the release. The EBS releases of ^{242}Pu irreversibly attached to colloids broken down with respect to unsaturated zone continuum and saturated zone source region are presented in Figures 11b and 12b, for slow and fast colloids, respectively. As can be seen in Figures 11b and 12b, the majority of the ^{242}Pu irreversibly attached to colloids release to the unsaturated zone enters the fractures for each of the four regions (northwest, northeast, southwest, and southeast). Prior to 500,000 years the EBS releases to the matrix are small compared to the releases to the fractures, but not as small proportionately as after 500,000 years.

The releases at the water table of ^{242}Pu irreversibly attached to colloids for the Seismic Ground Motion 1,000,000-Year modeling case are presented in Figures 11c and 12c. As can be seen by comparing the EBS and unsaturated zone releases of ^{242}Pu irreversibly attached to colloids, from the northwest and northeast regions for either case, most of the activity released to the unsaturated zone in the northwest region ultimately leaves the unsaturated zone from the northeast saturated zone source region. This pattern of EBS release and unsaturated zone release is consistent with the conceptual model of fault controlled transport in the north. As can be seen in Tables 3a and 3b, virtually all of the activity entering the unsaturated zone from the EBS in the northern regions, reaches the water table within the 1,000,000-year simulation length.

In addition, the magnitudes of matrix releases from the unsaturated zone in the northwest and northeast regions indicate that little of the ^{242}Pu irreversibly attached to colloids released from the northwest and northeast regions is transported through the unsaturated zone matrix in the northern regions. In the northern regions, the lack of differences between delay time seen when comparing the slow and fast colloid unsaturated zone activity release curves, indicates that advection is dominating the transport of ^{242}Pu irreversibly attached to colloids through the unsaturated zone and the rapid transport rate in the north offsets the influence of reversible colloid filtration of the slow fraction of irreversible colloids.

As can be seen by comparing the EBS and unsaturated zone releases ^{242}Pu irreversibly attached to slow and fast colloids from the southwest and southeast regions, most of the activity released to the unsaturated zone in the southwest region ultimately leaves the unsaturated zone from the southwest saturated zone source region (Figures 11 and 12). There is enough migration of ^{242}Pu irreversibly attached to colloids from the southwest to the southeast region during transport through the unsaturated zone that the activity leaving the unsaturated zone from the southeast region is greater than the activity released to the southeast region. It can also be seen that the increase is relatively larger for the ^{242}Pu irreversibly attached to colloids released from the matrix in the southeast as opposed to ^{242}Pu released from fractures. As can be seen in Tables 3a and 3b, virtually all of the ^{242}Pu activity entering the unsaturated zone from the EBS in the southern regions, reaches the water table within the 1,000,000-year simulation length. The larger difference in magnitude of unsaturated zone releases from the fracture continuum relative to releases from the matrix continuum in the southwest region is consistent with a change from a matrix controlled transport regime to a fractured media controlled transport before the water table is reached (BSC 2004, Figures 6-7, 6-8, and C3-2). The more balanced ratio of unsaturated zone releases from the fracture continuum relative to releases from the matrix continuum in the southeast reflects the contact between the CHn vitric facies and the water table (BSC 2004, Figure C3-2). Little difference in delay time when comparing the slow and fast colloid unsaturated zone activity release curves is seen in the south, but this lack of influence of reversible colloid filtration is a reflection of the dominance of matrix flow and transport in the CHn vitric facies where reversible filtration is not modeled (reversible filtration is confined to the fractures).

A.3 SEISMIC 10,000-YEAR GROUND MOTION MODELING CASE

A.3.1 ^{99}Tc RELEASES

EBS releases of the nonsorbing ^{99}Tc for the Seismic Ground Motion 10,000-Year modeling case, broken down by saturated zone source region, are presented in Figure 13a. As can be seen in the figure, the EBS release above the northwest region is the highest release for the Seismic Ground Motion 10,000-Year modeling case. This is followed by the southwest and northeast regions with similar releases and the southeast region where only a small release is depicted. This is consistent with the distribution of repository release nodes presented in Section 1. The EBS releases of ^{99}Tc broken down with respect to unsaturated zone continuum and saturated zone source region are presented in Figure 13b. As can be seen in Figure 13b, the majority of the ^{99}Tc release to the unsaturated zone enters the matrix for each of the four regions (northwest, northeast, southwest, and southeast).

The releases of ^{99}Tc at the water table for the Seismic Ground Motion 10,000-Year modeling case are presented in Figure 13c. As can be seen by comparing the EBS and unsaturated zone releases of ^{99}Tc from the northwest and northeast regions, most of the activity released to the unsaturated zone in the northwest region ultimately leaves the unsaturated zone from the northeast region. This pattern of EBS release and unsaturated zone release is consistent with the conceptual model of fracture transport through the TSw, lateral transport to faults (which mainly traverse the northeast region) and vertical transport through the faults to the water table (SAR Section 2.3.8.4.5.1 and associated Figure 2.3.8-37). As can be seen in Tables 4a and 4b, 73% of the activity entering the unsaturated zone from the EBS in the northern regions, reaches the water table within the 10,000-year simulation length. The release of most of the ^{99}Tc to the rock matrix decreases the amount of mass that can reach the water table over a 10,000-year period. The increased EBS release to the matrix strongly influences the amount of release from the unsaturated zone that takes place in the north.

As can be seen by comparing the EBS and unsaturated zone releases of ^{99}Tc from the southwest and southeast regions, much of the activity released to the unsaturated zone in the southwest region ultimately leaves the unsaturated zone from the southwest region through the fractures (Figure 13). There is enough migration of ^{99}Tc from the southwest to the southeast region during transport through the unsaturated zone that the activity leaving the unsaturated zone from the southeast region is more than the activity released from the EBS to the southeast region. In addition, the mass leaving the unsaturated zone by matrix in the southeast is almost as large as by fractures in the southeast. As can be seen in Tables 4a and 4b, 78% of the activity entering the unsaturated zone from the EBS in the southern regions, reaches the water table within the 10,000-year simulation length. The large difference in magnitude of unsaturated zone releases from the fracture continuum relative to releases from the matrix continuum in the southwest region is consistent with a change from a matrix controlled transport regime to a fractured media controlled transport before the water table is reached (BSC 2004, Figures 6-7, 6-8, and C3-2) and/or mass release through the western branch of the Ghost Dance Fault Zone. The more balanced ratio of unsaturated zone releases from the fracture continuum relative to releases from the matrix continuum in the southeast is indicative of the importance of contact between the CHn vitric facies and the water table (BSC 2004, Figure C3-2). In the south, the mass remaining in the unsaturated zone after 10,000 years is a product of the matrix flow in the CHn vitric units that delays the release enough that 22% of the ^{99}Tc mass remains in the unsaturated zone.

A.3.2 ^{237}Np RELEASES

EBS releases of weakly sorbing ^{237}Np for the Seismic Ground Motion 10,000-Year modeling case, broken down by saturated zone source region, are presented in Figure 14a. As can be seen in the figure, the EBS release above the northwest saturated zone source region is the highest release for the Seismic Ground Motion 10,000-Year modeling case. This is followed by the southwest then the northeast regions and the southeast region where only a small release is depicted. The EBS releases of ^{237}Np broken down with respect to unsaturated zone continuum and saturated zone source region are presented in Figure 14b. As can be seen in Figure 14b, most of the ^{237}Np release to the unsaturated zone enters the fractures for each of the four regions (northwest, northeast, southwest, and southeast). But as can be seen in Tables 4a and 4b, there

is a sizable amount of ^{237}Np released to the matrix, with 21% of the EBS release enters the matrix in the northern regions and 20% enters the matrix in the southern regions.

The releases of ^{237}Np at the water table for the Seismic Ground Motion 10,000-Year modeling case are presented in Figure 14c. As can be seen by comparing the EBS and unsaturated zone releases of ^{237}Np from the northwest and northeast regions, most of the ^{237}Np released to the unsaturated zone in the northwest region ultimately leaves the unsaturated zone from the northeast saturated zone source region. This pattern of EBS release and unsaturated zone release reflects the fault controlled releases in the north. The magnitudes of matrix releases from the unsaturated zone in the northwest and northeast regions indicate that little ^{237}Np activity released from the northwest and northeast regions is transported through the unsaturated zone matrix in the northern regions. In the northern region, the lack of delay time seen when comparing the EBS activity release curves to the unsaturated zone activity release curves indicates that advection is dominating the transport of ^{237}Np through the unsaturated zone. The 10,000-year release results for the combined northern regions (Tables 4a and 4b) does show a 19% decrease in total activity leaving the unsaturated zone which reflects the influence of the EBS release to the matrix, coupled matrix diffusion/matrix sorption and the shorter time period.

As can be seen by comparing the EBS and unsaturated zone releases of ^{237}Np from the southwest and southeast regions, much of the ^{237}Np released to the unsaturated zone in the southwest region does not make it out of the unsaturated zone (Figure 14). There is enough migration of ^{237}Np from the southwest to the southeast region during transport through the unsaturated zone that the activity leaving the unsaturated zone from the southeast region is much greater than the magnitude the activity released to the southeast region. In the southern regions, only 26% of the activity released from the EBS is released from the unsaturated zone over the course of 10,000 years (Tables 4a and 4b). In addition comparing the EBS and the unsaturated zone releases of ^{237}Np in the southwest and southeast regions shows that ^{237}Np released from the southwest fractures was retarded more than ^{237}Np released from the southeast fractures. This reflects a longer travel pathway to the water table in the southwest or a faster track to the water table in the southeast region associated with the Ghost Dance Fault (SAR Figure 2.3.9-8) or both. Either way, over a 10,000-year period, even the low sorption coefficient for ^{237}Np (Table 6) accentuates the delay relative to transport of nonsorbing ^{99}Tc.

A.3.3 RELEASES OF ^{242}Pu TRANSPORTED AS A DISSOLVED SPECIES SUBJECT TO COLLOID TRANSPORT

EBS releases of moderately-to-strongly sorbing ^{242}Pu transported as a dissolved species subject to reversible colloid transport for the Seismic Ground Motion 10,000-Year modeling case, broken down by saturated zone source region, are presented in Figure 15a. As can be seen in the figure, the EBS release above the northwest saturated zone source region is the highest release for the Seismic Ground Motion 10,000-Year modeling case. This is followed by the southwest and northeast regions with the southwest being greater, and the southeast region with a relatively small release. The EBS releases of ^{242}Pu broken down with respect to unsaturated zone continuum and saturated zone source region are presented in Figure 15b. As can be seen in Figure 15b, the majority of the ^{242}Pu release to the unsaturated zone enters the fractures for each of the four regions (northwest, northeast, southwest, and southeast).

The releases of ^{242}Pu at the water table for the Seismic Ground Motion 10,000-Year modeling case are presented in Figure 15c. As can be seen by comparing the EBS and unsaturated zone releases of ^{242}Pu from the northwest and northeast regions, most of the ^{242}Pu released to the unsaturated zone in the northwest region ultimately leaves the unsaturated zone from the northeast saturated zone source region. This pattern of EBS release and unsaturated zone release again reflects the conceptual model of fault controlled transport in the north. The magnitudes of matrix releases from the unsaturated zone in the northwest and northeast regions indicate that little ^{242}Pu activity released from the northwest and northeast regions is transported through the unsaturated zone matrix in the northern regions. In the northern region, the lack of delay time seen when comparing the EBS activity release curves to the unsaturated zone activity release curves indicates that advection is dominating the transport of ^{242}Pu through the unsaturated zone. The 10,000-year release results for the combined northern regions (Tables 4a and 4b) does show a 24% decrease in total activity leaving the unsaturated zone which reflects a small to moderate influence of matrix diffusion/matrix sorption for moderately-to-strongly sorbing radionuclides.

As can be seen by comparing the EBS and unsaturated zone releases of ^{242}Pu from the southwest and southeast regions, most of the ^{242}Pu released to the unsaturated zone in the southwest region does not make it out of the unsaturated zone (Figure 15). There is enough migration of ^{242}Pu from the southwest to the southeast region during transport through the unsaturated zone that the activity leaving the unsaturated zone from the southeast region is much greater than the magnitude the activity released to the southeast region. In the southern regions, over 98% of the activity released from the EBS remains in the unsaturated zone (Table 4) indicating that matrix sorption has a high effect on transport of the ^{242}Pu in the southern regions which are dominated by the matrix transport in the CHn vitric units. In addition comparing the EBS and the unsaturated zone releases of ^{242}Pu in the southwest and southeast regions shows that ^{242}Pu released from the southwest fractures was retarded more than ^{242}Pu released from the southeast fractures. This reflects a longer travel pathway to the water table in the southwest or a faster track to the water table in the southeast region associated with the Ghost Dance Fault (SAR Figure 2.3.9-8) or both. Either way, the higher sorption coefficient for plutonium accentuates the delay relative to transport of nonsorbing ^{99}Tc and weakly sorbing ^{237}Np (Figures 13c and 14c).

A.3.4 RELEASES OF ^{230}Th TRANSPORTED AS A DISSOLVED SPECIES SUBJECT TO COLLOID TRANSPORT

EBS releases of very strongly sorbing ^{230}Th transported as a dissolved species subject to reversible colloid transport for the Seismic Ground Motion 10,000-Year modeling case are presented in Figure 16a. As can be seen in the figure, the EBS release above the northwest saturated zone source region is the highest release for the Seismic Ground Motion 10,000-Year modeling case. This is followed by the southwest and northeast regions with the southwest release being larger, and the southeast region with a relatively small release. The EBS releases of ^{230}Th broken down with respect to unsaturated zone continuum and saturated zone source region are presented in Figure 16b. As can be seen in Figure 16b, the majority of the ^{230}Th release to the unsaturated zone enters fractures for each of the four regions (northwest, northeast, southwest, and southeast).

The releases of ^{230}Th at the water table for the Seismic Ground Motion 10,000-Year modeling case are presented in Figure 16c. As can be seen by comparing the EBS and unsaturated zone releases of ^{230}Th from the northwest and northeast regions, most of the ^{230}Th released to the unsaturated zone in the northwest region ultimately leaves the unsaturated zone from the northeast saturated zone source region. This pattern of EBS release and unsaturated zone release again reflects the conceptual model of fault controlled transport in the north. At 9,320 years, a step release of ^{230}Th from the unsaturated zone occurs, which goes higher than the cumulative release from the EBS at that same time. As with the Seismic Ground Motion 1,000,000-Year modeling case, this sudden release is associated with ingrowth (i.e., decay of ^{230}Th's parent ^{234}U). The step nature of the unsaturated zone cumulative release curve at 9,320 years is because unsaturated zone mass transport is represented by finite particles, each representing a specified amount of ^{230}Th. Because of the large ^{234}U initial inventory relative to ^{230}Th, it would only take the release of one decayed ^{234}U particle to cause the step change seen in Figure 16c. The large magnitude of matrix releases in Tables 4a and 4b is not reflective of ^{230}Th releases from the EBS, but rather of matrix transport of ^{230}Th particles that are daughters of ^{234}U particles, which decayed while they were traveling through the unsaturated zone matrix. Note that Figure 16c indicates that most of the mass is released from fractures in the north, until the ^{234}U daughter product release shows up. In the northern region, the almost 43% reduction in activity between the EBS and unsaturated zone releases over 10,000 years for the combined northern regions (if the activity from the ^{234}U daughter product release of 4.6×10^{-8} Ci is disregarded) reflects a moderate to high influence of coupled matrix diffusion/matrix sorption for very strongly sorbing radionuclides.

As can be seen by comparing the EBS and unsaturated zone releases of ^{230}Th from the southwest and southeast regions, most of the ^{230}Th released from the unsaturated zone is from the southeast region through the fracture continuum (Figure 16). This is in contrast to the much greater southwest releases of ^{99}Tc early on, and ^{237}Np at later times (see Figures 13c and 14c), which reflects the highly sorptive nature of ^{230}Th and the added effectiveness of the sorption in much of the SW region. Note that ^{230}Th releases from the southwest fractures are barely visible in Figure 16c because of the delay caused by matrix sorption. They begin to appear at 9,960 years. However, they do not represent transport of ^{230}Th from the EBS to the water table but, rather, the ingrowth of a single ^{234}U parent particle that was transported through the SW matrix and decayed to ^{230}Th. This is reflected in Table 4, which shows that 23% of the ^{230}Th mass released from the EBS is released to the water table in 10,000 years. However, this number simply represents the finite amount of ingrowth activity (7.26×10^{-9} Ci) from the decay of the single ^{234}U particle. If this ingrowth mass is removed from the calculation, then the total percent of EBS release that reaches the water table would be only 0.03%.

A.3.5 RELEASES OF ^{242}Pu IRREVERSIBLY ATTACHED TO COLLOIDS

In the single realization study of the 10,000-year Seismic Ground Motion modeling case, the ionic strength inside the failed waste packages generally exceeds 1 molal, which results in unstable colloid suspensions. Colloidal transport in the waste package is limited. As a result, colloid releases from the EBS are not significant from this modeling case. Therefore, colloid releases from the EBS were not partitioned by saturated zone region.

RAI Volume 3, Chapter 2.2.1.3.7, First Set, Number 2:

Describe how sorption is simulated in fault zones in the UZ transport model.

Basis: Aqueous radionuclides that travel through fractures in the unsaturated zone are assumed not to sorb to fracture surfaces except in fault zones (e.g., Drill Hole Wash Fault, Pagany Wash Fault) (SAR, Section 2.3.8.5.2.3). The fault zone is treated as a fracture continuum with low porosity where sorption on fracture surfaces can occur (SAR, Section 2.4.2.3.2.1.9 Unsaturated Zone Transport). DOE provides radioelement-specific sorption parameter distributions based on rock type, but the referenced supporting information (SNL, 2007, Appendix A, Section A6) does not provide sufficient information on how these, or other parameters, are used to simulate transport in the fault zones. This information is needed to verify compliance with 10 CFR 63.114(a) and 63.114(b).

1. RESPONSE

Faults in the unsaturated zone transport model are simulated as fault zones, and the fault zones are modeled with sorption in both the fracture and matrix continua (SAR Section 2.3.8.5.2.3). The fracture continuum within the fault zones is treated as an equivalent continuum with low porosity and no matrix diffusion, to represent the fracture transport characteristics prevalent in faults in the unsaturated zone. Matrix diffusion is applied to all nodes except those designated as fault nodes in the unsaturated zone (SNL 2008a, Section 6.5.5[b]). Elsewhere in the non-fault zones of the unsaturated zone, sorption in the fracture continuum is conservatively not included (SAR Section 2.3.8.1).

As is the case in the matrix of the non-faulted regions of the unsaturated zone, sorption in the fault zones is modeled using the linear sorption model with a sorption distribution coefficient (K_d), and the K_d distributions for the fault zones are taken from those developed for the remainder of the unsaturated zone (see SAR Section 2.3.8, Table 2.3.8-2). The fracture continuum nodes for the fault zones are assigned to one of the four zones representative of the Tiva Canyon welded (TCw), Paintbrush nonwelded (PTn), Topopah Spring welded (TSw), and Calico Hills nonwelded (CHn) hydrogeologic units (SNL 2008a, Table 6-3) (Note radionuclide transport occurs only through the TSw and CHn units). In the unsaturated zone transport abstraction model, for each sorbing radionuclide, three K_d values are sampled, one each for devitrified, vitrified, and zeolitic rock types. In the rock matrix continuum, the K_d values are assigned according to the 15 elements and 3 rock groups (SAR Table 2.3.8-9). In the fracture continuum of the fault zones, the K_d for the TSw unit is assigned to be the rock-matrix K_d for the devitrified tuff, and the K_d for the CHn unit is assigned to be the rock-matrix K_d for the zeolitic tuff.

In the fault zones, matrix properties are taken to be the same as in the fractured rock mass (SAR Section 2.3.8.4.1).

Therefore, the conceptual model for transport of dissolved or reversibly sorbed radionuclides through the unsaturated zone fault zones is different from the conceptual model for transport of dissolved or reversibly sorbed radionuclides through the remainder of the unsaturated zone in

two aspects: (1) sorption in the fault zones is simulated for both the fracture and the matrix continua; and (2) the fault zones utilize a dual-permeability transport model that considers advection and dispersion without any fracture-matrix diffusive interaction (i.e., matrix diffusion) (SNL 2008b, Section P21).

To have treated sorption in the fault zones differently would not have significantly affected the results. The incorporation of sorption in the fracture continuum of the fault zones in the unsaturated zone is not conservative when compared to the case where sorption is conservatively excluded, because sorption contributes to the retardation of radionuclides. However, this approach is inconsequential as only about 7% of the repository nodes are fault nodes (39 fault nodes out of 560 nodes) and a sensitivity analysis using the TSPA model shows that this treatment has an insignificant impact on the calculated mean annual dose (SNL 2008b, Section P21). The impact analysis considered the Seismic Ground Motion Modeling Case and the Igneous Intrusion Modeling Case, which are the two cases with the highest mean annual dose for the 1,000,000-year simulation duration. For the impact evaluation, the transport characteristics of the fault zones were modified so that the conceptual model for transport through the fault pathways is made similar to the rest of the unsaturated zone transport abstraction model, thus allowing for the fracture–matrix diffusive interaction but no sorption in the fracture continuum of the fault zones. This treatment represents a conservative alternative conceptualization with regard to sorption in the fracture continuum. The mean annual dose for the alternative case is similar with only a small increase (< 5%) during majority of the 1,000,000-year time period simulated. Among the major dose-contributing radionuclides, the doses for ^{226}Ra and ^{237}Np rise slightly (< 5%) as anticipated (SNL 2008b, Figures P-17 and P-19). The overall impact of using these two different treatments of fault zones on the mean annual dose for all modeling cases is small (< 5%) (SNL 2008b, p. P-25).

Similarly, although the assignment of K_ds for the zeolitic rock type to the fracture continuum in all fault nodes in the CHn unit is not a demonstrably conservative approach because K_ds for the zeolitic rock tend to be larger than those for the vitric rock (SAR Table 2.3.8-9), the impact of this approach on the dose calculation is expected to be small because: (1) as mentioned earlier, only about 7% of the repository nodes are located in the fault zones; of these, only a small portion are in the CHn vitric zones; and (2) the TSPA sensitivity analysis described earlier demonstrates that the impact of using zero K_ds for the fracture continuum in all fault zones will be insignificant for the TSPA dose calculations (SNL 2008b, p. P-25).

In summary, fault zones in the unsaturated zone are treated differently from the remainder of the unsaturated zone in two aspects: (1) sorption in the fault zones is simulated for both the fracture and the matrix continua; and (2) the fault zones utilize a dual-permeability transport model that considers advection and dispersion without any fracture-matrix diffusive interaction (i.e., matrix diffusion) (SNL 2008b, Section P21). The sorption coefficient distribution parameters for fault zones are taken from SAR Section 2.3.8, Tables 2.3.8-2 and 2.3.8-9. The TSPA impact analysis shows that the overall impact of using two different treatments of the fault zones (one as currently implemented in the unsaturated zone transport model with sorption in both fracture and matrix continua but without matrix diffusion, and the other allowing for the fracture-matrix diffusive interaction but no sorption in the fracture continuum of the fault zones) on the mean annual dose for seismic ground motion and igneous intrusion modeling cases is small (< 5%).

2. COMMITMENTS TO NRC

None.

3. DESCRIPTION OF PROPOSED LA CHANGE

None.

4. REFERENCES

SNL (Sandia National Laboratories) 2008a. *Particle Tracking Model and Abstraction of Transport Processes*. MDL-NBS-HS-000020 REV 02 AD 02. Las Vegas, Nevada: Sandia National Laboratories. ACC: DOC.20080129.0008; DOC.20070920.0003; LLR.20080325.0287; LLR.20080522.0170.

SNL 2008b. *Total System Performance Assessment Model/Analysis for the License Application.* MDL-WIS-PA-000005 REV 00 AD 01. Las Vegas, Nevada: Sandia National Laboratories. ACC: DOC.20080312.0001; LLR.20080414.0037; LLR.20080507.0002; LLR.20080522.0113.

RAI Volume 3, Chapter 2.2.1.3.7, First Set, Number 3:

Provide the details on how DOE weighted empirical sorption data to develop the cumulative distribution functions.

Basis: In developing the basis for the K_d statistical distributions (SAR, Section 2.3.8.3.1; SNL, 2007, Appendix A and Addendum 1), DOE notes in many places that "As discussed in Section A6, not all the empirical data was equally weighted in selecting the probability distribution as the influence of expected variations in water chemistry, radionuclides, and variations in rock surface properties within each major rock type were incorporated in making the selection." (See, for example, SNL, 2007, Appendix A, Section A8.1.3).

The referenced section (SNL, 2007, Appendix A, Section A6) provides only general information, and does not provide sufficient detail to allow an evaluation of the weighting methodology. For example, it is not clear if the weighting process might result in the removal of some data points from the development of the probability distributions, or if the influence of a subset of the data was increased. This information is needed to evaluate whether acceptance criteria related to system description and data uncertainty in NRC, 2003, Section 2.2.1.3.7.3 are met, and thus verify compliance with 10 CFR 63.114(a) and 63.114(b).

1. RESPONSE

1.1 GENERAL

Use of the term "weight" in *Radionuclide Transport Models Under Ambient Conditions* (SNL 2007a) is not intended to imply a mathematical weighting function. Rather, experimental data, surface-complexation modeling, and ultimately, professional judgment of the author, were all used to develop distribution functions that support K_d values and their uncertainty distributions in TSPA. In this context the term "weight" can be considered essentially synonymous with the term "emphasis."

Criteria used to evaluate experimental sorption data (and other information on radioelement sorption behaviors) and develop distribution functions that support K_d values and their uncertainty ranges in the TSPA are discussed in SAR Sections 2.3.8.2.2 and 2.3.8.3.1, as well as various sections of *Radionuclide Transport Models Under Ambient Conditions* (SNL 2007a) and other supporting documents, as described below. Examples of factors taken into consideration when developing K_d distribution functions for use in TSPA include potential saturation with precipitated radioelement-bearing solids, observed trends in experimental data (e.g., water chemistry and experimental duration), and results from surface-complexation modeling. Pertinent factors are discussed as they apply to specific elements in each relevant subsection of Sections A8 and A2[a] in *Radionuclide Transport Models Under Ambient Conditions* (SNL 2007a). Taken together such considerations and selection criteria reflect the professional judgment of report authors and subject-matter experts (SMEs). Indeed, professional judgment is

an important and legitimate component of K_d selection criteria. Professional judgment is not, however, readily quantified, being based as it commonly must be on subjective criteria (i.e., "judgment") that reflect the cumulative knowledge of an SME's expertise. Factors influencing the development of K_d distribution functions for use in TSPA are outlined in SAR Sections 2.3.8.2.2.2 and 2.3.8.3.1, and are summarized in the following three paragraphs.

Sorption-coefficient data obtained with the natural and surrogate waters were used to derive sorption coefficient distributions for use in unsaturated zone radioelement transport calculations (SNL 2007a, Section A.4). To evaluate the impact of water chemistry on the sorption behavior of the radioelements of interest, laboratory experiments used two natural water compositions (J-13 and UE-25 p#1) intended to be representative of the natural fluids encountered in the unsaturated zone. Sorption experiments were carried out as a function of time, element concentration, atmospheric composition, water composition, particle size, rock type, and temperature. In some cases, solids remaining from sorption experiments were contacted with unspiked (no added radioelements) groundwater in "desorption" experiments. Combined sorption and desorption experiments provide information on forward and backward sorption reaction rates. Because sorption experiments provide a lower bound for K_d relative to desorption experiments, K_d values are primarily set through sorption experiments (SAR Section 2.3.8.3.1, p. 2.3.8-18)

Radioelement sorption coefficients are often a function of dissolved radioelement concentrations (nonlinear sorption isotherms). Most experiments were performed over a range of radioelement concentrations, although K_d values determined from experiments for which dissolved radioelement concentrations exceeded solubility limits were not considered in the derivation of K_d distributions for most elements (based on solubilities available at the time these distributions were developed; however, revised solubility limits in SNL 2007b do not significantly alter data selection criteria). For experiments conducted over a range of radioelement concentrations, the resulting K_d values and probability distributions derived from them account for a dependence on radioelement concentration. The only elements for which the experimental concentrations did not approach a solubility limit were cesium and selenium. Cesium and selenium K_d ranges were adjusted based on expected maximum concentrations in the unsaturated zone, so K_d values would not be overestimated (SNL 2007a, Section A8.2). Thus, K_d distributions for cesium, a strongly sorbing radioelement, were significantly reduced from the experimentally determined values in order to account for potential high cesium concentrations in the unsaturated zone. Potential selenium concentrations in the unsaturated zone that exceed those used in low-concentration sorption experiments may occur in the TSw (close to waste-emplacement drifts), which was accounted for by using a K_d value of zero in the TSw and experimentally supported K_d values in the rest of the unsaturated zone.

Sorption-reaction rates (kinetics) can be a source of uncertainty in batch and column sorption experiments; however, experimentally determined sorption coefficients have a conservative bias (SAR Section 2.3.8.2.2.2). That is, sorption coefficients obtained in relatively short-term experiments can be expected to be smaller than or equal to "effective" sorption coefficients during unsaturated zone transport. Sorption reactions for some radioelements (notably plutonium and radium) have been found to be slow enough that experimentally determined K_d values may not be appropriate for use in TSPA, as these radioelements may not achieve equilibrium during

unsaturated zone transport (SNL 2007a, Sections A8.4.1 and A8.6.1). In such cases, upper bounds on K_d distributions have been reduced relative to the available data in order to better account for potentially slow sorption kinetics (SNL 2007a, Sections A8.4 and A8.6).

Section 6.1.2.3 of *Radionuclide Transport Models Under Ambient Conditions* (SNL 2007a) also discusses general criteria used to evaluate experimental data in the development of distribution functions. It is noted that, "sorption is not only a function of the sorptive strength (as quantified by the value of Kd), but also of the contact time of the radioelements with the rock matrix during transport through the UZ" (SNL 2007a, p. 6-8). Because the use of a K_d assumes thermodynamic equilibrium (see SNL 2007a, Section I.1.3.2), experimentally determined K_ds for each radioelement must therefore be evaluated as a function of experimental duration to determine the relative effects of sorption kinetics (SNL 2007a, p. 6-8). Furthermore, "Kd values obtained from experiments involving low concentration solutions tend to be higher than those from higher concentration ones because the most active sorption sites are immediately occupied by the dilute solutes … The obvious implication is that K_d values from experiments involving concentrations similar to those expected in the field should be used to avoid overestimation or underestimation" (SNL 2007a, p. 6-8). In addition, another reason to deemphasize or omit the lowest K_d values from some sorption experiments is that natural waters contain background concentrations of many elements for which sorption data are reported, including uranium, barium, cesium, strontium, thorium, and protactinium. Yucca Mountain site waters used in many sorption experiments (e.g., J-13, UE-25 p#1) also contain natural concentrations of these same elements of interest (SNL 2007a, p. A-4). During sorption experiments, these background concentrations are sorbed to solid phases along with the radioactive isotopes used in the experiments. Thus, the initial concentrations of these elements-of-interest may be higher in these sorption experiments than concentrations calculated based only on activities of radioactive isotopes used in the experiments. Including sorption-coefficient data from experiments containing natural background concentrations generally tends to underestimate retardation potential (SNL 2007a, p. A-4).

Surface-complexation modeling, combined with existing literature data, was used to inform professional judgment when developing K_d distribution functions and their uncertainty ranges for uranium, plutonium, neptunium, and americium (Group I), as discussed in *Radionuclide Transport Models Under Ambient Conditions* (SNL 2007a, Section A1[a], "Approach To The Derivation Of K_d Ranges For Major Rock Types In The Yucca Mountain Flow System," p. A-2):

> [K_d] distributions were derived from available project data combined with external data … [which] … provided further insights into how other variables affect sorption behavior. PHREEQC model results were used to assess how water chemistry and surface area affect sorption behavior. …. Chemical insights regarding the kinds of reactions involved were also used. These insights included potential impacts from variations in water compositions (e.g., Eh) outside those addressed in the experimental program … [and] … an attempt was made to emphasize those experiments that used samples closest to the mean composition of the hydrologic units as defined in the transport model. … To incorporate uncertainties in project and literature data and their application for this purpose,

> the results were conservatively biased by selecting values at the low ends of the ranges."

Inputs to and use of outputs from surface-complexation modeling of Group I elements are provided in Appendix L of *Radionuclide Transport Models Under Ambient Conditions* (SNL 2007a, Section L3), which further clarifies that, "results of this modeling, in conjunction with the experimental data, inform the process of expert judgment to arrive at the uncertainty distributions for sorption coefficients for Am (Appendix A8.1), Np (Appendix A8.3), Pu (Appendix A8.4), and U (Appendix A8.9)."

Finally, valuable insight into the author's ultimate reliance on his professional judgment to develop distribution functions that support K_d values and their ranges for use in performance assessment can be found in historical project documents. For example, the author has stated that "expert judgment has been applied in order to generalize sorption behavior expected under diverse natural conditions, based on data collected from a very limited number of samples and under very restricted environmental conditions in the laboratory;" that K_d values "reflect the current best judgment of the investigator…;" and that "the investigator also used his best judgment for estimating distribution parameter values for the unsaturated zone."

1.1.1 Discussions of Individual K_d Distributions

Distribution functions for radioelements with K_d values greater than zero are described in Sections A8 and A2[a] of *Radionuclide Transport Models Under Ambient Conditions* (SNL 2007a). As discussed in SAR Section 2.3.8.2.2.2, sorption reactions for the radioelements of interest include ion-exchange reactions and surface-complexation reactions. Ion-exchange reactions involve exchange of a radioelement with ionic constituents on exchange sites in minerals such as zeolites and clays. These exchange reactions are most relevant for radioelements that occur as simple aqueous ions, such as cesium, strontium, and radium. Surface-complexation reactions involve adsorption of radioelements onto oxide surfaces. Radioelements that sorb primarily by surface complexation include americium, neptunium, uranium, plutonium, protactinium, and thorium (SAR Section 2.3.8.3.1). Radioelements for which sufficient data on surface-complexation constants were available (uranium, plutonium, neptunium, americium) comprise the first group of radioelements discussed in Section 1.1.1.1 (Group I), and their sorption behaviors were modeled by using the software code PHREEQC (V2.3, STN: 10068-2.3-00) (see Section A7 of SNL 2007a for more detail). The second group of radioelements (Group II) consists of the remaining radioelements whose sorption behaviors were not modeled with surface complexation, either because of insufficient data for surface-complexation constants or because these elements sorb primarily through ion exchange. (K_d values for carbon, iodine, technetium, and chlorine are all set to zero and are not discussed further here).

Subsequent to completion of the SAR, errors in classifications of tuff rock-types used in sorption–coefficient measurements were identified for uranium, plutonium, americium, thorium, and strontium; however, rectifying the affected K_d measurements after correcting previous rock misclassifications has a negligible effect on TSPA dose calculations, and no changes were made to K_d distributions used in TSPA.

1.1.1.1 Group I

For the four actinides (uranium, plutonium, neptunium, and americium) K_d distributions are developed with the aid of surface-complexation modeling (using PHREEQC) that supplement experimental sorption data and inform professional judgment. Some experimental sorption data were excluded from consideration when developing K_d distribution functions, based in part on professional judgment. Explanations for data selection/exclusion and the rationale used for developing distribution functions to support K_d values and their uncertainty distributions for each actinide in this group are provided in the relevant subsection of Section A8 of *Radionuclide Transport Models Under Ambient Conditions* (SNL 2007a) and are abstracted in Sections 1.1.1.1.1 to 1.1.1.1.4.

1.1.1.1.1. Uranium

Table 1.1.1.1.1 Uranium K_d Distribution Functions for Unsaturated Zone Rock Types

Species	Rock Type	Distribution	Coefficients Describing Distribution (mL/g)
Uranium	Zeolitic	Cumulative	(K_d, *probability*) (0, 0) (0.5, 0.5) (30, 1.0)
	Devitrified	Cumulative	(K_d, *probability*) (0, 0) (0.2, 0.5) (4, 1.0)
	Vitric	Cumulative	(K_d, *probability*) (0, 0) (0.2, 0.5) (3, 1.0)

Source: SNL 2007a, Table 6-1[a].

a. **Section A8.9.1 Devitrified Tuff**: Negative K_d values were omitted. Experimentally determined sorption coefficients for uranium sorption on devitrified tuffs show no correlation with final uranium solution concentrations. Experimental data show no clear relationship between K_d values and pH, whereas surface-complexation modeling predicts K_d to decrease with increasing pH (SNL 2007a, Figure A-62, p. A-77). Professional judgment guided by the experimental data and modeling results led to selection of a cumulative probability distribution for uranium sorption on devitrified tuff that ranges from 0 to 4 mL/g, which emphasizes values lower than most determined experimentally (Table 1.1.2-1 and Figure 1.1.2-1).

b. **Section A8.9.2 Zeolitic Tuff**: Experimental data suggest a very weak positive correlation with pH, whereas surface-complexation modeling predicts the opposite effect, although small. No correlation between K_d and final uranium concentration or with increased experimental duration is evident, suggesting that uranium sorption is fast. Professional judgment guided by the experimental data and modeling results led to selection of a cumulative probability distribution for uranium sorption on zeolitic tuff that ranges from 0 to 30 mL/g, lower than the range observed experimentally (Table 1.1.2-1 and Figure 1.1.2-1).

c. **Section A8.9.3 Vitric Tuff**: Beyond three days' duration, no clear correlation is evident between sorption coefficients and experimental duration. No surface-complexation modeling was performed for uranium sorption on vitric tuff. Professional judgment guided by the experimental data led to selection of a

cumulative probability distribution for uranium sorption on vitric tuff that ranges from 0 to 3 mL/g, which emphasizes values lower than most determined experimentally (Table 1.1.2-1 and Figure 1.1.2-1).

1.1.1.1.2. Plutonium

Table 1.1.1.1.2 Plutonium K_d Distribution Functions for Unsaturated Zone Rock Types

Species	Rock Type	Distribution	Coefficients Describing Distribution (mL/g)
Plutonium	Zeolitic	Cumulative	(K_d, *probability*) (10, 0) (100, 0.5) (200, 1.0)
	Devitrified	Cumulative	(K_d, *probability*) (10, 0) (70, 0.5) (200, 1.0)
	Vitric	Cumulative	(K_d, *probability*) (10, 0) (100, 0.5) (200, 1.0)

Source: SNL 2007a, Table 6-1[a].

a. **Section A8.4.1 Devitrified Tuff**: Observed trends in sorption and desorption data suggest convergence to values between about 100 and 1,000 mL/g after more than about 100 days. The earliest experimental sorption data indicating K_d values above 1,000 mL/g reflect samples with considerable clay or zeolite, and these were omitted from consideration (see SNL 2007a, p. A-40). To examine the effect of Eh on plutonium sorption, surface-complexation modeling was used to calculate plutonium sorption coefficients as a function of Eh (SNL 2007a, Figure A-33a, p. A-43). Results of this modeling suggest that tetravalent plutonium will be the dominant oxidation state of sorbed plutonium for most Yucca Mountain groundwaters. However, in the absence of definitive data on the actual oxidation state of sorbed plutonium in the experiments, the experimentally determined sorption coefficient values were used to derive the distribution function. The plutonium sorption-coefficient probability distribution derived for devitrified tuff in the unsaturated zone is a cumulative distribution ranging from 10 to 200 mL/g. Based on professional judgment, that is, by taking into account potentially slow sorption kinetics of plutonium (SAR Section 2.3.8.2.2.2), the low end of the K_d distribution is selected as equal to one-tenth of the minimum long-term K_d value in order to account for the possibility of relatively fast transport in the unsaturated zone, as well as to capture potential impacts of experimental variations in water chemistry, plutonium concentrations (up to the solubility limit), and sample surface area. The upper limit of the selected distribution, which deemphasizes the highest empirical K_d values (Table 1.1.2-1), accounts for potential impacts of sorption kinetics during potentially fast transport in the unsaturated zone.

b. **Section A8.4.2 Zeolitic Tuff**: Observed trends in the sorption and desorption data suggest eventual convergence to values between about 100 and 1,000 mL/g, similar to the range for devitrified tuffs. The plutonium sorption-coefficient probability distribution derived for zeolitic tuff in the unsaturated zone is a cumulative distribution ranging from 10 to 200 mL/g. Based on professional judgment, the median K_d value was increased from 70 mL/g for devitrified tuff to 100 mL/g for zeolitic tuff in order to reflect the higher K_d values obtained with zeolitic tuff at lower pH values (7 to 7.5).

c. **Section A8.4.3 Vitric Tuff**: Observed trends in sorption and desorption data suggest eventual convergence to values between about 100 and 1,000 mL/g, similar to values for devitrified and zeolitic tuffs. The plutonium sorption-coefficient probability distribution selected for vitric tuff in the unsaturated zone is a cumulative distribution ranging from 10 to 200 mL/g. By taking into account potentially slow sorption kinetics of plutonium (SAR Section 2.3.8.2.2.2), the lower value is selected as equal to one-tenth of the minimum long-term K_d value in order to account for potential fast transport through the unsaturated zone. The median value of 100 mL/g was selected to be equal to the median value among K_d values obtained from experiments with synthetic UE-25 p#1 water and to account for the effect of UE-25 p#1 water chemistry.

1.1.1.1.3. Neptunium

As discussed below, several neptunium sorption experiments that could have been oversaturated with respect to Np_2O_5 or NpO_2 were omitted from the developed K_d distribution functions, including four experiments conducted with devitrified tuff (i.e., four K_d values from experiments with sample GU3-0433) and eight experiments conducted with zeolitic tuff (i.e., eight K_d values from experiments with sample G4-1608).

Table 1.1.1.1.3 Neptunium K_d Distribution Functions for Unsaturated Zone Rock Types

Species	Rock Type	Distribution	Coefficients Describing Distribution (mL/g)
Neptunium	Zeolitic	Cumulative	(*K_d*, *probability*) (0, 0) (0.5, 0.5) (6, 1.0)
	Devitrified	Cumulative	(*K_d*, *probability*) (0, 0) (0.5, 0.5) (6, 1.0)
	Vitric	Cumulative	(*K_d*, *probability*) (0, 0) (1.0, 0.5) (3, 1.0)

Source: SNL 2007a, Table 6-1[a].

a. **Section A8.3.1 Devitrified Tuff**: Experimental K_d data show a dependence on final neptunium solution concentration, and four K_d values from experiments with sample GU3-0433 suspected of being oversaturated with respect to Np_2O_5 were not used to evaluate the K_d cumulative probability distribution. Surface-complexation modeling was performed for neptunium sorption on devitrified tuff, and a potential interpretation of those results is that the sorption experiments had not reached equilibrium. The neptunium sorption-coefficient probability distribution selected for devitrified tuff in the unsaturated zone is a cumulative distribution ranging from 0 to 6 mL/g. The low end of the range was selected to agree with the minimum value obtained in short-term experiments ($\leq$ 21 days). The upper end of the distribution, which deemphasizes the highest empirical K_d values, is a minimum upper limit for neptunium concentrations near the solubility limit, emphasizing results from experiments with UE-25 p#1 water near pH 7, and well below that determined experimentally (Table 1.1.2-1 and Figure 1.1.2-1).

b. **Section A8.3.2 Zeolitic Tuff**: Experimental K_d data show a clear dependence on final neptunium solution concentration, and eight K_d values from experiments with sample G4-1608, suspected of being oversaturated with respect to Np_2O_5 or NpO_2 were not used to evaluate the K_d cumulative probability distribution. A clear dependence of sorption coefficient on water chemistry is evident for short-term experiments with J-13 and UE-25 p#1 waters. No surface-complexation modeling was performed for neptunium sorption on zeolitic tuff. The neptunium sorption-coefficient probability distribution selected for zeolitic tuff in the unsaturated zone is a cumulative distribution ranging from 0 to 6 mL/g. The low end of the range was selected to agree with the minimum value obtained in short-term experiments (≤ 21 days). The upper end of the distribution, which deemphasizes the highest empirical K_d values, is a minimum upper limit for neptunium concentrations near the solubility limit, emphasizing results from experiments with UE-25 p#1 water near pH 7, and well below that determined experimentally (Table 1.1.2-1 and Figure 1.1.2-1).

c. **Section A8.3.3 Vitric Tuff**: Experimental K_d data show a clear dependence on final neptunium solution concentration, and several results from experiments suspected of being oversaturated with respect to Np_2O_5 or NpO_2 were not used to evaluate the K_d cumulative probability distribution. No surface-complexation modeling was performed for neptunium sorption on vitric tuff. The neptunium sorption-coefficient probability distribution selected for vitric tuff in the unsaturated zone is a cumulative distribution ranging from 0 to 3 mL/g. The low end of the range is selected to agree with the minimum value obtained in short-term experiments (≤ 21 days). The upper end of the distribution, which deemphasizes the highest empirical K_d values, is a minimum upper limit for neptunium concentrations near the solubility limit, emphasizing results from experiments with UE-25 p#1 water near pH 7, and well below that determined experimentally (Table 1.1.2-1 and Figure 1.1.2-1).

1.1.1.1.4. Americium

Table 1.1.1.1.4 Americium K_d Distribution Functions for Unsaturated Zone Rock Types

Species	Rock Type	Distribution	Coefficients Describing Distribution (mL/g)
Americium	Zeolitic	Truncated Log-Normal	Range = 1,000 to 10,000 Mean = 5500 Std Dev = 1,500
	Devitrified	Truncated Log-Normal	Range = 1,000 to 10,000 Mean = 5500 Std Dev = 1,500
	Vitric	Cumulative	(K_d, *probability*) (100, 0) (400, 0.5) (1,000, 1.0)

Source: SNL 2007a, Table 6-1[a].

a. **Section A8.1.1 Devitrified Tuff**: Because calculated final solution concentrations of americium exceeded the solubility of $Am(OH)CO_3$ in several experiments, the results for experiments with samples JA-32 and YM-54 were omitted from consideration. K_d values for the remaining experiments range from 1,000 mL/g to more than 10,000 mL/g, and show little or no sensitivity to experimental duration or variations in pH between approximately pH 7.8 and 9.2

(SNL 2007a, Figure A-3, p. A-18). Results from surface-complexation modeling of americium sorption onto quartz (SiO_2) are consistent with the experimental results and indicate that K_d values for americium decrease as pH increases from 7 to 9. In terms of pH, experimentally determined K_ds are therefore considered to be at the low end of the range expected in the unsaturated zone. The distribution function selected for americium sorption coefficients in devitrified tuffs in the unsaturated zone is a truncated log-normal distribution ranging from 1,000 to 10,000 mL/g, comparable to the range of experimentally determined K_d values (Table 1.1.2-1 and Figure 1.1.2-1).

b. **Section A8.1.2 Zeolitic Tuff**: Calculated final solution concentrations of americium were close to (but below) the solubility of $Am(OH)CO_3$ only for sample G2-1952, although sorption coefficients obtained for this sample were considered when developing the K_d distribution function (SNL 2007a, p. A-14), thereby accounting for potentially elevated americium concentrations in the unsaturated zone. The distribution function selected for americium sorption coefficients in zeolitic tuffs in the unsaturated zone is a truncated log-normal distribution ranging from 1,000 to 10,000 mL/g (identical to the K_d distribution function developed for americium sorption on devitrified tuff). The upper end of this distribution is well below the upper limit of experimentally determined K_d values (Table 1.1.2-1 and Figure 1.1.2-1).

c. **Section A8.1.3 Vitric Tuff**: Americium sorption data obtained by using samples GU3-1203, GU3-1301, and JA-18 were not included in the derivation of the distribution function because the final solutions in experiments that used these samples were oversaturated with respect to $Am(OH)CO_3$. Because the pH dependence of K_d values for americium sorption on vitric tuffs is inferred to be similar to that for devitrified tuffs (SNL 2007, p. A-19), and because sorption experiments with vitric tuffs were carried out at the high end of the pH range expected in the natural system, sorption coefficients in the natural system might be expected to be larger than those observed experimentally. However, vitric units have the potential to have surface areas substantially smaller than those reported for vitric tuff in *Radionuclide Transport Models Under Ambient Conditions* (SNL 2007a, Table A-1). Taking such opposing considerations into account, a cumulative distribution function is selected for americium sorption coefficients in vitric tuffs in the unsaturated zone that ranges from 100 to 1,000 mL/g, considerably lower than experimentally determined values (Table 1.1.2-1 and Figure 1.1.2-1).

d. A reevaluation of rock-type assignments led to reclassification of sample JA-18 as vitric (rather than zeolitic); however, K_d values determined from experiments that used sample JA-18 were not considered when deriving any K_d distribution functions because the final solutions in experiments that used this sample were judged to be oversaturated with respect to $Am(OH)CO_3$, so there is no affect on the selected K_d distributions used in TSPA.

1.1.1.2 Group II

Experimental data used to develop distribution functions of K_d values for seven elements were not complemented with results of surface-complexation modeling; these are, protactinium, cesium, strontium, radium (based largely on sorption data for barium), thorium, selenium and tin.

1.1.1.2.1. Protactinium

Very few experimental data are available on protactinium chemistry or its sorption behavior. Berry et al. (1989, Table 15) report dissolved concentrations of protactinium measured in selected groundwaters (filtered) fall within the range 1.4×10^{-14} to 1.4×10^{-12} mol/L. Allard et al. (1983, p. 12) reported protactinium sorption coefficients for experiments with a silica sample having a surface area similar to that measured for devitrified tuffs, and using a solution composition of 0.01 M $NaClO_4$. The initial protactinium concentration in all their experiments was 4.0×10^{-12} mol/L. Allard's data indicate that protactinium sorption coefficients vary substantially (approximately 2 orders of magnitude) as a function of pH. Over the pH range expected in unsaturated zone waters at Yucca Mountain (7 to 8.5), sorption coefficients reported by Allard et al. (1983, p. 12) range from approximately 7,500 to 20,000 mL/g; similar results were reported for protactinium sorption on alumina. Insufficient thermodynamic data precluded using surface complexation to model the sorption behavior of protactinium.

Table 1.1.1.2.1 Protactinium K_d Distribution Functions for Unsaturated Zone Rock Types

Species	Rock Type	Distribution	Coefficients Describing Distribution (mL/g)
Protactinium	Zeolitic	Truncated Log-Normal	Range = 1,000 to 10,000, Mean = 5500, Std Dev = 1,500
	Devitrified	Truncated Log-Normal	Range = 1,000 to 10,000, Mean = 5500, Std Dev = 1,500
	Vitric	Truncated Log-Normal	Range = 1,000 to 10,000, Mean = 5500, Std Dev = 1,500

Source: SNL 2007a, Table 6-1[a].

a. **Section A8.5.1 Devitrified Tuff**: No experimentally determined K_ds are available for protactinium sorption on devitrified tuffs from Yucca Mountain, and the K_d range chosen for americium sorption on devitrified tuffs is used instead (1,000 to 10,000 mL/g). This range is well within the range of K_ds reported by Allard et al. (1983, p. 12) for sorption of protactinium to silica and alumina above pH 6.8 (SNL 2007a, Figure A-40, p. A-51). As for americium, a truncated log-normal distribution was selected (SNL 2007, Section A8.1). The selection of this K_d range for protactinium sorption on devitrified tuff is compatible with the study of Berry et al. (1989, p. 347), who reported a K_d range of 1,000 to 1,000,000 mL/g for protactinium sorption on natural rock samples, including sandstone, shale, granite, and clay in contact with natural groundwaters.

b. **Section A8.5.2 Zeolitic Tuff**: Experimentally determined sorption coefficients for protactinium sorption on zeolitic tuffs from Yucca Mountain in J-13 water range from 3.3 to 10.1 mL/g. Initial solution concentrations in those experiments ranged from 1×10^{-11} to 5×10^{-14} molar, and it is possible that protactinium in those sorption experiments co-precipitated with one or more other readily

hydrolyzed species (SNL 2007a, p. A-52). Final solution pH values for the experiments on the Yucca Mountain samples ranged from 6.3 to 6.7. However, because pH values measured in natural waters in the unsaturated zone range from 6.7 to 9.7 (SNL 2007a, Section A4, Table A-2), the experimental sorption coefficients are not considered directly applicable to Yucca Mountain unsaturated zone conditions. The apparent sorption edge reported by Allard et al. (1983, p. 12) above pH 6.8, along with the fact that the surface area of zeolitic tuff tends to be greater than that of devitrified tuff, led to the selection of the distribution function for protactinium sorption on devitrified tuff being used for protactinium sorption on zeolitic tuff as well (i.e., equal to that of americium sorption on devitrified tuff).

c. **Section A8.5.3 Vitric Tuff**: Again, with no experimental data available for protactinium sorption on vitric tuffs, the K_d distribution function selected for protactinium sorption on devitrified tuffs is also used for protactinium sorption on vitric tuff (i.e., also that of americium on devitrified tuff). This selection is rationalized by the fact that vitric tuffs have surface areas similar to those of devitrified tuffs (SNL 2007a, p. A-52).

d. Additional information from the literature support treating protactinium as a strongly sorbing element. For example, Vine et al. (1980, p. 65) note that strong sorption of ^{233}Pa onto Yucca Mountain rock thin sections interfered with microautoradiography measurements of ^{237}Np sorption on those thin sections. Myasoedov et al. (2006) state that pentavalent protactinium "exhibits an extraordinarily high tendency … to be adsorbed on almost any available surface", although Kirby (1959) claims that, "The well-publicized tendency of protactinium to deposit on the walls of glass vessels is primarily due to its insolubility …." Keller (1966) points out that "it is impossible in practice to obtain solutions of Pa(V) which remain stable for a long period [and] it is … believed that the irreversible changes are due not to hydrolysis, but to condensation reactions." Baes and Mesmer (1976) declare that, "The great difficulty of maintaining Pa(V) in aqueous solution without hydrolytic precipitation … is perhaps the best known feature of the aqueous chemistry of this element." Trubert et al. (2001) affirm that protactinium is "characterized by a strong tendency toward hydrolysis and colloid and polymer formation" and note that "in the absence of a strong complexing agent, the high affinity of Pa(V) for any solid support and impurities in solution enhances experimental difficulties." Finally, Kulmala et al. (1998) reported sorption coefficients (K_ds) for protactinium sorption onto rock samples of granodiorite and granite gneiss (Finnish repository program) using natural groundwaters and measured under oxic and anoxic (N_2) atmospheres. The values thus obtained were 0.2 to 3.1 and 0.07 to 12 $m^3\ kg^{-1}$ for oxic and anoxic atmospheres, respectively. These values correspond to 200 to 3,100 mL/g (oxic) and 70 to 12,000 mL/g (anoxic), K_d ranges that bracket those selected for protactinium sorption onto all three unsaturated zone rock types: 1,000 to 10,000 mL/g.

1.1.1.2.2. Cesium

Among those radioelements with TSPA K_d values greater than zero, cesium is the only element for which experimental concentrations never approached a solubility limit. The solubility of cesium compounds is very high in Yucca Mountain waters (SNL 2007b, Section 6.17), and the sorption coefficient probability distributions for cesium were developed by accounting for potential concentrations of cesium in the unsaturated zone.

Table 1.1.1.2.2 Cesium K_d Distribution Functions for Unsaturated Zone Rock Types

Species	Rock Type	Distribution	Coefficients Describing Distribution (mL/g)
Cesium	Zeolitic	Cumulative	(K_d, *probability*) (425, 0) (5,000, 0.5) (20,000, 1.0)
	Devitrified	Uniform	Range = 1 to 15
	Vitric	Cumulative	(K_d, *probability*) (0, 0) (2, 0.5) (100, 1.0)

Source: SNL 2007a, Table 6-1[a].

a. **Section A8.2.1 Devitrified Tuff**: The probability distribution developed for cesium K_d values in contact with devitrified tuff in the unsaturated zone is a uniform distribution with a range of 1 to 15 mL/g (SNL 2007a, Table 6-1[a]). Although most sorption experiments resulted in K_d values greater than 100 mL/g (and up to 1,000 mL/g), the highest K_d values correspond predominantly to experiments carried out at cesium concentrations below 1.0×10^{-6} mol/L, whereas higher cesium concentrations resulted in K_d values between 10 and 100 mL/g. For this reason, the selected distribution was chosen based on professional judgment to acknowledge the potential for high cesium concentrations (e.g., greater than 10^{-3} mol/L) to be transported in the unsaturated zone. A uniform distribution equally weights K_d values within the selected range.

b. **Section A8.2.2 Zeolitic Tuff**: The probability distribution developed for cesium K_d values in contact with zeolitic tuff in the unsaturated zone is a cumulative distribution ranging from 425 mL/g to 20,000 mL/g; whereas, the range of measured cesium sorption coefficients for zeolitic tuffs is 3,500 to 72,000 mL/g.. The low end of this distribution was selected based on professional judgment to acknowledge the potential for high cesium concentrations and lower-than-average ion-exchange capacities in zeolitic tuff during transport in the unsaturated zone. The middle value of the distribution (5,000 mL/g) was selected, based on professional judgment, as being a representative value for dissolved cesium concentrations below 10^{-4} mol/L. The upper end of the range was selected, also based on professional judgment, as a minimum upper limit, given the potential impact of lower cesium solution concentrations and higher-than-average ion exchange capacities. The large range in sorption coefficients obtained at a given duration mainly reflects variations in cesium solution concentrations, although there must also be some contribution from variations in ion exchange capacities of the zeolitic tuff samples used in the experiments (SNL 2007a, p. A-25).

c. **Section A8.2.3 Vitric Tuff**: The probability distribution developed for cesium K_d values in contact with zeolitic tuff in the unsaturated zone is a cumulative distribution ranging from 0 to 100 mL/g. Based on professional judgment, the low-end value was selected to acknowledge the possibility of elevated dissolved cesium concentrations in the unsaturated zone and the possibility that surface areas in vitrophyric rocks may be small. The middle value (2 mL/g) was selected, based on professional judgment, to be representative of expected rock surface areas, high cesium concentrations, and water chemistries such as that from well UE-25 p#1. The upper end of the distribution, which deemphasizes the highest empirical K_d values, is selected to be a minimum upper limit that accounts for the potential impact of lower dissolved cesium on sorption (see SNL 2007, Figure A-15, p. A-26), greater rock surface areas in ash layers, and more dilute water chemistries, such as that from well J-13.

1.1.1.2.3. Strontium

Table 1.1.1.2.3 Strontium K_d Distribution Functions for Unsaturated Zone Rock Types

Species	Rock Type	Distribution	Coefficients Describing Distribution (mL/g)
Strontium	Zeolitic	Uniform	Range = 50 to 2,000
	Devitrified	Uniform	Range = 10 to 70
	Vitric	Uniform	Range = 0 to 50

Source: SNL 2007a, Table 6-1[a].

a. **Section A8.7.1 Devitrified Tuff**: At the time the K_d distribution was being developed, five experiments with devitrified were noted to have final strontium concentrations oversaturated with respect to strontianite ($SrCO_3$) (see SNL 2007a, p. A-62). Several rock samples used in those experiments were subsequently reclassified, and an evaluation of the reclassified data reveals that 22 experiments with devitrified tuff appear to have been oversaturated, including 18 that used sample G1-2840 and four that used sample YM-22. The reclassified K_d values are compared against the K_d distribution selected for use in TSPA in section 1.1.2 below, including omission of these 22 oversaturated experiments from Table 1.1.2-1 and Figure 1.1.2-1. The probability distribution developed for strontium K_d values in contact with devitrified tuff in the unsaturated zone is a uniform distribution with a range of 10 to 70 mL/g. (SNL 2007a, Table 6-1[a]). Based on professional judgment, the low end of the range was selected to correspond to the minimum value observed in isotherm experiments, including the effect of nonlinear isotherms. The upper end of the distribution was chosen, based on professional judgment, as a minimum upper limit to account for the potential impact on strontium sorption due to naturally occurring strontium in pore waters (SNL 2007a, p. A-64). A uniform distribution was chosen in order to equally weight sorption coefficient values in the selected range.

b. **Section A8.7.2 Zeolitic Tuff**: At the time the K_d distribution for TSPA was developed, oversaturation with respect to strontianite in the strontium sorption

experiments with zeolitic tuff was deemed not an issue (SNL 2007a, p. A-66). An evaluation of reclassified data reveals that two experiments that used zeolitic-tuff sample YM-38 appear to have been oversaturated, and two K_d values obtained from these two experiments are omitted from Table 1.1.2-1 and Figure 1.1.2-1. The probability distribution developed for strontium K_d values in contact with zeolitic tuff in the unsaturated zone is a uniform distribution with a range of 50 to 2,000 mL/g, well below the range of K_d values from the sorption experiments (up to 100,000 mL/g). The low end of the range was selected to correspond with the minimum value observed in isotherm experiments and to account for the trend of lower sorption coefficients with increasing strontium concentration, which, when extended to the solubility limit for strontianite in UE-25 p#1 water, indicates a K_d value well below 1,000 mL/g. Based on professional judgment, a lower-end K_d value of 50 mL/g was chosen as being conservative, and the upper end of the distribution, which deemphasizes the highest empirical K_d values, was chosen as a minimum upper limit that accounts for the potential impact on strontium sorption due to naturally occurring strontium in pore waters, which indicate a sorption coefficient of approximately 2,000 mL/g for dissolved strontium concentrations in Yucca Mountain waters (see SNL 2007a, p. A-64). A uniform distribution was chosen to equally weight the sorption coefficient values in the selected range.

c. **Section A8.7.3 Vitric Tuff**: Calculated final solution strontium concentrations in all strontium sorption experiments with vitric tuff were below saturation with respect to strontianite (SNL 2007a, p. A-67), which remains true following a reclassification of rock types used in the experiments. The cumulative probability distribution developed for strontium K_d values in contact with vitric tuff in the unsaturated zone is a uniform distribution with a range of 0 to 50 mL/g. The low end of the range was selected to be consistent with the minimum K_d determined from experiments with UE-25 p#1 water and to account for the possibility that, when combined with naturally occurring strontium, solution concentrations of strontium may approach saturation with respect to strontianite ($SrCO_3$). The upper end of the distribution, which deemphasizes the highest empirical K_d values, is chosen to be a minimum upper limit in J-13 water containing natural strontium, well below maximum experimentally determined K_d values (Table 1.1.2-1 and Figure 1.1.2-1). A uniform distribution was chosen to equally weight K_d values within the selected range.

1.1.1.2.4. Radium

Due to their similar chemistries and the relative ease by which radioactive barium can be measured, barium sorption coefficients are used as proxies for radium K_d values. A limited number of separate experiments were performed with radium to confirm its sorption behavior relative to barium.

Table 1.1.1.2.4 Radium K_d Distribution Functions for Unsaturated Zone Rock Types

Species	Rock Type	Distribution	Coefficients Describing Distribution (mL/g)
Radium	Zeolitic	Uniform	Range = 1,000 to 5,000
	Devitrified	Uniform	Range = 100 to 1,000
	Vitric	Uniform	Range = 50 to 600

Source: SNL 2007a, Table 6-1[a].

a. **Section A8.6.1 Devitrified Tuff**: Measured K_d values show a general increase with decreasing barium (or radium) concentration, suggesting nonlinear isotherms for barium sorption onto devitrified tuff, the impact of which was accounted for when selecting the K_d probability distribution (SNL 2007a, p. A-54). Because two experiments with samples YM-22 had dissolved barium concentrations close to saturation with respect to barite ($BaSO_4$), the effect of nonlinear isotherms was also accounted for when developing the final K_d distribution. In addition, results from one sorption experiment (sample YM-22) were omitted from consideration due to likely saturation (SNL 2007a, p. A-53). The probability distribution developed for radium K_d values in contact with vitric tuff in the unsaturated zone is a uniform distribution with a range of 100 to 1,000 mL/g, the range over which experimentally determined K_d values appear to converge over time (SNL 2007a, p. A-54). A uniform distribution equally weights K_d values within the selected range. The low end of the chosen range was selected based on the minimum value observed in long-term experiments (greater than 40 days), and, based on professional judgment, to account for the potential impact of variations in water chemistry and rock surface areas among devitrified tuffs at Yucca Mountain. The upper end of the distribution, which deemphasizes the highest empirical K_d values, is chosen to be a minimum upper limit, given the potential impact of sorption kinetics, radium solution concentrations, and variation in surface areas. The resulting K_d distribution range is lower than the experimentally determined range (Table 1.1.2-1 and Figure 1.1.2-1).

b. **Section A8.6.2 Zeolitic Tuff**: Essentially all experimentally determined sorption coefficients exceed a value of 10,000 mL/g, and some desorption experiments approach values of 1,000,000 mL/g (SNL 2007a, p. A-56). Unlike sorption experiments conducted on devitrified tuff, there is no clear trend in barium/radium K_d values as functions of water chemistry, barium concentration, or experimental duration. The probability distribution developed for radium K_d values in contact with zeolitic tuff in the unsaturated zone is a uniform distribution with a range of 1,000 to 5,000 mL/g. A uniform distribution equally weights K_d values within the selected range. The low end of the distribution was selected to account for the possibility that at radium concentrations near a solubility limit, sorption coefficients may be lower than the minimum value observed in long-term experiments (that is, isotherms may be nonlinear) and that rock chemistry may show greater variation than that represented by the samples used in the experiments. The upper end of the distribution, which deemphasizes the highest

empirical K_d values, is chosen to be a minimum upper limit, given the potential impacts of radium solution concentrations and variations in rock chemistry.

c. **Section A8.6.3 Vitric Tuff**: Sorption coefficient values determined for radium are larger than those of barium for similar solution concentrations, indicating that barium sorption coefficients provide a conservative estimate of radium sorption coefficients on vitric tuff. Sorption data show a general increase in sorption coefficient with decreasing barium (and radium) concentration, suggesting a nonlinear sorption isotherm and is accounted for in development of the K_d distribution function. Sorption coefficients determined from experiments that used UE-25 p#1 water are lower than those determined from experiments with J-13 water, indicating a groundwater-composition effect for barium/radium sorption onto vitric tuff. The probability distribution developed for radium K_d values in contact with vitric tuff in the unsaturated zone is a uniform distribution with a range of 50 to 600 mL/g, lower than the experimentally determined range of up to about 5,000 mL/g (Table 1.1.2-1 and Figure 1.1.2-1). A uniform distribution equally weights K_d values within the selected range. The lower value is based on experiments with UE-25 p#1 water. The upper limit of the distribution, which deemphasizes the highest empirical K_d values, is a minimum upper limit that acknowledges the potential impact of more dilute water chemistries and the potential for elevated radium concentrations near the solubility limit.

1.1.1.2.5. Thorium

TSPA-LA Sorption Coefficients

The following ranges for sorption coefficients for sorption of thorium on tuff in the unsaturated volcanic section at Yucca Mountain are reported in SAR Table 2.3.8-2, all with uniform distributions (Table 1.1.1.2.5):

Devitrified:	1,000 to 10,000 mL/g
Vitric:	1,000 to 10,000 mL/g
Zeolitic:	1,000 to 30,000 mL/g.

The bases for these distributions are described in *Radionuclide Transport Models Under Ambient Conditions* (SNL 2007, Section A8.8). The approach used to determine ranges and distributions is the same for all three types of tuff. Experimental data, both with Yucca Mountain tuffs and waters, as well as data from studies unrelated to Yucca Mountain, were evaluated to determine what influences the extent of thorium sorption. However, available data are sparse. Therefore, professional judgment was used to decide which effects and which experimental data should be given greater emphasis in determining the sorption coefficient distributions. As discussed in *Radionuclide Transport Models Under Ambient Conditions* (SNL 2007a, Section A8.8.1), the results of experiments oversaturated with thorium dioxide were judged to be unacceptable for contributing to the sorption coefficient distribution (samples USW G1-2289 and USW G1-2233). For the remaining experiments, average values of sorption coefficients range from 1,213 to 23,800 mL/g for all rock types (SNL 2007a, A-71; also see Table 1.1.2-1, which lists raw K_d

values, not averages). Some of the data and effects that were taken into consideration are described in the following paragraphs.

Table 1.1.1.2.5 Thorium K_d Distribution Functions for Unsaturated Zone Rock Types

Species	Rock Type	Distribution	Coefficients Describing Distribution (mL/g)
Thorium	Zeolitic	Uniform	Range = 1,000 to 30,000
	Devitrified	Uniform	Range = 1,000 to 10,000
	Vitric	Uniform	Range = 1,000 to 10,000

Source: SNL 2007a, Table 6-1[a].

a. **Section A8.8.1 Devitrified Tuff**: For devitrified tuff, experiments were carried out with Yucca Mountain tuffs initially oversaturated with thorium dioxide; thorium sorption onto the rock sample in some cases, though not all, brought the final solution concentrations below saturation with thorium dioxide. Data are unavailable for the effect of experimental duration on sorption coefficient values for Yucca Mountain samples (SNL 2007a, Section A8.8.1). There are also no data available to evaluate the impact of variations in water chemistry on thorium sorption coefficients; however, water chemistry is expected to have little influence on thorium sorption coefficient values in Yucca Mountain groundwaters (SNL 2007a, Section A8.8.1). The range chosen is intended to reflect the range in surface areas found in devitrified tuffs in the unsaturated zone and the range in thorium concentrations expected during unsaturated zone transport. The lower end of the range reflects sorption coefficients at thorium concentrations near the solubility limit. Given the sparseness of available data, the probability distribution type selected is a uniform distribution, which equally weights K_d values within the selected range. Ultimately, professional judgment was the deciding factor in specifying the sorption coefficients for sorption of thorium on tuff, taking into account the available experimental data and comparisons with sorption behaviors of other radioelements such as americium.

b. **Section A8.8.2 Zeolitic Tuff**: Available data show that zeolitic tuffs have sorption coefficients for thorium that are similar to those obtained for devitrified tuffs. Based on the data presented in *Radionuclide Transport Models Under Ambient Conditions* (SNL 2007, Section A8.8.2), the range of thorium sorption coefficients selected for zeolitic tuffs in the unsaturated volcanic section at Yucca Mountain is 1,000 to 30,000 mL/g. The upper end of this range was selected to reflect the higher surface areas of zeolitic tuffs relative to devitrified tuffs. Given the sparseness of available data, a uniform distribution is selected for zeolitic tuffs.

c. **Section A8.8.3 Vitric Tuff**: Based on the available data presented in *Radionuclide Transport Models Under Ambient Conditions* (SNL 2007a, Section A8.8.3), vitric tuffs have sorption coefficients for thorium in the range of those obtained for the other tuffs in those experiments that were undersaturated with respect to thorium dioxide. The range of thorium sorption coefficients

selected for vitric tuffs in the unsaturated volcanic section at Yucca Mountain is 1,000 to 10,000 mL/g, with the upper limit supported in part by complimentary experiments conducted with silica (Table 1.1.2-1), which has surface properties similar to those of vitric tuff, see SNL 2007a (p. A-8). A uniform distribution is selected for vitric tuffs. A uniform distribution equally weights K_d values within the selected range. As with devitrified and zeolitic tuffs, professional judgment played a major role in deciding how experimental data were emphasized and how factors such as expected variations in water chemistry, radioelement concentrations, and variations in rock surface properties affect selection of the thorium K_d distribution for TSPA.

Updated Sorption Coefficients

Subsequent to completion of the SAR, errors in the classification of tuff rock-types used in thorium sorption coefficient measurements were identified. A rock-type correction for one sample changed it from devitrified to zeolitic, affecting the two highest "devitrified" thorium sorption coefficient measurements. As a result, the selected sorption coefficient distribution for devitrified tuff used in TSPA-LA shown at the beginning of this section is potentially non-conservative compared to the data, as it overestimates the thorium sorption coefficient for devitrified tuff by a factor of as much as 2.5, and therefore underestimates the potential mobility of thorium. (The impact to the zeolitic distribution is negligible).

In addition, an unrelated correction was made for vitric tuff. The original figure (Figure A-59d of SNL 2007a, p. A-74) was found to display one too many vitric tuff sorption coefficient values and has been corrected. While this correction did not markedly change the distribution of data for vitric tuff, it was noted that the selected distribution for vitric tuff appears to be even more non-conservative than the distribution selected for devitrified tuff. For vitric tuff, the maximum of the selected distribution is five times the maximum measured value.

Therefore, new thorium sorption coefficient distributions were developed for a TSPA impact analysis to determine whether the lower K_ds impact expected repository performance. These new distributions are referred to as "modified" sorption coefficient distributions for use in this impact analysis. The modified distributions are as follows:

Devitrified:	900 to 4,000 mL/g
Vitric:	300 to 2,000 mL/g
Zeolitic:	1,000 to 30,000 mL/g (no change).

The modified distributions are compared to experimental data and original selected distributions. The modified distribution is unchanged for zeolitic tuff because the original selected distribution remains representative. Based on these analyses, the impact of the modified thorium K_d distributions on the TSPA calculations is negligible. Therefore, the original distributions used in TSPA are adequate and are not revised.

1.1.1.2.6. Selenium

The ranges of selenium sorption coefficient values for the major rock types are derived directly from available experimental data. Matrix sorption coefficients have been developed for different rock types (zeolitic, devitrified, and vitric) and their statistical distribution are sampled to represent the uncertainty in sorption in the TSPA. The influence of expected variations in water chemistry, radioelement concentrations, and variations in rock surface properties within each of the major rock types were incorporated into the probability distributions (SNL 2007a, Section A1[a]).

Table 1.1.1.2.6 Selenium K_d Distribution Functions for Unsaturated Zone Rock Types

Species	Rock Type	Distribution	Coefficients Describing Distribution (mL/g)
Selenium	Zeolitic	Truncated Log-Normal	Range = 1 to 35 Mean = 14.3 Std Dev = 7.9
	Devitrified	Truncated Log-Normal	Range = 1 to 50 Mean = 14.0 Std Dev = 11.2
	Vitric	Truncated Log-Normal	Range = 0 to 25 Mean = 8.6 Std Dev = 7.9

Source: SNL 2007a, Table 6-1[a].

NOTE: Selenium sorption is set to zero in the TSw to account for nonlinear sorption behavior that could result from potentially high concentrations of aqueous selenium in this unit.

a. **Section A2.5.1[a] Devitrified Tuff**: Low-concentration sorption measurements are limited to selenium aqueous concentrations less than 10^{-8} molar. The truncated log-normal distribution was fit to the four low-concentration data points for use in the unsaturated zone below the TSw, where aqueous selenium concentrations are expected to remain below 10^{-8} molar (the K_d for selenium in the Tsw is set to zero; SAR Section 2.3.8.2.2.2 and SNL 2007a, Table 6-1[a], footnote "d").The truncated log-normal distribution has a mean of 14 mL/g, a standard deviation of 11.2 mL/g and a range of 1 to 50 mL/g, which provides an adequate fit to the experimental data.

b. **Section A2.5.2[a] Zeolitic Tuff**: Low-concentration sorption measurements are limited to selenium aqueous concentrations less than 10^{-8} molar. The truncated log-normal distribution was fit to the low-concentration data for use in the unsaturated zone below the TSw where aqueous selenium concentrations are expected to remain below 10^{-8} molar. The truncated log-normal distribution has a mean of 14.3 mL/g, a standard deviation of 7.9 mL/g and a range of 1 to 35 mL/g, which provides an adequate fit to the experimental data.

c. **Section A2.5.3[a] Vitric Tuff**: The only experimentally determined K_d values for selenium sorption onto vitric rock were determined from experiments for which aqueous selenium concentrations were greater than those used for selenium sorption experiments with devitrified and zeolitic tuffs (on the order of 0.1 ppm to 0.5 ppm or 10^{-6} to 5×10^{-6} molar (SNL 2007a, p. A-7). As shown in SNL 2007 (Section A2.5.1[a] and A2.5.2[a]) such elevated selenium concentrations result in significantly reduced empirical K_d values. The K_d distribution for selenium sorption onto vitric tuff in the unsaturated zone was therefore calculated by

comparing K_d values obtained from experiments conducted at higher selenium concentration and by accounting for the relationship between K_d values from the high-concentration and lower concentration experiments with zeolitic and devitrified tuffs. The standard deviation for the K_d distribution in zeolitic tuff is taken as the smaller of the values found for selenium sorption on zeolitic and devitrified tuff. The median selenium K_d for vitric rock is 8.6 mL/g, and the standard deviation 7.9 mL/g. The K_d distribution function is limited to a range of 0 to 25 mL/g. The mean for the sorption distribution on vitric tuff is the ratio of the medians for K_d values in zeolitic (0.5 mL/g) and devitrified rock (0.8 mL/g) from high-concentration data, which is a factor of 0.6. This calculation omits anomalously high sorption values found for sorption on zeolite. The mean K_d value for selenium sorption on zeolitic tuff (14.3) multiplied by 0.6 gives a value of 8.6 mL/g for the mean K_d value for selenium sorption on vitric tuff. A comparison of the truncated log-normal distribution with the high-concentration data shows the derived distribution gives values that are generally larger than Kd values derived for the high-concentration experiments. However, this distribution is reasonable for low concentration conditions given the variations between the high- and low-concentration measurements. Although the distribution developed for selenium sorption on vitric rock is not supported by direct measurements, the data at both low concentrations and at high concentrations indicates that selenium sorption is not strongly affected by rock type. The probability distribution for selenium sorption on vitric rock has lower K_d values compared to sorption on devitrified and zeolitic rock.

1.1.1.2.7 Tin

The ranges of tin sorption coefficient values for the major rock types are derived directly from the available experimental data. Matrix sorption coefficients have been developed for different rock types (zeolitic, devitrified, and vitric) and their statistical distribution are sampled to represent the uncertainty in sorption in the TSPA. The influence of expected variations in water chemistry, radioelement concentrations, and variations in rock surface properties within each of the major rock types were incorporated into the probability distributions (SNL 2007a, Section A1[a]).

Table 1.1.1.2.7 Tin K_d Distribution Functions for Unsaturated Zone Rock Types

Species	Rock Type	Distribution	Coefficients Describing Distribution (mL/g)
Tin	Zeolitic	Log-Uniform	Range = 100 to 5,000
	Devitrified	Log-Uniform	Range = 100 to 100,000
	Vitric	Log-Uniform	Range = 100 to 5,000

Source: SNL 2007a, Table 6-1[a].

a. **Section A2.6.1[a] Devitrified Tuff**: A log-uniform distribution was fit to the empirical sorption data for use in the unsaturated zone. This distribution has a range of 100 to 100,000 mL/g based on a fit to the experimentally determined K_d values. Data fall into two distinct ranges, less than 1,000 mL/g and greater than

10,000 mL/g. Experiments that fall into the lower range may have included colloids, which, if not adequately filtered, would increase the apparent tin concentration and result in lower apparent K_d values. Final solution concentrations in sorption experiments are quite low (3.5×10^{-14} to 4.4×10^{-12} M); it would not take much colloidal material with adsorbed tin, to significantly reduce the calculated K_ds. Four of the six experiments that fell into the higher range were conducted with UE-25 p#1 water. All of the tests with sorption in the lower range were conducted by using J-13 well water.

b. **Section A2.6.2[a] Zeolitic Tuff**: The sorption experiments were conducted on crushed tuff, and zeolitic tuff tends to create more colloid-sized material. If not completely removed, the colloidal material could carry sorbed tin as a suspended material, leading to reduced values of the apparent sorption. The sorption experiments carried out with UE-25 p#1 water show the tin sorption coefficient values at the high end of the range, which is consistent with the interpretation that colloidal interference has occurred. Therefore, the estimated log-uniform distribution was used to represent uncertainty in unsaturated zone sorption. This distribution has a range of 100 to 5,000 mL/g. The upper range was chosen because tin is expected to sorb as readily to zeolitic tuff as to vitric and devitrified tuffs. The value of 5,000 mL/g is the same as the upper bound for sorption of tin on vitric tuff and is less than the upper bound for tin sorption on devitrified tuff.

c. **Section A2.6.3[a] Vitric Tuff:** A log-uniform distribution was fit to the sorption data for use in the unsaturated zone. This distribution has a range of 100 to 5,000 mL/g based on the experimentally determined K_d values. These four data consist of two K_d values less than 200 mL/g and two K_d values greater than 3,000 mL/g. The two experiments that fall into the lower range may have included tin sorbed to colloids. Both of the higher sorption values were obtained by using UE-25 p#1 water, and both of the lower values were obtained by using J-13 well water.

1.1.2 Comparing TSPA K_d Distributions with Experimentally Determined K_d Values

A comparison between the developed K_d distribution functions and the experimentally determined K_d values from experiments on Yucca Mountain rocks is tabulated in Table 1.1.2-1 and shown graphically in Figure 1.1.2-1. The upper limit for K_d distributions selected for use in TSPA are, for nearly every element, lower than the experimental ranges, often by one or more orders of magnitude (e.g., plutonium, neptunium, cesium, strontium, radium). Exceptions include protactinium, for which very few experimental data are available (Section 1.1.1.2.1) and thorium, for which a TSPA impact analysis was conducted to examine the impact of using lower K_d values ("modified" thorium K_ds; Th[mod] in Figure 1.1.2-1). The results of that analysis showed no significant impact on TSPA dose calculations when using the lower thorium K_d values (Section 1.1.1.2.5). Kd ranges for tin sorption onto zeolitic and devitrified tuff also extend beyond experimentally determined maxima; however, this is a result of fitting a cumulative distribution to experimental data (without weighting) and calculating each K_d value that corresponds to a cumulative probability of one.

Table 1.1.2-1 TSPA K_d Distribution Ranges and Experimental K_d Ranges (values in mL/g)

Radioelement	Rock Type	TSPA K_d Range (mean/median)[a]	Experimental K_d Range (N)[b]
Uranium	Zeolitic	0 to 30 (0.5)	0 to 137 [9.423][c] (125)
	Devitrified	0 to 4 (0.2)	0 to 15 (65)
	Vitric	0 to 3 (0.2)	0 to 22 (86)
Plutonium[d]	Zeolitic	10 to 200 (100)	19 to 7,400 (181)
	Devitrified	10 to 200 (70)	4.7 to 5,165 (103)
	Vitric	10 to 200 (100)	68 to 3,584 (140)
Neptunium[e]	Zeolitic	0 to 6 (0.5)	0 to 511 (197)
	Devitrified	0 to 6 (0.5)	0.67 to 56 (180)
	Vitric	0 to 3 (1.0)	0.09 to 1,000 (153)
Americium[f]	Zeolitic	1,000 to 10,000 (5,500)	470 to 64,000 (37)
	Devitrified	1,000 to 10,000 (5,500)	1,000 to 14,000 (27)
	Vitric	100 to 1,000 (400)	13,000 to 1,000,000[k] (7)
Protactinium	Zeolitic	1,000 to 10,000 (5,500)	3.3 to 10.1 (11)
	Devitrified	1,000 to 10,000 (5,500)	NA
	Vitric	1,000 to 10,000 (5,500)	NA
Cesium	Zeolitic	425 to 20,000 (5,000)	2,700 to 72,000 (111)
	Devitrified	1 to 15 (8)	10 to 3,800 (208)
	Vitric	0 to 100 (2)	50 to 4,000 (30)
Strontium[g]	Zeolitic	50 to 2,000 (1,025)	1,500 to 350,000 (111)
	Devitrified	10 to 70 (40)	22 to 1,400 (213)
	Vitric	0 to 50 (25)	12 to 220 (34)
Radium/Barium[h]	Zeolitic	1,000 to 5,000 (3,000)	9,200 to 710,000 (110)
	Devitrified	100 to 1,000 (550)	130 to 25,000 (183)
	Vitric	50 to 600 (325)	65 to 4,740 [15,000][m] (31)
Thorium[i]	Zeolitic	1,000 to 30,000 (15,500)	2,000 to 26,700 (6)
	Devitrified	1,000 to 10,000 (5,500)	940 to 3,900 (6)
	Vitric	1,000 to 10,000 (5,500)	389 to 2,000 (4)
	Silica	NA	1 to 15,000 (14)

Table 1.1.2-1 TSPA K_d Distribution Ranges and Experimental K_d Ranges (values in mL/g) (Continued)

Radioelement	Rock Type	TSPA K_d Range (mean/median)		Experimental K_d Range (N)[a]	
Selenium[j]	Zeolitic	1 to 35	(14.3)	8.76 to 23.6	(4)
	Devitrified	1 to 50	(14.0)	1.51 to 51	(16)
	Vitric	0 to 25	(8.6)	NA	
Tin	Zeolitic	100 to 5,000	(707)	109 to 1,130	(16)
	Devitrified	100 to 100,000	(3162)	124 to 36,700	(11)
	Vitric	100 to 5,000	(707)	160 to 4,420	(4)

Sources: TSPA K_d values and ranges are from Table 6-1[a] of SNL 2007a; experimental K_d values are from DTNs cited in SNL 2007a

[a]). The mean and median values shown in this table are accurate, although for some uniform and log-uniform distributions, corresponding values indicated in bold font in Table 6-1[a] of SNL 2007 are *approximate* median values that were used in transport simulations for that report only. The TSPA *median* values are shown for all symmetric uniform and piece-wise uniform distributions, whereas *mean* values are shown for the truncated log-normal distributions of americium in zeolitic and devitrified tuffs [Am(Z) and Am(DV)], protactinium (all three rock types), and selenium (all three rock types).

[b]) N = number of reported observations (omitting negative values and K_d values not used to develop K_d distributions).

[c]) K_d in brackets (9,423 mL/g) anomalously exceeds the next highest experimentally determined K_d (137 mL/g).

[d]) Excluding K_d values for devitrified tuff from "old" dataee SNL 2007a). Although those data are shown in Figure A33b of SNL 2007a, p. A-44, they are not used to develop the K_d distribution function (SNL 2007a, p. A-40)

[e]) Excluding four K_d values from experiments with sample GU3-0433 and eight K_d values from experiments with sample G4-1608, due to suspected saturation (see text).

[f]) Excluding K_d values from samples JA-32 and YM-54 (devitrified) and GU3-1203, GU3-1301, and JA-18 (vitric) due to saturation effects (see text)

[g]) Excluding K_d values from 18 experiments with devitrified tuff sample G1-2840, four experiments with devitrified tuff sample YM-22, and two experiments with vitric tuff sample YM-38 due to saturation effects (see text)

[h]) Excluding two K_d values from experiments with sample YM-22 (devitrified tuff) due to suspected saturation (see text); no change in K_d range.

[i]) Excluding four K_d values from two zeolitic tuff samples USW G1-2289 and USW G1-2233 due to suspected saturation (see text).

[j]) Only K_d values from low-concentration experiments are indicated, as no K_d values from high-concentration experiments were used to develop K_d distribution functions for selenium. Selenium sorption is set to zero in the TSw to account for diminished sorption that may result from potentially high concentrations of aqueous selenium in this unit (see SNL 2007a, Table 6-1[a]).

[k]) Maximum K_d value of 1,000,000 is rounded up by 1 from two data entries. Corresponding data source lists both values as ">999,999."

[m]) K_d in brackets (15,000 mL/g) anomalously exceeds the next highest experimentally determined K_d (4,740 mL/g).

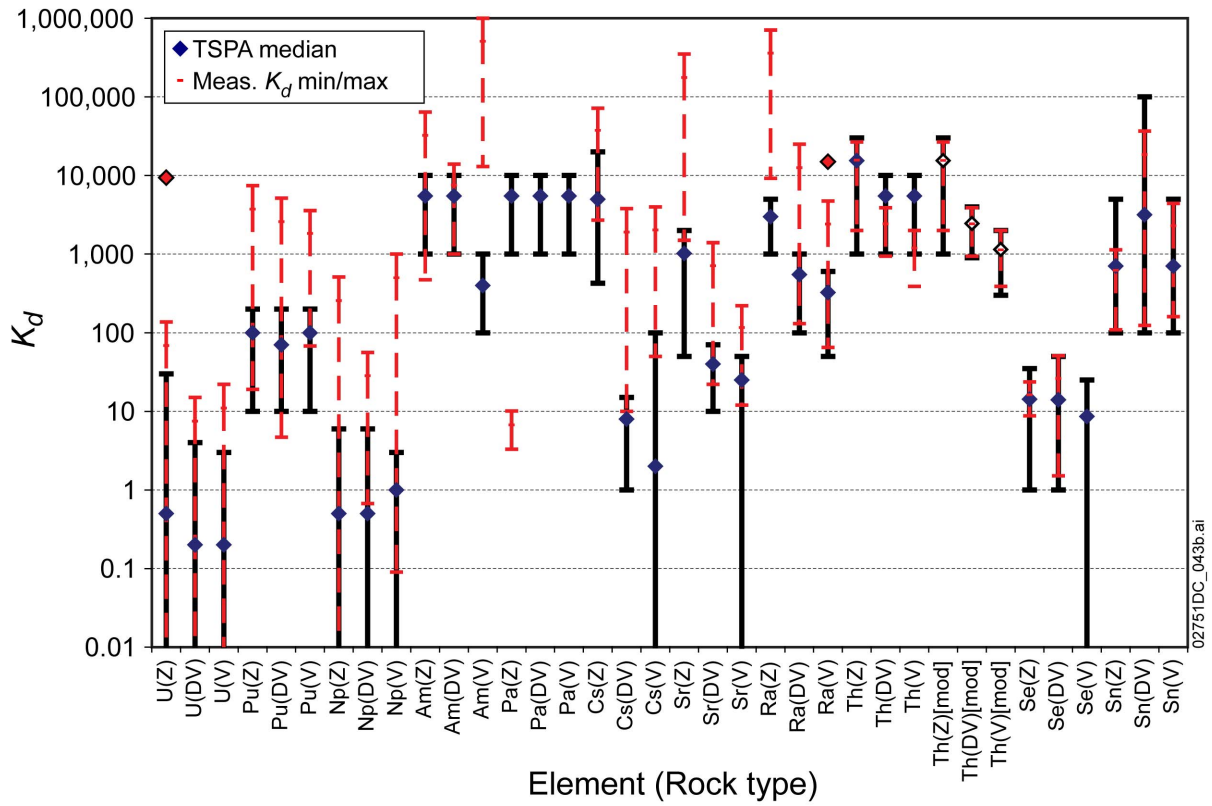

Source: K_d values and ranges from Table 1.1.2-1. Modified thorium ([mod]) ranges are not used in TSPA-LA. See Section 1.1.1.2.5.

NOTE: Rock type: (Z) = zeolitic tuff; (DV) = devitrified tuff; (V) = vitric tuff. The TSPA median values are shown for all symmetric uniform and piece-wise uniform distributions, whereas mean values are shown for the truncated log-normal distributions of americium in virtic and devitrified tuffs [Am(Z) and Am(DV)], protactinium (all three rock types), and selenium (all three rock types). Single data points above top-most K_d ranges of U(Z) and Ra(V) represent potential outliers (see Table 1.1.2-1 footnotes *c* and *m*).

Figure 1.1.2-1 TSPA K_d Values and Ranges from Table 6-1[a] of SNL 2007a (diamonds and black vertical bars) Compared Against Ranges of Measured Values (red dashed vertical bars).

2. COMMITMENTS TO NRC

None.

3. DESCRIPTION OF PROPOSED LA CHANGE

None.

4. REFERENCES

Allard, B.; Olofsson, U.; Torstenfelt, B.; and Kipatsi, H. 1983. Sorption Behaviour of Well-Defined Oxidation States. SKB TR-83-61. Stockholm, Sweden: Svensk Kärnbränsleförsörjning A.B.

Baes, C.F., Jr. and Mesmer, R.E. 1976. The Hydrolysis of Cations. New York, New York: John Wiley & Sons.

Berry, J.A.; Hobley, J.; Lane, S.A.; Littleboy, A.K.; Nash, M.J.; Oliver, P.; Smith-Briggs, J.L.; and Williams, S.J. 1989. "Solubility and Sorption of Protactinium in the Near-Field and Far-Field Environments of a Radioactive Waste Repository." Analyst, 114, 339-347. Cambridge, England: Royal Society of Chemistry.

Keller, C., 1966. The Chemistry of Protactinium. *Angewandte Chemie International Edition in English*, 5 (1), 23-35.

Kirby, H.W., 1959. *The Radiochemistry of Protactinium*. National Academy of Science, National Research Council, Nuclear Science Series, NAS-NS-3016, U.S. Atomic Energy Commission, Washington, D.C.

Kulmala, S., Hakanen, M., and Lindgerg, A. 1998. Sorption of protactinium on Finnish bedrock. *Radiokhimiya*, 40, 519–21.

Myasoedov, B.F., Kirby, H.W., and Tananaev, I.G., 2006. "Protactinium." In: *The Chemistry of the Actinide and Transactinide Elements*, Chapter 4, Volume I, edited by Morss, L.R.; Edelstein, N.M.; Fuger, J.; Katz, J.J., 3rd ed., Springer.

PHREEQC Software Code: V2.3. PC, LINUX , Windows 95/98/NT, Redhat 6.2. 10068-2.3-00.

SNL 2007a. *Radionuclide Transport Models Under Ambient Conditions*. MDL-NBS-HS-000008 REV 02 ADD 01. Las Vegas, Nevada: Sandia National Laboratories.
ACC: DOC.20050823.0003; DOC.20070718.0003; DOC.20070830.0005; LLR.20080324.0002; DOC.20090114.0005.

SNL 2007b. *Dissolved Concentration Limits of Elements with Radioactive Isotopes*. ANL-WIS-MD-000010 REV 06. Las Vegas, Nevada: Sandia National Laboratory.
ACC: DOC.20070918.0010.

Trubert, D., Le Naour, C., Jaussaud, C., and Mrad, O., 2003, Hydrolysis of Protactinium(V). III. Determination of Standard Thermodynamic Data. *Journal of Solution Chemistry*, 32, (6), 505-517.

Vine, E.N., Aguilar, R.D., Bayhurst, B.P., Daniels, W.R., Devilliers, S.J., Erdal, B.R., Lawrence, F.O., Maestas, S., Oliver, P.Q., Thompson, J.L., Wolfsberg K. 1980. *Sorption-Desorption Studies on Tuff. II. A Continuation of Studies with Samples from Jackass Flats, Nevada and Initial Studies with Samples from Yucca Mountain, Nevada*. Los Alamos Scientific Laboratory Informal Report LA-8110-MS, 1980 ACC: NNA.19920922.0023.

RAI Volume 3, Chapter 2.2.1.3.7, First Set, Number 4:

Describe the technical basis for establishing the low end of the sampled uncertainty distribution for the active fracture model gamma parameter at a value of 0.2 for the unsaturated zone transport abstraction.

Basis: For transport calculations, DOE addressed uncertainty in the gamma parameter by specifying a range of values from 0.2 to 0.6 (from a maximum possible variation between 0 and 1). DOE provided a technical basis for a nominal gamma value of 0.4 for most unsaturated zone model units between the repository horizon and the water table, based on (i) numerical simulations compared with C-14 data (SNL, 2008, PTMATP-AD02, Section 6.5.6), (ii) the calibration of gamma parameters for the site-scale flow model in TSPA (SAR, Tables 2.3.2-8 through 2.3.8-11), and (iii) the distribution of calcite coatings in unsaturated zone fractures (BSC, 2004, CMNA, Section 7.4.2). In sensitivity analyses presented by DOE (e.g., SAR Figure 2.3.2-40), radionuclide transport was significantly more sensitive to lower gamma values (e.g., values between 0.2 and 0.4) than higher values (e.g., 0.4 to 0.6). Given the demonstrated sensitivity, additional information is needed to justify the uncertainty distribution. The technical basis for the uncertainty distribution for the gamma parameter is needed to evaluate whether acceptance criteria related to system description and data uncertainty in (NRC, 2003, Section 2.2.1.3.7.3) are met, and thus verify compliance with 10 CFR 63.114(a) and 63.114(b).

1. RESPONSE

The selection of 0.2 as the lower end of the active fracture model (AFM) γ distribution for the total system performance assessment (TSPA) is based on comparisons of model calculations with three independent sets of field data. The results from these independent lines of evidence all support the choice of 0.2 as a reasonable lower limit for the active fracture γ parameter.

In Section 1.1, the definition of the active fracture γ parameter is presented, along with a discussion of the effects of the parameter value on flow and transport processes and the motivation for stochastic sampling of this parameter in TSPA. Evidence supporting the active fracture γ parameter lower limit of 0.2 follow in the next three sections: Section 1.2 presents results based on in-situ ^{14}C measurements in boreholes USW UZ-1 and USW SD-12 and associated modeling; Section 1.3 presents results based on Alcove 1 flow and transport testing and test-bed modeling; and Section 1.4 presents results based on calibration of the unsaturated zone flow model to in-situ water saturation and water potential measurements.

1.1 INTRODUCTION

The AFM is a component of the unsaturated zone flow and transport models used in the TSPA. The AFM is used to represent preferential flow within a fracture-network scale. The preferential flow arises because of a combination of the strong nonlinearity involved in an unsaturated flow system and heterogeneities of fracture geometry at different length scales (BSC 2004a, Section

6.3.7). The presence of preferential flow is captured in the AFM by limiting flow through a fracture network to only a portion of the total population of available connected fractures. This is quantified through a power-law equation that relates the fraction of active fractures, f_a, that participate in the flow as a function of the normalized fracture saturation, S_e (BSC 2004a, Equation 6-14):

$$f_a = S_e^{\gamma} \quad \text{(Eq. 1)}$$

where γ is the "active fracture parameter" and:

$$S_e = \frac{S_f - S_r}{1 - S_r} \quad \text{(Eq. 2)}$$

S_f (and the normalized value, S_e) represents an average saturation for all connected fractures in the fracture network, including the active and inactive fractures, and S_r is the residual fracture saturation. Based on Equation 1, an active fracture parameter of zero means that the fraction of active fractures is one for all fracture saturations. In other words, the fracture water is distributed over all available connected fractures, a condition that maximizes the fracture–matrix interface area available for exchange of water or dissolved solutes between the fracture and matrix. Conversely, if the active fracture parameter is one, the fraction of active fractures is equal to the normalized fracture saturation and all active fractures are fully saturated. This means that all of the available fracture water is confined to the minimum portion of the fracture network that can accommodate the given saturation level, a condition that minimizes the fracture–matrix interface area. Therefore fracture–matrix interaction increases with decreasing values of the active fracture parameter.

The appropriate values of the active fracture parameter used for the TSPA have been assigned through observations of flow and transport processes for the unsaturated zone at Yucca Mountain and comparisons of these observations with modeling results. As for many hydrogeologic and transport parameters, there is uncertainty associated with the assignment of specific values for the active fracture parameter. Sensitivity studies conducted using the unsaturated zone transport abstraction model found that transport results were sensitive to the value of the active fracture parameter (SNL 2008, Section 6.6.4). Higher values of the active fracture γ parameter lead to earlier breakthrough times, with greater sensitivity at lower values of the parameter (SNL 2008, Figures 6-33 to 6-35). To account for this sensitivity and uncertainty, a distribution for the active fracture parameter was sampled for TSPA stochastic simulations. The values were sampled using a uniform distribution ranging from 0.2 to 0.6 (SNL 2008, Section 6.5.6). The following information in this RAI response provides information concerning how the lower end of this range, 0.2, was selected.

1.2 ^{14}C OBSERVATIONS AND MODELING

Calculations of water travel times (ages) for the rock matrix were performed to compare with ^{14}C ages from gas samples taken from boreholes USW UZ-1 and USW SD-12 using models for

unsaturated zone flow and transport (BSC 2004a, Section 7.4.1). These model calculations were conducted using a range of the active fracture γ parameter from 0 to 0.6. Results indicated that values of the active fracture γ parameter, from 0 to 0.4 within the TSw, were needed for the model results to be consistent with observations of ^{14}C activity (BSC 2004a, Section 7.4.1).

1.3 ALCOVE 1 TEST OBSERVATIONS AND MODELING

Tests of unsaturated flow, drift seepage, and lithium bromide tracer transport were conducted at Alcove 1. The test bed is located near the North Portal of the Exploratory Studies Facility. Alcove 1 is an excavation about 30 m below the ground surface in fractured, densely welded tuff that is part of the Tiva Canyon Tuff (BSC 2004b, Section 6.12.5.1). Water and tracer introduced at the ground surface were collected in Alcove 1. The test data were used for comparisons with model calculations of drift seepage and tracer transport (Liu et al. 2003). Model calibrations using the drift seepage data included calibrations of the active fracture γ parameter (Liu et al. 2003, Section 3.3 and Table 1). Sequential calibrations to the seepage data resulted in values of 0.28 and 0.21 for the active fracture γ parameter (Liu et al. 2003, Table 1). These relatively low levels of the active fracture γ parameter, compared with the range of 0.2 to 0.6 used for unsaturated zone radionuclide transport in the TSPA, correspond to higher levels of fracture-matrix interaction. Despite this fact, the model results for tracer transport indicated that the model underestimated fracture–matrix interaction. The fracture–matrix interface area had to be increased by a factor of four to provide a reasonable match to the tracer transport measurements (Liu et al. 2003, Section 4.3).

1.4 UNSATURATED ZONE FLOW OBSERVATIONS AND MODELING

The site-scale unsaturated zone flow model was calibrated to site-specific data for matrix water saturation and water potential (SNL 2007a, Section 6.3.2). This calibration process included calibration of the active fracture parameter for the various model units represented in the flow model. Calibration results for the four uncertainty cases used in the TSPA are given in SAR Tables 2.3.2-21 to 2.3.2-24 and Tables B-1 to B-4 of *UZ Flow Models and Submodels* (SNL 2007b). The active fracture γ parameter values in the flow model calibration vary over a range of about 0.2 to 0.4 for the model units between the repository horizon (in tsw33 through tsw36 model units) and the water table. This is the portion of the unsaturated zone where radionuclide transport may occur. The unsaturated zone transport abstraction model used in the TSPA selects a single value of the active fracture γ parameter for all units between the repository and the water table in a given TSPA realization. Therefore, the uncertainty range for the active fracture γ parameter needs to include values representative of the range of values for units below the repository.

1.5 CONCLUSION

As noted in Section 1.1, higher values of the active fracture γ parameter lead to earlier breakthrough (lesser barrier performance) and lower values lead to extended breakthrough curves (greater barrier performance). Measurements of ^{14}C described in Section 1.2 indicate that the active fracture γ parameter could be as low as zero. In Section 1.3, the measurements from

Alcove 1 show that the calibrated value of 0.21 is an overestimate, requiring an adjustment of the fracture-matrix interface area. Therefore, the selection of 0.2 as the lower end of the distribution for unsaturated zone transport calculations used in the TSPA is reasonable, with some evidence that the value leads to a conservative bias towards earlier breakthrough.

2. COMMITMENTS TO NRC

None.

3. DESCRIPTION OF PROPOSED LA CHANGE

None.

4. REFERENCES

BSC (Bechtel SAIC Company) 2004a. *Conceptual Model and Numerical Approaches for Unsaturated Zone Flow and Transport.* MDL-NBS-HS-000005 REV 01. Las Vegas, Nevada: Bechtel SAIC Company. ACC: DOC.20040922.0006; DOC.20050307.0009.

BSC 2004b. *In Situ Field Testing of Processes.* ANL-NBS-HS-000005 REV 03. Las Vegas, Nevada: Bechtel SAIC Company. ACC: DOC.20041109.0001; DOC.20051010.0001; DOC.20060508.0001.

Liu, H-H.; Haukwa, C.B.; Ahlers, C.F.; Bodvarsson, G.S.; Flint, A.L.; and Guertal, W.B. 2003. "Modeling Flow and Transport in Unsaturated Fractured Rock: An Evaluation of the Continuum Approach." *Journal of Contaminant Hydrology, 62-63,* 173-188. New York, New York: Elsevier. TIC: 254205.

SNL (Sandia National Laboratories) 2007a. *Calibrated Unsaturated Zone Properties*, ANL-NBS-HS-000058 REV 00. Las Vegas, Nevada: Sandia National Laboratories. ACC: DOC.20070530.0013; DOC.20070713.0005; LLR.20080423.0015; LLR.20080527.0082.

SNL 2007b. *UZ Flow Models and Submodels.* MDL-NBS-HS-000006 REV 03 AD 01. Las Vegas, Nevada: Sandia National Laboratories. ACC: DOC.20080108.0003; DOC.20080114.0001; LLR.20080414.0007; LLR.20080414.0033; LLR.20080522.0086.

SNL 2008. *Particle Tracking Model and Abstraction of Transport Processes.* MDL-NBS-HS-000020 REV 02 AD 02. Las Vegas, Nevada: Sandia National Laboratories. ACC: DOC.20080129.0008; DOC.20070920.0003; LLR.20080325.0287; LLR.20080522.0170.

RAI Volume 3, Chapter 2.2.1.3.7, First Set, Number 5:

Describe the impact of vapor phase transport of carbon-14 on the comparison of the active-fracture model fitting simulation to the spatial distribution of carbon-14 in the unsaturated zone.

Basis: The applicant modeled groundwater ages, using different values of gamma in an active-fracture transport simulation in which carbon-14 is transported only in the liquid phase and compared the model results with groundwater ages estimated from carbon-14 measurements in unsaturated zone porewater and gas samples. Air permeability tests and barometric monitoring at Yucca Mountain suggest significant vapor flow and diurnal barometric pressure fluctuations throughout the unsaturated zone. The information is needed to verify compliance with 10 CFR 63.114(c) and (g).

1. RESPONSE

Based on rationale provided below, gas-phase transport of ^{14}C is significantly less than the aqueous-phase transport through the unsaturated zone. The gas-phase reservoir of ^{14}C is significantly smaller than the aqueous-phase reservoir. Barometric pumping cannot effectively transport ^{14}C because of the lack of net movement in this process. Buoyancy-induced gas-phase flow is expected to result in a net upward movement of ^{14}C, which is inconsistent with the observations. Measurements of ^{14}C activity in boreholes USW UZ-1 and USW SD-12 are considered to be the most representative of in-situ conditions at Yucca Mountain (*UZ Flow Models and Submodels*, SNL 2007a, Section 7.5.2). Diffusion cannot explain the observations of ^{14}C because penetration is too fast in the PTn and too slow in the TSw, whereas an aqueous-phase transport model provides a reasonable match to the data for borehole USW UZ-1. For all of these reasons, the distribution of ^{14}C in the unsaturated zone is dominated by transport in the aqueous phase. Therefore, the validation cases presented in *Conceptual and Numerical Approaches for UZ Flow and Transport* (BSC 2004a, Section 7.4.1) and *UZ Flow Models and Submodels* (SNL 2007a, Section 7.5), in which ^{14}C is transported in the aqueous phase but not in the gas phase, implement an appropriate approximation.

This response supports the use of radiocarbon analysis for validation of the unsaturated zone (UZ) flow model (SAR Section 2.3.2.5.1.2; SNL 2007a, Section 7.5) and the active fracture model (AFM) (SAR Section 2.3.2.4.1.1.3; BSC 2004a, Section 7.4.1). The analyses developed here provide additional details of the conceptual basis for the use of aqueous transport of ^{14}C in these validation cases. Accordingly, this response is fully consistent with the previous work although it uses new approaches for evaluating aqueous and gaseous transport. This response addresses only the distribution of natural ^{14}C. Dispersion of repository waste-derived gaseous ^{14}C in the geosphere is addressed by FEP 2.1.12.07.0A (Effects of radioactive gases in EBS; SAR Table 2.2-5), while aqueous transport of waste-derived ^{14}C to the accessible environment is included in the performance assessment (SAR Section 2.4.2.2.1.1.3).

Four modes of inorganic ^{14}C transport are evaluated in this response, to show that modeling of transport as only aqueous advection is an appropriate approximation, as was done for validation

of the UZ flow model (SAR Section 2.3.2.5.1.2) and the AFM (SAR Section 2.3.2.4.1.1.3). Evaluation of these four modes, and the results presented, are summarized as follows:

- Barometric pumping – This mechanism is evaluated relative to the potential for advective gas-phase transport of ^{14}C over depths relevant to the thickness of the unsaturated zone. The results indicate that the transport distances are limited to a few meters for a given barometric cycle and that the oscillatory nature of this mechanism does not result in significant net advective transport of ^{14}C. Therefore, any significant transport effects of barometric pumping are a result of dispersion associated with barometric pumping as discussed below.
- Gas-phase buoyant circulation – Large-scale buoyancy-driven flow in the unsaturated zone may occur due to seasonal variation of atmospheric temperature and pressure. The effect of this gas-flow process is evaluated in terms of its potential importance to the distribution of in situ ^{14}C. The results from this analysis show that such flow produces a net effect that is inconsistent with the profile of apparent ^{14}C age with depth, and therefore buoyant circulation is not an important mode of ^{14}C transport in the unsaturated zone.
- Gas-phase diffusive-dispersive transport – This evaluation considers the alternative hypothesis that diffusive gas-phase transport, potentially enhanced by the dispersive effect of fluctuating barometric pressure, controls the distribution of ^{14}C with depth in the unsaturated zone. The analysis results are compared with the ^{14}C apparent age profile from borehole UZ-1, to show that a diffusive mechanism does not fit the observations well and therefore diffusive-dispersive transport is not an important mode of ^{14}C transport in the unsaturated zone.
- Aqueous advective tranport – Mobile water in the unsaturated zone is known to contain dissolved inorganic carbon, and to percolate downward. This evaluation shows that 1-dimensional advective transport readily explains the distribution of ^{14}C in the unsaturated zone as represented by the profile from borehole UZ-1, while accounting explicitly for the contribution of mobile water in the UZ. Combined with the evaluation of other modes, this result shows that aqueous advection is the dominant mode of transport.

1.1 PARTITIONING OF ^{14}C BETWEEN THE GAS AND AQUEOUS PHASES

^{14}C, as for other carbon isotopes, is present in the unsaturated zone primarily as inorganic species that partition between the aqueous, gas, and mineral phases (SNL 2007a, Section 7.7.4.2). Aqueous carbon is predominantly bicarbonate in Yucca Mountain pore waters, while the predominant gas-phase species is carbon dioxide (SNL 2007b, p. 7-68). The principal mineral containing carbon is calcite (SNL 2007b, Table 6.2-2).

The soil zone is the source of most carbon found in the unsaturated zone and is responsible for the greater subsurface gas-phase CO_2 concentrations compared with atmospheric levels. Evapotranspiration in the soil zone leads to concentration of aqueous species in the soil zone and chemical saturation of the aqueous phase relative to calcite. Calcite precipitation is favored over

dissolution because of the saturated solution entering the unsaturated zone, the increasing temperature with depth, and the decreasing solubility of calcite with increasing temperature (SNL 2007a, Section 7.7.2). Analyses of secondary mineral deposition behavior show that calcite deposition has been relatively constant over millions of years. Furthermore, calcite dissolution and isotopic exchange of aqueous carbon with calcite do not appear to be significant factors in the distribution of ^{14}C in the unsaturated zone, based on ^{13}C observations. The continuous calcite precipitation in the unsaturated zone removes carbon from groundwater. Although ^{14}C exhibits some isotopic fractionation when calcite precipitates, calcite precipitation has an insignificant impact on the ^{14}C activity in the groundwater and subsurface gas.

Carbon-14 equilibrates rapidly between the gas and aqueous phases, based on the rapid equilibration of CO_2 between the gas and aqueous phases. Therefore, the ^{14}C age in the gas phase is representative of the local ^{14}C age in the aqueous phase. The gas phase reservoir holds much less carbon (including ^{14}C) than the aqueous phase reservoir. This is a result of the equilibrium partitioning relationship between gaseous and aqueous CO_2 and the relative volumetric fractions of gas and water in the rock. It is esimated that the aqueous reservoir contains 84 to 506 times more carbon than the gas phase, in a given volume of rock. Consequently, the local concentrations of inorganic carbon species, and the apparent ^{14}C age, are dominated by the aqueous phase.

1.2 SOLUTE TRANSPORT MODEL FOR COMPARISON WITH ^{14}C AGE

An aqueous-only solute transport model used to compare computed solute travel times with ^{14}C age is described in *UZ Flow Models and Submodels* (SNL 2007a, Section 7.5) and *Conceptual and Numerical Approaches for UZ Flow and Transport* (BSC 2004a, Section 7.4.1). Aqueous-phase transport in the unsaturated zone over distances relevant to observations of ^{14}C in boreholes USW UZ-1 and USW SD-12 is generally dominated by aqueous-phase advection; however, diffusion plays a role in the distribution of solutes between water in the fractures and rock matrix. In certain locations where aqueous advection is extremely small, global diffusion in the aqueous phase can become important. As shown in Figures 7.5-1 to 7.5-4 of *UZ Flow Models and Submodels* (SNL 2007a), aqueous-phase transport can explain the distribution of ^{14}C ages observed, but adjustments to the percolation flux are required.

1.3 GAS-PHASE ^{14}C TRANSPORT

In the following sections, several transport processes for ^{14}C are evaluated. Advective transport in the gas-phase is evaluated for both barometric pumping (Section 1.3.1) and buoyancy-induced flow (Section 1.3.2) mechanisms. Gas-phase diffusion/dispersion and aqueous-phase advection are compared in Section 1.3.3. These evaluations are used to determine whether or not significant effects from gas-phase transport are consistent with the data.

1.3.1 Barometric Pumping

Changes in weather can lead to changes in atmospheric (barometric) pressure at the ground surface. Because of the compressibility of air, an increase in barometric pressure will result in air moving into the unsaturated zone as a result of compression of the underground air.

Similarly, a reduction in barometric pressure will result in air exiting the unsaturated zone through the ground surface as a result of the expansion of the underground air. Barometric pumping was evaluated to assess the rate of removal of moisture from the unsaturated zone through evaporative processes. In the analysis, the amount of air entering or leaving the unsaturated zone (expressed in terms of volume per unit area, or length), V, is given by:

$$V = \phi S_g H\left(\frac{\Delta p}{p}\right) \quad \text{(Eq. 1)}$$

where H is the depth of the unsaturated zone, p, is the initial air pressure at the ground surface, and Δp is the change in air pressure at the ground surface, ϕ is the porosity, and S_g is the gas saturation. The average volumetric flux, q, is $\frac{V}{0.5T}$ because the full volume of air movement (into the rock or out) occurs in approximately one-half of a barometric cycle time period, T. More important for transport is the average pore velocity, v, which is $\frac{q}{\phi S_g}$. This is the average velocity of a constituent in the gas phase. The average distance traveled into the rock, d, is one-half the period times the pore velocity, so:

$$d = H\left(\frac{\Delta p}{p}\right) \quad \text{(Eq. 2)}$$

An analysis of atmospheric pressure data shows that the amplitude of pressure changes at the ground surface is represented by a value of 0.5 kPa, and the average pressure is 85 kPa. The pressure variations have a dominant period of 24 hours. The depth of the unsaturated zone is approximately 600 m. Therefore, the transport distance into the rock is about 3.5 m. Because pressure oscillates about an average value for barometric pumping, the motion of a constituent particle is also oscillatory.

For longer-period barometric cycles, the flux is reduced because the volume exchange occurs over a longer time period but the transport distance remains the same. The amount of compression or expansion of the unsaturated zone gas from barometric pumping is a linear function of depth that goes to zero at the water table, therefore, barometric pumping flux decreases with increasing depth. Because there is no net storage or release of air from the unsaturated zone over long time periods as a result of barometric pumping, the contribution to the net long-term advective transport of ^{14}C in the unsaturated zone is negligible; although the dispersive transport (represented as enhanced diffusion) associated with oscillatory gas flow may be important. The potential effects of barometric pumping on enhanced diffusion are discussed in Section 1.3.3.

1.3.2 Seasonal Buoyancy-Induced Flow in the Gas Phase

Seasonal buoyancy-induced gas-phase flow is possible because of the temperature stability of the underground gas, the seasonal temperature fluctuations at the ground surface, and the geometry of Yucca Mountain. A cross-sectional profile of Yucca Mountain is shown in Figure 1.3.2-1. Yucca ountain can be approximated as a ridge with the crest oriented north-south. As can be seen in the figure, the ground surface about 2,500 m east of the repository comes close to the elevation of the repository. During the winter, the cold air temperatures along the ground surface result in increased air density. The air is colder and denser along the ground surface than the air in the unsaturated zone, leading to a pressure difference that drives a flow of air laterally into the base of Yucca Mountain and back to the atmosphere at higher elevations near the crest. During the summer, the high air temperatures along the ground surface lead to the opposite effect, resulting in air entering Yucca Mountain at higher elevations and exiting at lower elevations (BSC 2004c, Setions 7.3 and 7.9.1.8).

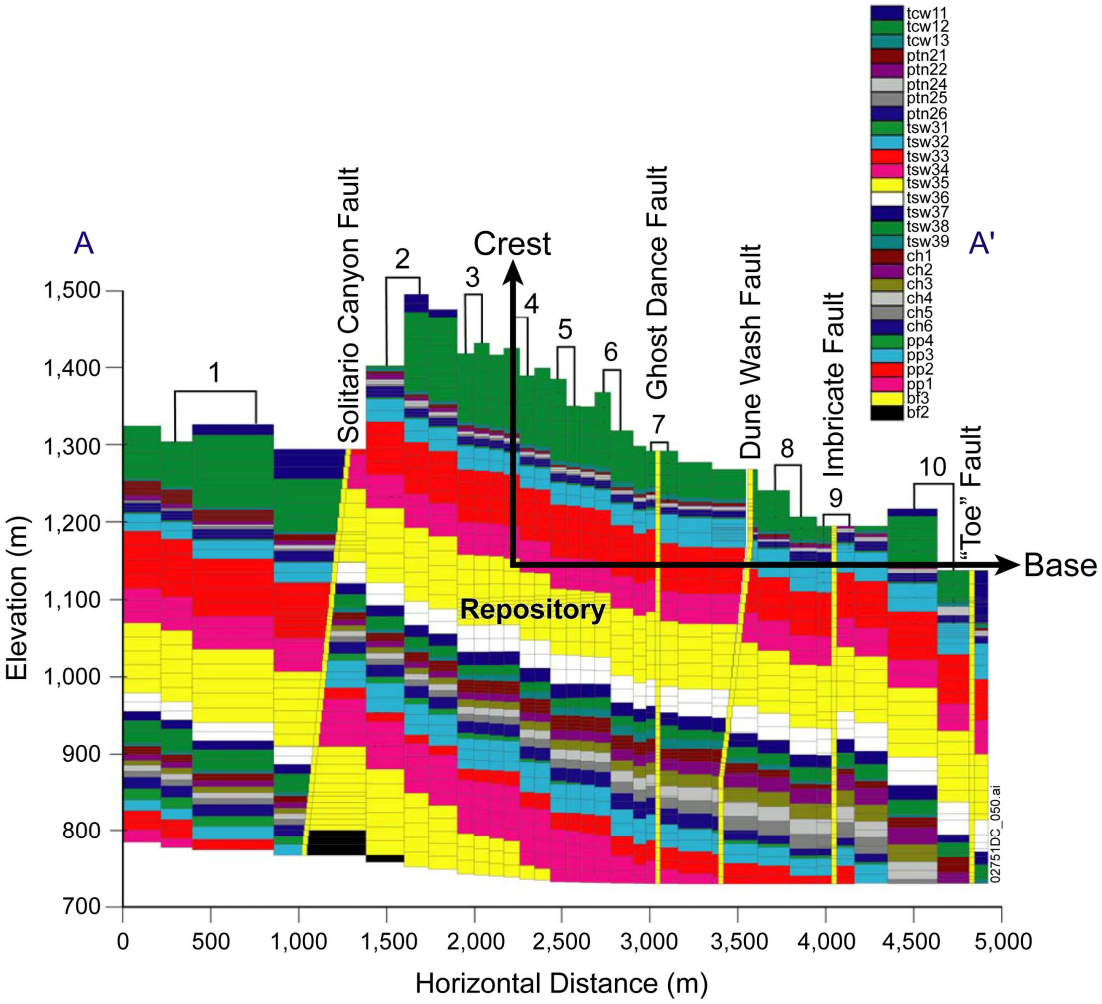

NOTE: Black arrows denote gas-flow pathways for one-dimensional model.

Figure 1.3.2-1. Vertical Cross-Section of Yucca Mountain (approximately east-west at 231,050 m Northing Nevada State Plane coordinates)

An analysis of gas-phase flow induced by buoyancy effects is developed here using two one-dimensional pathways to approximate the more complex flow patterns in three dimensions (black arrows in Figure 1.3.2-1). The two pathways are a horizontal pathway from the base of Yucca Mountain to the repository and a vertical pathway from the repository to the crest of Yucca Mountain. As discussed earlier, the flow pattern in winter is inward from the base, exiting at the crest. The summer flow pattern goes in the reverse direction.

1.3.2.1 Flow along the vertical pathway

Flow along the vertical pathway is computed using Darcy's law for the constant gas flux, V_i, where the subscript i is used to distinguish the month:

$$V_i = -\frac{k}{\mu}\left(\frac{dp_{vi}}{dz} - \rho_{vi} g\right) \qquad \text{(Eq. 3)}$$

where k is the permeability, μ is the viscosity, z is the depth (positive downward), ρ_{vi} is the gas density along the vertical pathway, g is the gravitational acceleration, and p_{vi} is the gas pressure along the vertical pathway. Strictly speaking, for compressible flow the volumetric flux, V_i, is not constant along a given pathway, but the mass flux, $\rho_{vi} V_i$, is constant for steady flow. A standard approximation used in atmospheric dynamics (Boussinesq approximation) allows for the neglect of density variations with respect to flow, except for where these variations couple with gravity to produce buoyancy forces, as in this problem. Therefore, V_i can be treated as a constant.

The standard equation of state for a perfect gas is:

$$\rho_{vi} = \frac{M_r p_{vi}}{R T_v} \qquad \text{(Eq. 4)}$$

where M_r is the apparent molecular weight of air, R is the gas constant per mole, and T_v is the absolute temperature along the vertical pathway. The temperature profile in the unsaturated zone will be approximated as a constant linear function of depth (SNL 2007a, Figures 6.3-2 through 6.3-6),

$$T_v = az + b \qquad \text{(Eq. 5)}$$

A shallow zone from the ground surface down to about 20-m depth that shows large seasonal fluctuations in temperature is not included in this analysis (SNL 2007a, Section 6.3.4). Temperature variations in this zone have a negligible effect because the zone is thin compared to distances from the ground surface to the repository, on the order of 300 m. Below 20-m depth, to the water table at roughly 600-m depth (Figure 1.3.2-1), the unsaturated zone temperatures do not have any seasonal dependence. Pressure at the ground surface $p_{si}(z)$ is described as a

function of distance below a datum at the crest of Yucca Mountain (taken here to be 1,400-m elevation). This is the same datum used for depth in the unsaturated zone, so the coordinate z used for the ground surface and subsurface depth are identical. Therefore, at a depth of zero ($z = 0$), the unsaturated zone pressure for the vertical pathway, $p_{vi}(0)$, is the same as the surface pressure (i.e., $p_{vi}(0) = p_{si}(0)$). The maximum depth of the vertical pathway (at the repository) is L_v.

Integration of Equation 3 using Equations 4 and 5, applying the boundary condition $p_{vi}(0) = p_{si}(0)$, gives the pressure at the repository depth ($z = L_v$):

$$p_{vi}(L_v) = \left(\frac{a}{b}L_v + 1\right)^{\frac{M_r g}{aR}} \left[p_{si}(0) - V_k \frac{(\mu/k)(b/a)}{1 - \frac{M_r g}{aR}} \left\{ \left(\frac{a}{b}L_v + 1\right)^{1-\frac{M_r g}{aR}} - 1 \right\} \right] \quad \text{(Eq. 6)}$$

This equation for the pressure is used to solve for V_i in Section 1.3.2.3.

1.3.2.2 Flow along the horizontal pathway

For horizontal flow, Darcy's law is:

$$V_i = -\frac{k}{\mu}\frac{dp_{hi}}{dx} \quad \text{(Eq. 7)}$$

where x is the horizontal coordinate with $x = 0$ at the repository and $x = L_h$ at the base of Yucca Mountain, and p_{hi} is the pressure along the horizontal pathway. Note that $p_{hi}(L_h) = p_{si}(L_v)$ because the horizontal pathway is at repository depth. Equation 7 is integrated to give:

$$p_{hi}(0) = p_{si}(L_v) + \frac{\mu V_i L_h}{k} \quad \text{(Eq. 8)}$$

The pressure $p_{si}(L_v)$ is related to the pressure $p_{si}(0)$ because the atmosphere is approximately in static equilibrium. For static equilibrium:

$$\frac{dp_{si}}{dz} = \rho_{si} g \quad \text{(Eq. 9)}$$

The equation of state for a perfect gas is also applicable here:

$$\rho_{si} = \frac{M_r p_{si}}{R T_{si}} \quad \text{(Eq. 10)}$$

As for the unsaturated zone, the temperature variation with depth is approximated by a linear profile:

$$T_{si} = cz + d_i \qquad \text{(Eq. 11)}$$

Unlike the unsaturated zone, the temperatures along the ground surface depend on the season. The constant c is known as the adiabatic lapse rate and is only a function of the gravitational constant and specific heat of air at constant pressure. Therefore, c is independent of the seasonal temperature variations. Integrating Equation 9, using Equations 10 and 11, and evaluating at repository depth ($z = L_v$) gives:

$$p_{si}(L_v) = p_{si}(0)\left(\frac{c}{d_i}L_v + 1\right)^{\frac{M_r g}{cR}} \qquad \text{(Eq. 12)}$$

Substituting this result into Equation 8 gives:

$$p_{hi}(0) = p_{si}(0)\left(\frac{c}{d_i}L_v + 1\right)^{\frac{M_r g}{cR}} + \frac{\mu V_i L_h}{k} \qquad \text{(Eq. 13)}$$

This equation for the pressure is used to solve for V_i in Section 1.3.2.3.

1.3.2.3 Gas flux

The pressures $p_{hi}(0)$ and $p_{vi}(L_v)$ are equal because these both correspond to the pressure at the repository. Therefore, Equations 6 and 13 are used to solve for V_i:

$$V_i = \frac{\frac{kp_{si}(0)}{\mu L_h}\left\{1 - \left(\frac{c}{d_i}L_v + 1\right)^{\frac{M_r g}{cR}}\left(\frac{a}{b}L_v + 1\right)^{-\frac{M_r g}{aR}}\right\}}{\frac{(b/aL_h)}{1 - \frac{M_r g}{aR}}\left\{\left(\frac{a}{b}L_v + 1\right)^{1-\frac{M_r g}{aR}} - 1\right\} + \left(\frac{a}{b}L_v + 1\right)^{-\frac{M_r g}{aR}}} \qquad \text{(Eq. 14)}$$

The temperature profile for the unsaturated zone is based on Figures 6.3-3 to 6.3-5 of *UZ Flow Models and Submodels* (SNL 2007a). The temperatures are approximately 17°C at an elevation of 1,300 m and 31°C at 730 m. This gives a value for the parameter a,

$a = 0.0246$°C/m.

The top unsaturated zone temperature at an elevation of 1,400 m is estimated by interpolating the yearly average temperatures from sites 2 and 3 given in Tables 6-2, 6-7, and 6-8 of *Yucca Mountain Site Description* (BSC 2004c). This results in the following value for b,

$$b = 16.0°\text{C}.$$

The lapse rate for surface temperatures is (SNL 2007a, Section 6.3.2),

$$c = 0.01°\text{C/m}.$$

The distances for the vertical and horizontal pathways are taken from Figure 1.3.2-1,

$$L_v = 300 \text{ m}$$

$$L_h = 2500 \text{ m}.$$

An approximate average bulk rock permeability for rock units above the repository is estimated using fracture permeabilities given in Appendix B of *UZ Flow Models and Submodels* (SNL 2007a),

$$k = 10^{-12} \text{ m}^2.$$

The other parameters are as follows:

$$\mu = 1.81 \times 10^{-5} \text{ kg/m-s at } 20°\text{C}$$

$$R = 8.3143 \text{ J/K-mol}$$

$$M_r = 29.864 \text{ g/mol}$$

$$g = 9.80664 \text{ m/s}^2.$$

The surface temperatures and pressures at 1400 m elevation are interpolated from values in Tables 6-2, 6-7, and 6-8 of *Yucca Mountain Site Description* (BSC 2004c) for Department of Energy meteorological monitoring sites 2 and 3. The monthly average temperatures and pressures at 1,400 m elevation are shown in Table 1-1. With these inputs and using Equation 13, the buoyancy-induced gas flux for each month is computed and shown in Table 1-1.

Table 1-1. Surface Temperatures and Pressures at 1,400 m Elevation (zero meters depth) and the Resulting Gas Fluxes

Month →	Jan	Feb	Mar	Apr	May	Jun	Jul	Aug	Sep	Oct	Nov	Dec
d_i (°C)	5.9	7.9	10.4	15.0	18.5	24.3	27.5	27.0	23.0	17.4	9.8	5.7
$p_{si}(0)$ (mbar)	860	859	858	857	856	857	859	860	860	860	861	860
V_i (mm/yr)	-94	-78	-58	-24	1	42	64	61	33	-7	-63	-96

The yearly average gas flux is about −18 mm/yr. The net negative gas flux is a result of geothermal energy that leads to the higher lapse rate in the unsaturated zone ($a = 0.0246$°C/m) as compared with the atmospheric lapse rate ($c = 0.01$°C/m). Therefore, it is reasonable to expect that the net transport direction is from the repository to the ground surface. If this gas flow process dominated ^{14}C movement, ^{14}C age would be expected to decrease with depth. The fact that ^{14}C observations at boreholes USW UZ-1 and USW SD-12 show a general trend of increasing ^{14}C age with depth (SNL 2007a, Figures 7.5-1 and 7.5-2) means that seasonal buoyancy-induced gas-phase flow is not a significant mechanism for transport of ^{14}C.

1.3.3 Gas-Phase Diffusion and Aqueous-Phase Advection of ^{14}C

Because ^{14}C decays and is not generated in the underground environment, there is a concentration gradient for ^{14}C between the ground surface and subsurface locations. Molecular diffusion is generally a weak mechanism for mass transport over large distances, such as the depth of the unsaturated zone. However, the effects of gas-phase flow, such as that imposed by barometric pumping, may result in dispersion that enhances diffusive transport.

An assessment of diffusive transport can be made using a one-dimensional, steady-state diffusive transport model. A one-dimensional, steady-state model including gas-aqueous exchange and simple radioactive decay gives a governing equation for diffusive transport,

$$\left(\frac{D_g}{1 + \Phi_w K_d / \Phi_g} \right) \frac{d^2 c_g}{dz^2} - \lambda c_g = 0 \qquad \text{(Eq. 15)}$$

where c_g is the concentration of ^{14}C in the gas phase, z is the depth, Φ_w is the water content of the rock, Φ_g is the gas content of the rock, K_d is the ratio of equilibrated ^{14}C concentrations in the aqueous phase to the gas phase, λ is the decay constant for ^{14}C, and D_g is the effective gas-phase diffusion coefficient in the rock. The effective diffusion is a combination of molecular diffusion and dispersion caused by gas movement discussed in Sections 1.3.1 and 1.3.2. Because of the difficulty in assigning a specific value of D_g, the parameter will be used to fit data from USW UZ-1 (SNL 2007a, Figures 7.5-1 and 7.5-3). The general solution of Equation 15 is:

$$c_g(z) = A \exp(Qz) + B \exp(-Qz) \qquad \text{(Eq. 16)}$$

where

$$Q = \left[\frac{\lambda}{D_g} \left(1 + \frac{\Phi_w K_d}{\Phi_g} \right) \right]^{\frac{1}{2}} \qquad \text{(Eq. 17)}$$

Boundary conditions are set at the ground surface and the water table. The ^{14}C concentration at the ground surface ($z = 0$) is approximately 100 pmc (percent modern carbon) and 15 pmc at the water table ($z =$ 600 m). The aqueous-gas partitioning factor, K_d, is estimated to be 40.

An important heterogeneity in the unsaturated zone system for diffusion processes in the gas phase is the volumetric gas content of the rock for in situ conditions. The uppermost hydrogeologic unit at UZ-1 is the PTn, which is underlain by the TSw hydrogeologic unit (SNL 2007a, Figure 7.5-1). All of the ^{14}C observations at UZ-1 are from these two hydrogeologic units (SNL 2007a, Figure 7.5-1). The gas content varies significantly between the PTn and the TSw hydrogeologic units. The gas content of the PTn is approximately 0.25 based on the approximate porosity (~0.5) and the gas saturation (~0.5) of the PTn (BSC 2004b, Table 6-6; SNL 2007c, Figure 6-1). By comparison, most of the TSw rock matrix has a gas content of about 0.01 because of the low porosity (~0.1) and low gas saturation (~0.1) (BSC 2004b, Table 6-6; SNL 2007c, Figure 6-1). The upper portion of the TSw has higher volumetric gas content in the rock matrix, some lithophysal cavities in the TSw may be in communication with the fracture porosity, and the gas content for fractures in the TSw is on the order of 0.01 (BSC 2004b, Table 6-5; SNL 2007c, Figure 6-1). Therefore, an effective value of gas content for the entire TSw is estimated to be about 0.03.

The volumetric water content of these hydrogeologic units also varies, but the variations are smaller. For the PTn, the water content is about equal to the gas content and in the TSw the water content is about 0.09 given a porosity of about 0.1 and a water saturation of about 0.9 (BSC 2004b, Table 6-6; SNL 2007c, Figure 6-1).

To account for the changes in gas and water content for the PTn and TSw, distinct forms of the general solution in Equation 16 are identified for the PTn and TSw:

$$c_{gP}(z) = A_P \exp(Q_P z) + B_P \exp(-Q_P z) \text{ in the PTn } (z = 0 \text{ to } 85 \text{ m}) \qquad \text{(Eq. 18)}$$

$$c_{gT}(z) = A_T \exp(Q_T z) + B_T \exp(-Q_T z) \text{ in the TSw } (z = 85 \text{ to } 600 \text{ m}) \qquad \text{(Eq. 19)}$$

where A_P, B_P, A_T, and B_T are coefficients determined by boundary and interface conditions discussed below. Consistent with the stratigraphy at borehole UZ-1, designate the PTn-TSw interface boundary position as $L_I = 85$ m and the water table as $L_{wt} = 600$ m. The concentration of ^{14}C at the ground surface is represented by C_s (expressed as a relative concentration; 100% modern carbon, or pmc), and the concentration at the water table is represented by C_{wt} (15 pmc). The boundary and interface conditions are:

^{14}C concentration boundary condition at the ground surface ($z = 0$ m):

$$A_P + B_P = C_s \qquad \text{(Eq. 20)}$$

^{14}C concentration boundary condition at the water table ($z = 600$ m):

$$A_T \exp(Q_T L_{wt}) + B_T \exp(-Q_T L_{wt}) = C_{wt} \quad \text{(Eq. 21)}$$

Continuity of ^{14}C concentration at the PTn-TSw interface ($z = 85$ m):

$$A_P \exp(Q_P L_I) + B_P \exp(-Q_P L_I) = A_T \exp(Q_T L_I) + B_T \exp(-Q_T L_I) \quad \text{(Eq. 22)}$$

Continuity of diffusive mass flux of ^{14}C at the PTn-TSw interface ($z = 85$ m):

$$\begin{aligned} &A_P Q_P \Phi_{gP} D_{gP} \exp(Q_P L_I) - B_P Q_P \Phi_{gP} D_{gP} e \exp(-Q_P L_I) \\ &= A_T Q_T \Phi_{gT} D_{gT} e \exp(Q_T L_I) - B_T Q_T \Phi_{gT} D_{gT} \exp(-Q_T L_I) \end{aligned} \quad \text{(Eq. 23)}$$

Equations 20 through 23 are solved for A_P, B_P, A_T, and B_T to give:

$$A_P = \left\{ \begin{array}{l} \dfrac{Q_T \Phi_{gT} D_{gT}}{Q_P \Phi_{gP} D_{gP}} \left(\dfrac{C_s \exp(-Q_P L_I) - C_{wt} \exp\{Q_T (L_{wt} - L_I)\}}{\exp(Q_p L_I) + \exp(-Q_P L_I)} \right) \bullet \\ \left(\dfrac{\exp(Q_T L_I) + \exp\{Q_T (2L_{wt} - L_I)\}}{\exp(Q_T L_I) - \exp\{Q_T (2L_{wt} - L_I)\}} \right) \\ + \dfrac{C_s \exp(-Q_P L_I) - \dfrac{Q_T \Phi_{gT} D_{gT}}{Q_P \Phi_{gP} D_{gP}} C_{wt} \exp\{Q_T (L_{wt} - L_I)\}}{\exp(Q_p L_I) + \exp(-Q_P L_I)} \end{array} \right\} \times$$

$$\left[1 - \left(\frac{Q_T \Phi_{gT} D_{gT}}{Q_P \Phi_{gP} D_{gP}} \right) \left(\frac{\exp(Q_P L_I) - \exp(-Q_P L_I)}{\exp(Q_p L_I) + \exp(-Q_P L_I)} \right) \left(\frac{\exp(Q_T L_I) + \exp\{Q_T (2L_{wt} - L_I)\}}{\exp(Q_T L_I) - \exp\{Q_T (2L_{wt} - L_I)\}} \right) \right]^{-1} \quad \text{(Eq. 24)}$$

$$B_P = C_s - A_P \quad \text{(Eq. 25)}$$

$$A_T = \frac{A_P \exp(Q_P L_I) + (C_s - A_P) \exp(-Q_P L_I) - C_{wt} \exp\{Q_T (L_{wt} - L_I)\}}{\exp(Q_T L_I) - \exp\{Q_T (2L_{wt} - L_I)\}} \quad \text{(Eq. 26)}$$

$$B_T = C_{wt} \exp(Q_T L_{wt}) - A_T \exp(2Q_T L_{wt}) \quad \text{(Eq. 27)}$$

With the coefficients from Equations 24 through 27 and the solutions for the PTn and TSw given by Equations 18 and 19, the concentrations may be computed.

A similar analysis may be carried out assuming that ^{14}C is transported entirely by advection in the aqueous phase. The equivalent one-dimensional, steady-state model including gas-aqueous exchange and simple radioactive decay is:

$$q_w \frac{dc_w}{dz} + \lambda\left(\theta_w + \frac{\theta_g}{K_d}\right)c_w = 0 \qquad \text{(Eq. 28)}$$

where c_w is the aqueous-phase ^{14}C concentration, q_w is the aqueous-phase percolation flux and all other terms as defined previously. The general solution is:

$$c_{wP}(z) = A_P \exp\left(\left[-\frac{\lambda}{q_w}\left(\theta_{wP} + \frac{\theta_{gP}}{K_d}\right)\right]z\right) \qquad \text{(Eq. 29)}$$

$$c_{wT}(z) = A_T \exp\left(\left[-\frac{\lambda}{q_w}\left(\theta_{wT} + \frac{\theta_{gT}}{K_d}\right)\right]z\right) \qquad \text{(Eq. 30)}$$

where A_P and A_T are coefficients determined by boundary and interface conditions discussed below and subscripts P and T designate the PTn and TSw units as before.

The ^{14}C concentration boundary condition at the ground surface requires:

$$A_P = C_s \qquad \text{(Eq. 31)}$$

The continuity of ^{14}C concentration at the PTn-TSw interface requires that:

$$A_T = A_P \frac{\exp\left(-\frac{\lambda}{q_w}\left(\theta_{wP} + \frac{\theta_{gP}}{K_d}\right)L_I\right)}{\exp\left(-\frac{\lambda}{q_w}\left(\theta_{wT} + \frac{\theta_{gT}}{K_d}\right)L_I\right)} \qquad \text{(Eq. 32)}$$

The ^{14}C concentrations may be computed using the solutions for the PTn and TSw given by Equations 29 and 30 and the coefficients given by Equations 31 and 32.

The diffusion coefficient is adjusted to a value of 9.9×10^{-6} m^2/s to provide a best fit of the ^{14}C concentration data (Figure 1.3.3-1). Similarly, the aqueous flux is adjusted to provide a best fit of the ^{14}C concentration data; this value is 5.1 mm/yr for the advective fit in the same figure. All other relevant parameters are assigned the same values as for the diffusion model. The model results are shown in Figure 1.3.3-1 along with the measurements from borehole USW UZ-1.

The data and model results have been converted to ^{14}C age, a, to be consistent with the presentation in *UZ Flow Models and Submodels* (SNL 2007a, Figures 7.5-1 to 7.5-4) using the age equation,

$$a = \frac{T_{0.5}}{\ln(2)} \ln\left(\frac{c_{g0}}{c_g}\right) \quad \text{(Eq. 33)}$$

where $T_{0.5}$ is the half-life (5,715 years) and c_{g0} is the ^{14}C concentration at the ground surface. Although the surface values of ^{14}C concentration slightly exceed 100 pmc, data evaluated for borehole USW UZ-1 (SNL 2007a, Figures 7.5-1 and 7.5-3) shown in Figure 1.3.3-1 below start at a depth where ^{14}C concentrations are less than 100 pmc and the ages are evaluated relative to a ground surface concentration of 100 pmc.

The results shown in Figure 1.3.3-1 indicate that the aqueous advection model provides a better match to the data. In the diffusive model the ^{14}C penetrates the PTn too rapidly and the TSw too slowly because of the differences in volumetric gas content of the two units. The aqueous advection model reflects the basic pattern in the data (i.e., the rate of change in ^{14}C apparent age with depth is greater in the PTn than in the TSw) (see Figure 1.3.3-1b).

This analysis neglects any differences in the effective diffusion parameter, D_g, between the PTn and TSw. However, the differences in these units are expected to result in higher values of D_g for the PTn than the TSw. The greater porosity of the PTn is expected to result in larger values of tortuosity, because tortuosity has been approximated by porosity of the rock matrix (SNL 2007d, Section 6.1.2.4). Also the dispersive effects of barometric pumping are larger near the surface than deeper in the unsaturated zone (see Section 1.3.1), leading to greater dispersive effects in the PTn as compared with the TSw. The effects of these changes on the diffusion coefficient lead to even greater difficulty matching a gas-diffusion-only model to the data. Therefore, gas-phase diffusion is not a dominant process for large-scale ^{14}C transport in the unsaturated zone.

Additional comparisons of ^{14}C age with the unsaturated zone flow model have also been made using data from borehole USW SD-12 (SNL 2007a, Figures 7.5-2 and 7.5-4). The models developed here for borehole USW UZ-1 are not directly applicable to USW SD-12 because the ^{14}C measurements at this borehole were taken in three major units (TCw, PTn, and TSw) instead of just two as at USW UZ-1. If the diffusion and advection models derived here were extended to account for the additional unit, the models could then be applied to the USW SD-12 data. However, the ^{14}C transport behavior at this borehole is not expected to readily distinguish between gas-phase diffusion and aqueous-phase advection transport processes. This is because of the similarity of the volumetric gas content in the TCw and TSw units, and because the PTn is thinner at this location. In other words, the stratigraphy at USW SD-12 is expected to behave more like a homogeneous system than at USW UZ-1.

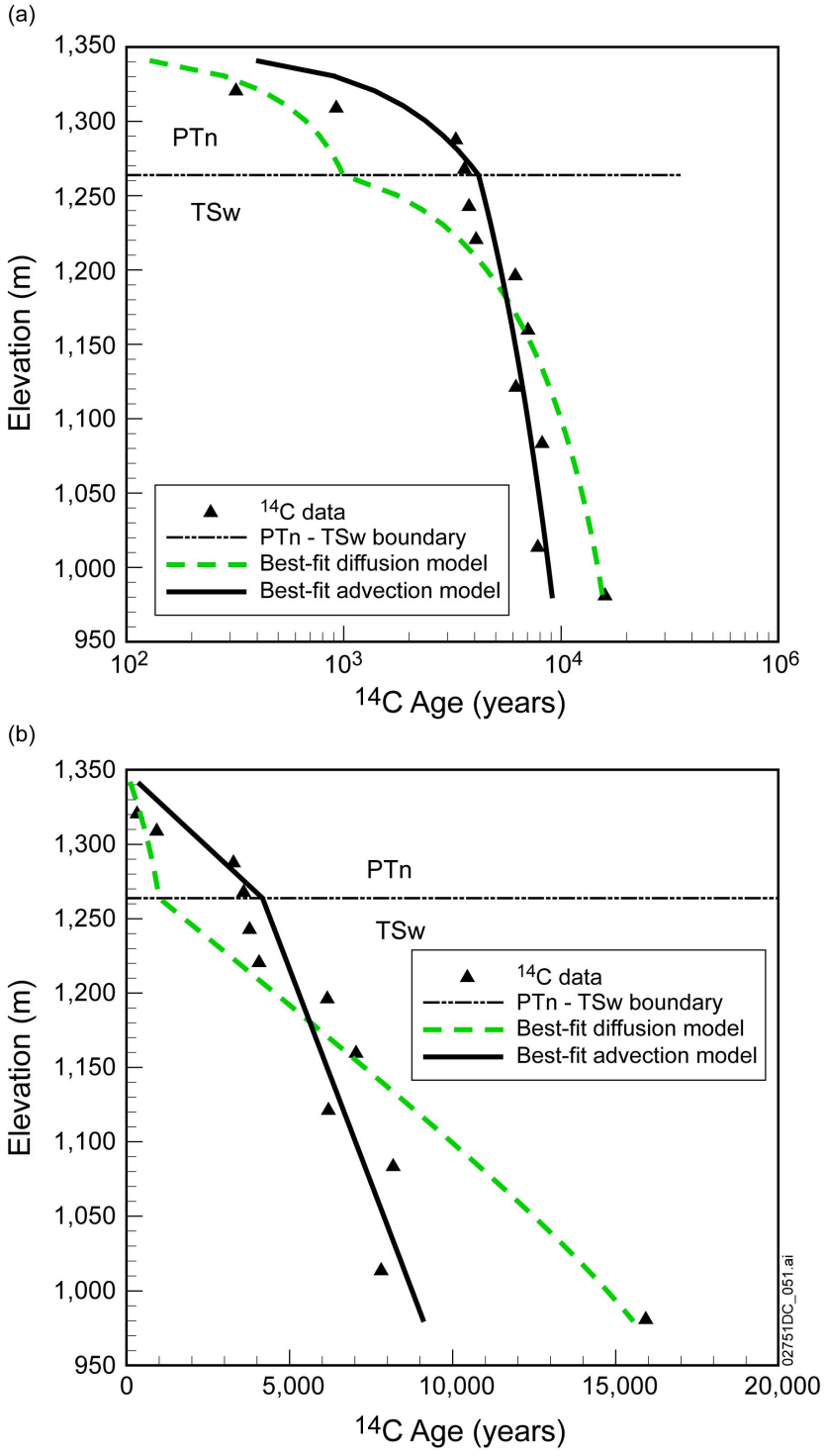

NOTE: (a) logarithmic time scale, (b) linear time scale.

Figure 1.3.3-1. Gas-Phase Diffusion and Aqueous Advection Models for ^{14}C at Borehole USW UZ-1 with Measured ^{14}C Ages

1.4 SUMMARY—IMPACTS OF THE GAS-PHASE ON THE DISTRIBUTION OF ^{14}C IN THE UNSATURATED ZONE

Based on the considerations above, the contribution from gas-phase transport of ^{14}C to the distribution of ^{14}C in the unsaturated zone is significantly less than from aqueous-phase transport. The distribution of ^{14}C in the unsaturated zone is dominanted by transport in the aqueous phase. Therefore, the validation cases presented in *Conceptual and Numerical Approaches for UZ Flow and Transport* (BSC 2004a, Section 7.4.1) and *UZ Flow Models and Submodels* (SNL 2007a, Section 7.5), in which ^{14}C is transported in the aqueous phase but not in the gas phase, implement an appropriate approximation.

2. COMMITMENTS TO THE NRC

None

3. DESCRIPTION OF PROPOSED LA CHANGE

None

4. REFERENCES

BSC (Bechtel SAIC Company) 2004a. *Conceptual Model and Numerical Approaches for Unsaturated Zone Flow and Transport.* MDL-NBS-HS-000005 REV 01. Las Vegas, Nevada: Bechtel SAIC Company. ACC: DOC.20040922.0006; DOC.20050307.0009.

BSC 2004b. *Analysis of Hydrologic Properties Data.* ANL-NBS-HS-000042 REV 00. Las Vegas, Nevada: Bechtel SAIC Company. ACC: DOC.20041005.0004; DOC.20050815.0003; LLR.20080416.0162; LLR.20080522.0162.

BSC 2004c. *Yucca Mountain Site Description.* TDR-CRW-GS-000001 REV 02 ICN 01. Two volumes. Las Vegas, Nevada: Bechtel SAIC Company. ACC: DOC.20040504.0008; LLR.20080423.0019.

SNL (Sandia National Laboratories) 2007a. *UZ Flow Models and Submodels.* MDL-NBS-HS-000006 REV 03 AD 01. Las Vegas, Nevada: Sandia National Laboratories. ACC: DOC.20080108.0003; DOC.20080114.0001; LLR.20080414.0007; LLR.20080414.0033; LLR.20080522.0086.

SNL 2007b. *Drift-Scale THC Seepage Model.* MDL-NBS-HS-000001 REV 05. Las Vegas, Nevada: Sandia National Laboratories. ACC: DOC.20071010.0004; LLR.20080408.0266.

SNL 2007c. *Calibrated Unsaturated Zone Properties.* ANL-NBS-HS-000058 REV 00. Las Vegas, Nevada: Sandia National Laboratories. ACC: DOC.20070530.0013; DOC.20070713.0005; LLR.20080423.0015; LLR.20080527.0082.

SNL 2007d. *Radionuclide Transport Models Under Ambient Conditions.* MDL-NBS-HS-000008 REV 02 ADD 01. Las Vegas, Nevada: Sandia National Laboratories. ACC: DOC.20050823.0003; DOC.20070718.0003; DOC.20070830.0005; LLR.20080324.0002.

SNL 2008. *Simulation of Net Infiltration for Present-Day and Potential Future Climates.* MDL-NBS-HS-000023 REV 01 AD 01. Las Vegas, Nevada: Sandia National Laboratories. ACC: DOC.20080201.0002; LLR.20080507.0008; LLR.20080522.0101.

RAI Volume 3, Chapter 2.2.1.3.7, First Set, Number 6:

Discuss the potential for bias in the prediction of active fractures and matrix diffusion resulting from the exclusion of Cl-36 evidence.

Basis: Fracture coating record of secondary minerals used to support the active-fracture model could be analogous to a time-exposure of all flow paths over the last 10 million years, whereas a "snapshot" of present-day flow paths might correspond to a much smaller subset of active fractures. Although evidence for the existence of a few fast present-day flow paths, as suggested by bomb-pulse chlorine-36 measurements, is sparse, such data may provide an illustration of an active-fracture "snapshot". The NRC staff notes that Liu, et al. (1998) discounts chlorine-36 data as evidence for sparsely distributed active flow paths in support of the active-fracture model. The authors suggest that bomb-pulse Cl-36 occurrences are too widespread to help constrain the active-fracture model as a continuum model. The information is needed to verify compliance with 10 CFR 63.114(c) and (g).

1. RESPONSE

This response clarifies that secondary mineral data are representative of the flow pattern in the unsaturated zone of Yucca Mountain under the current climate, and that bomb-pulse ^{36}Cl signals are associated with flow paths carrying a small amount of water only and are not representative of a significant number of flow paths. Consequently, the potential for bias in the prediction of active fractures and the matrix diffusion (associated with active fractures) without explicitly considering bomb-pulse ^{36}Cl data is negligible.

1.1 Secondary Mineral Data and Flow Pattern in the Unsaturated Zone

The secondary minerals were deposited from water percolation through the unsaturated zone of Yucca Mountain, and provide a record of water flow history through fractures at depth in the unsaturated zone. The growth histories of these mineral coatings also provide an indication of how the Yucca Mountain unsaturated zone has responded to changes in climate conditions. Geochronological data indicate that growth rates are extremely slow and have remained approximately uniform over long periods of time. The average long-term growth rates calculated for Yucca Mountain deposits within the repository horizon have also remained relatively constant from early- through late-stage parts of the coatings. The U-series data from outermost calcite and silica imply similarly slow growth rates evenly distributed throughout the last 500 k.y., in spite of the known variations in Pleistocene climate in the region. These growth rates are consistent with rates derived by assuming that the cumulative thicknesses of 10 to 20 mm (0.4 to 0.8 in.) of mineral coatings were formed at constant rates over the past 10 to 12.8 million years. This observation, plus the fact that most coatings continued to grow through the Pleistocene, indicate that once established, transmissive fracture pathways appear to be maintained throughout the history of the mountain. These interpretations of slow, uniform growth rates at the same depositional sites over long periods indicate that the unsaturated zone fracture network is capable of maintaining a large degree of hydrologic stability. Hydrologic

stability of the Yucca Mountain unsaturated zone is also implied by the fact that the approximately uniform long-term growth rates have been maintained throughout the Miocene, Pliocene, and Pleistocene epochs (BSC 2004a, Section 7.7.7). Because of this stability inferred from mineral growth rates, secondary minerals are representative of flow patterns under the current climate (BSC 2004b, Section 7.4.2).

The evaluation of the active fracture model (AFM) with the secondary mineral data is not only based on secondary minerals that are representative of the flow pattern under the current climate, but also that the unsaturated zone flow pattern (the number of active fractures) is largely stable under the current and past climates (BSC 2004b, Section 7.4.2). Specifically, two infiltration rates at borehole USW SD-12, the present-day mean infiltration rate and glacial-transition maximum infiltration rate, were used in the simulations for evaluating the AFM with the mineral data (BSC 2004b, Section 7.4.2). Simulation results indicate that the calculated fraction of active fractures within the whole fracture continuum is about 10% for an AFM parameter (γ) of 0.4. This is consistent with the observation that about 10% of fractures have fracture coatings (secondary minerals) among fractures surveyed along Exploratory Studies Facility (ESF). The simulation results also indicate that the numbers of active fractures are relatively stable for $\gamma = 0.4$ and for the infiltration ranges considered. Therefore, AFM simulation results are remarkably consistent with the fracture coating data set and its implications (BSC 2004b, Section 7.4.2).

1.2 Fast Flow Paths Associated With Bomb-Pulse ^{36}Cl Carry a Minor Amount of Water

This RAI also asks whether bomb-pulse ^{36}Cl data may provide an illustration of an active-fracture "snapshot" under current climate. As discussed in SAR Section 2.3.2.2.2.3, a journal report by Liu et al. (1998), and *Conceptual Model and Numerical Approaches for Unsaturated Zone Flow and Transport* (BSC 2004b, Section 6.1.7), fast and potentially transient flow paths associated with bomb-pulse ^{36}Cl carry only about 1% of percolating water in the unsaturated zone, because: (1) bomb-pulse signatures were found in only a few locations in the ESF that are generally associated with localized fault structures that cut through the Paintbrush nonwelded (PTn) hydrogeologic unit; (2) these discrete flow paths are not associated with large catchment areas involving large volumes of infiltrating water; and (3) bomb-pulse tracers (e.g., ^{36}Cl and ^{14}C) are not detected in perched water that would be considered more representative of overall flow in the unsaturated zone (at least the northern portion of the unsaturated zone). Instances where bomb-pulse ^{36}Cl samples were not associated directly with PTn-cutting faults were found to be associated with structural features in the Topopah Spring welded (TSw) hydrogeologic unit that could transport water laterally away from PTn-cutting faults. Field measurements support the distribution of flow paths that are relatively uniform and not limited to major faults (BSC 2004b, Section 6.1.7; SAR Section 2.3.2.2.2.3). Measured matrix saturations suggest relatively uniform values for most of the units, and in situ water potential measurements show little variability within the TSw for different boreholes (BSC 2004b, Section 6.1.7; SAR Section 2.3.2.2.2.3). It was also observed that temperatures within the TSw unit are fairly uniform, providing further confirmation that flow fields are relatively uniform in the unsaturated zone (SAR Section 2.3.2.2.2.3; BSC 2004b, Section 6.1.7).

In conclusion, bomb-pulse ^{36}Cl signals are not representative of a significant number of all flow paths (in the unsaturated zone of Yucca Mountain) that the AFM represents. Indications of bomb-pulse ^{36}Cl in the ESF are sparse and not broadly representative of flow in the unsaturated zone. Similarly, the bomb-pulse ^{36}Cl signals are not broadly representative of transport pathways and processes such as matrix diffusion. Therefore the bomb-pulse ^{36}Cl would have a negligible effect on constraining matrix diffusion. Accordingly, bomb-pulse ^{36}Cl signals do not provide an illustration of an active fracture "snapshot."

2. COMMITMENTS TO NRC

None.

3. DESCRIPTION OF PROPOSED LA CHANGE

None.

4. REFERENCES

BSC (Bechtel SAIC Company) 2004a. *Yucca Mountain Site Description.* TDR-CRW-GS-000001 REV 02 ICN 01. Two volumes. Las Vegas, Nevada: Bechtel SAIC Company. ACC: DOC.20040504.0008; LLR.20080423.0019.

BSC 2004b. *Conceptual Model and Numerical Approaches for Unsaturated Zone Flow and Transport.* MDL-NBS-HS-000005 REV 01. Las Vegas, Nevada: Bechtel SAIC Company. ACC: DOC.20040922.0006; DOC.20050307.0009.

Liu, H.H.; Doughty, C.; and Bodvarsson, G.S. 1998. "An Active Fracture Model for Unsaturated Flow and Transport in Fractured Rocks." *Water Resources Research, 34,* (10), 2633-2646. Washington, D.C.: American Geophysical Union. TIC: 243012.

RAI Volume 3, Chapter 2.2.1.3.7, First Set, Number 7:

Address the potential limitations of the relationship between the fraction of active fractures and the effective saturation of connected fractures on modeling flow in unsaturated fractured rock and resulting effects on uncertainty and its propagation.

Basis: Liu, et al. (1998) describe how f_a, S_e, and gamma range only between 0 and 1. With these constraints, in f_a-S_e space, only f_a-S_e pairs including and above the $f_a = S_e$ line are possible. This limitation has not been explained. In the situation, where all the fracture system is saturated ($S_e = 1$), the active fracture model would have all the fractures flowing. The relationship seems to preclude the possibility of preferential pathways. However, fracture geometries can result in preferential pathways even in fully-saturated fracture systems. DOE should address the ramifications of this limitation on matrix diffusion. The information is needed to verify compliance with 10 CFR 63.114(c) and (g).

1. RESPONSE

This response clarifies the physical bases for relationships among active fracture model (AFM) parameters and further demonstrates that the current approach to simulating matrix diffusion (based on the AFM) does not overestimate matrix diffusion.

1.1 Relationships Among AFM Parameters

The AFM was developed to deal with preferential flow in an unsaturated fracture network (Liu et al. 1998). It conceptualizes the fracture continuum (consisting of connected fractures) into two parts: active and inactive. Liquid water flow occurs in the active part only and the inactive part is simply by-passed. The fraction of active fractures within the whole fracture continuum, f_a, is related to the effective fracture saturation (defined for the whole fracture continuum), S_e, by (Liu et al. 1998, Equation 1):

$$f_a = S_e^{\gamma} \qquad \text{(Eq. 1)}$$

where the parameter, γ, is a constant. Based on the definitions of f_a and S_e, the effective saturation in active fractures, S_{ae}, is given as (Liu et al. 1998, Equation 3):

$$S_{ae} = \frac{S_e}{f_a} \qquad \text{(Eq. 2)}$$

Physically speaking, water saturation in active fractures, S_{ae}, cannot be larger than one, and therefore the following relationship must hold:

$$f_a \geq S_e \qquad \text{(Eq. 3)}$$

Combining Equations 1 and 2 yields:

$$S_{ae} = S_e^{1-\gamma} \quad \text{(Eq. 4)}$$

which physically requires that the parameter γ cannot be larger than one. Otherwise, S_{ae} would take nonphysical values larger than one.

Also note that Equation 1 requires that parameter γ must be positive. Otherwise, f_a would be larger than one, which is nonphysical. The physical basis for Equation 1 was documented in *Conceptual Model and Numerical Approaches for Unsaturated Zone Flow and Transport* (BSC 2004, Section 7.2) and is a result of a fractal flow pattern often observed in unsaturated and multiphase flow systems (BSC 2004, Section 7.2.1). The theoretical relationship between the parameter γ and the dimension of a fractal flow pattern was also established by *Conceptual Model and Numerical Approaches for Unsaturated Zone Flow and Transport* (BSC 2004, Section 7.2.3).

In summary, there are no self-imposed limitations on the treatment of AFM parameters, and the constraints on the parameter values are a result of fundamental physics.

1.2 AFM and Matrix Diffusion

The RAI indicates that the AFM seems to preclude the possibility of preferential pathways for saturated flow (when all the fractures are active), while fracture geometries can result in preferential pathways even in fully saturated fracture systems. In other words, the RAI is concerned with whether non-uniform flow among the different active fractures is considered by the AFM.

The AFM was mainly developed for dealing with preferential flow in unsaturated flow conditions, based on a consideration that flow occurs only in active fractures and inactive fractures are simply by-passed. However, it does not conceptually preclude the possibility of non-uniform flow within the active-fracture continuum consisting of active fractures. The use of van Genuchten relationships for describing water flow within the active-fracture continuum does consider the non-uniform flow behavior within the active fracture continuum (Liu et al. 1998), because van Genuchten parameter *m* characterizes effects of so-called "pore-size distributions" that is a measure of heterogeneous flow behavior below the continuum scale. Note that the volume of perched water zones is only a small percentage of the unsaturated zone of Yucca Mountain. Thus although the fraction of active fractures, f_a, is always 1 in perched zones because of saturated conditions, transport through perched water zones is associated with the fastest travel times from the repository to the water table (SNL 2008, Sections 6.6.2.1 and 6.6.2.3). Therefore the neglect of preferential pathways for flow and transport in perched zones does not have a significant nonconservative effect on the overall model for flow and transport behavior in the unsaturated zone.

Note that the current approach (based on the AFM) to modeling solute transport in the unsaturated zone of Yucca Mountain underestimates the effects of matrix diffusion, which is

conservative for performance evaluation because matrix diffusion can retard radionuclide transport (BSC 2006). Analysis of Alcove 8/Niche 3 tests that were performed in the unsaturated zone of Yucca Mountain indicates that simulation results significantly overestimated peak concentrations and underestimated breakthrough times for all the tracers (BSC 2006, Section 6.3.2), implying that matrix diffusion was underestimated. One major reason for this underestimation is that small-scale fractures have been ignored for modeling flow and transport in the unsaturated zone of Yucca Mountain and these small-scale fractures considerably increase the degree of matrix diffusion by increasing fracture-matrix interfacial area (BSC 2006, Section 6.4). Although some uncertainty exists in the analysis of Alcove 8/Niche 3 tests, the underestimation of matrix diffusion inferred from the analysis is generally consistent with study results in the literature (BSC 2006, Section 6.4.1). Therefore, AFM does not preclude preferential pathways, and based on a comparison of model and field results, the conservative parameterization used for matrix diffusion bounds the uncertainties.

2. COMMITMENTS TO NRC

None.

3. DESCRIPTION OF PROPOSED LA CHANGE

None.

4. REFERENCES

BSC (Bechtel SAIC Company) 2004. *Conceptual Model and Numerical Approaches for Unsaturated Zone Flow and Transport.* MDL-NBS-HS-000005 REV 01. Las Vegas, Nevada: Bechtel SAIC Company. ACC: DOC.20040922.0006; DOC.20050307.0009.

BSC 2006. *Analysis of Alcove 8/Niche 3 Flow and Transport Tests.* ANL-NBS-HS-000056 REV 00. Las Vegas, Nevada: Bechtel SAIC Company. ACC: DOC.20060901.0003; DOC.20061208.0016.

Liu, H.H.; Doughty, C.; and Bodvarsson, G.S. 1998. "An Active Fracture Model for Unsaturated Flow and Transport in Fractured Rocks." *Water Resources Research, 34,* (10), 2633-2646. Washington, D.C.: American Geophysical Union. TIC: 243012.

SNL (Sandia National Laboratories) 2008. *Particle Tracking Model and Abstraction of Transport Processes.* MDL-NBS-HS-000020 REV 02 AD 02. Las Vegas, Nevada: Sandia National Laboratories. ACC: DOC.20080129.0008; DOC.20070920.0003; LLR.20080325.0287; LLR.20080522.0170.

RAI Volume 3, Chapter 2.2.1.3.7, First Set, Number 8:

Describe how the data and observations from the Alcove 1 test support the flow and transport models used in the TSPA.

Basis: Figures 2.3.8-34 and -35, referred to in Section 2.3.8.4.4.5 of the SAR, show applied bromide tracer concentrations that fluctuated irregularly from 150 to 600 ppm over a period of approximately 100 days and observed seepage tracer concentrations that increased from 0 to 150 ppm in a relatively smoother curve approximately one month after the initiation of the tracer application. It is not apparent how much retardation of the tracer occurred relative to the infiltration rate, why the applied tracer concentration varied so irregularly as part of the experiment, how the fluctuating initial concentration was addressed in the interpretation of results and subsequent modeling, or what percentage of tracer mass was recovered relative to that applied. This information is needed to verify compliance with 10 CFR Part 63.114(g).

1. RESPONSE

In general, the Alcove 1 test data and test-bed modeling were used in the license application to provide additional confidence in the continuum method for modeling flow and transport in fractured rock. The observed seepage rates in Alcove 1 were predicted using a continuum modeling method to represent fractured rock. The results of the test and test-bed modeling regarding drift seepage support conceptual models of unsaturated flow, and confirm that numerical approaches used in unsaturated zone models adequately represent physical processes controlling unsaturated flow (SAR Section 2.3.2.3.2.6). Modeling was also conducted to interpret results of the tracer transport test. The tracer test provided information supporting the use of the active fracture model and the method used to model matrix diffusion. The results of the test and test-bed modeling provided evidence of the significance of matrix diffusion for tracer transport in fractured, densely welded tuff. The test results and test-bed modeling also provided evidence that the effects of hydrodynamic dispersion in fractures are not significant (SAR Section 2.3.8.3.3.3). Although the Alcove 1 test data are useful for supporting conceptual models for unsaturated zone flow and transport in fractured rock, the test results were not used directly to provide feeds of parameter values to the TSPA for the license application.

1.1 ALCOVE 1 TEST DESCRIPTION

The Alcove 1 test was conducted over about a twenty-two-month period that commenced in March 1998. The test bed is located near the North Portal of the Exploratory Studies Facility. Alcove 1 is an excavation about 30 m below the ground surface in fractured, densely welded tuff that is part of the Tiva Canyon Tuff (BSC 2004a, Section 6.12.5.1). Although the rock is characterized by high fracture permeability and low rock matrix permeability (SNL 2007a, Appendix B), the water content of the rock is dominated by water in the rock matrix (SNL 2007b, Figure 6-1; BSC 2004b, Tables 6-5 and 6-6). A rectangular infiltration plot having an area of 83.7 m^2 was used to introduce water into the ground. At the latter stage of the test, water was introduced containing a lithium bromide tracer (BSC 2004a, Section 6.12.5.1 and

Figure 6-167). Water release rates were much higher than the expected infiltration rates under natural conditions in order to produce results within a reasonable time period (SAR Section 2.3.8.3.3.3). Water and tracer recovery were conducted in the underlying alcove, with a collection system covering an area of 40.2 m^2 and lies within the footprint of the infiltration plot (BSC 2004a, Section 6.12.5.1). Untraced water was released intermittently during the first 14 months of the test. Measurements made from this portion of the test were used to calibrate the test-bed flow model. During this period seepage of water into Alcove 1 was observed and measured. Traced water was subsequently applied over two distinct periods. Seepage water volume and tracer concentrations in Alcove 1 were observed and measured during and after the tracer application periods. Very little tracer reached Alcove 1 from the first application that lasted about 6 weeks. Tracer was again introduced into the infiltrating water approximately 4 months after ending the first tracer application. This second application of tracer continued for approximately 15 weeks. The tracer concentrations measured in Alcove 1 during and after the second tracer application were much larger than those associated with the first tracer application (Figure 1.1). After the second tracer application, untraced water continued to be applied for another 12 weeks in order to drive the introduced tracer to Alcove 1. Tracer and seepage measurements also continued during this period.

1.2 TRACER TRANSPORT RATES

1.2.1 Observed Transport Time

Tracer transport rates in Alcove 1 are based on tracer breakthrough behavior shown in Figure 1.1. The time origin on this plot corresponds to May 18, 1999, about 14 months after the beginning of water release into the infiltration plot at Alcove 1. This analysis focuses on the second tracer application because of the stronger response in the tracer concentrations measured in Alcove 1 seepage water as compared with the first tracer application. The second tracer injection began on day 152 on Figure 1.1. Tracer injection concentrations are highly variable during the second tracer application (see Section 1.4), but an average injection concentration was about 266 ppm. The tracer response reached a peak concentration in Alcove 1 seepage water of about 133 ppm at about day 255. After this peak concentration is reached, the tracer concentration in Alcove 1 seepage water began to decrease in response to the termination of tracer in the infiltrating water at the ground surface.

One characteristic transport time is the median transport time, which is the time required for the downstream tracer concentration to reach 50% of a sustained tracer concentration in the introduced water at the ground surface. The breakthrough curve reaches the 50% relative concentration level about 103 days after the beginning of the second tracer application to the infiltration water (Figure 1.1). Another characteristic transport time is the point where the slope of the concentration-time curve changes significantly at about 180 days, or 28 days after the beginning of tracer application. This time will be referred to as the “breakthrough” time. The fraction of tracer that arrives at or before the breakthrough time is clearly quite small and, therefore, is suitable to characterize the fastest observed tracer transport.

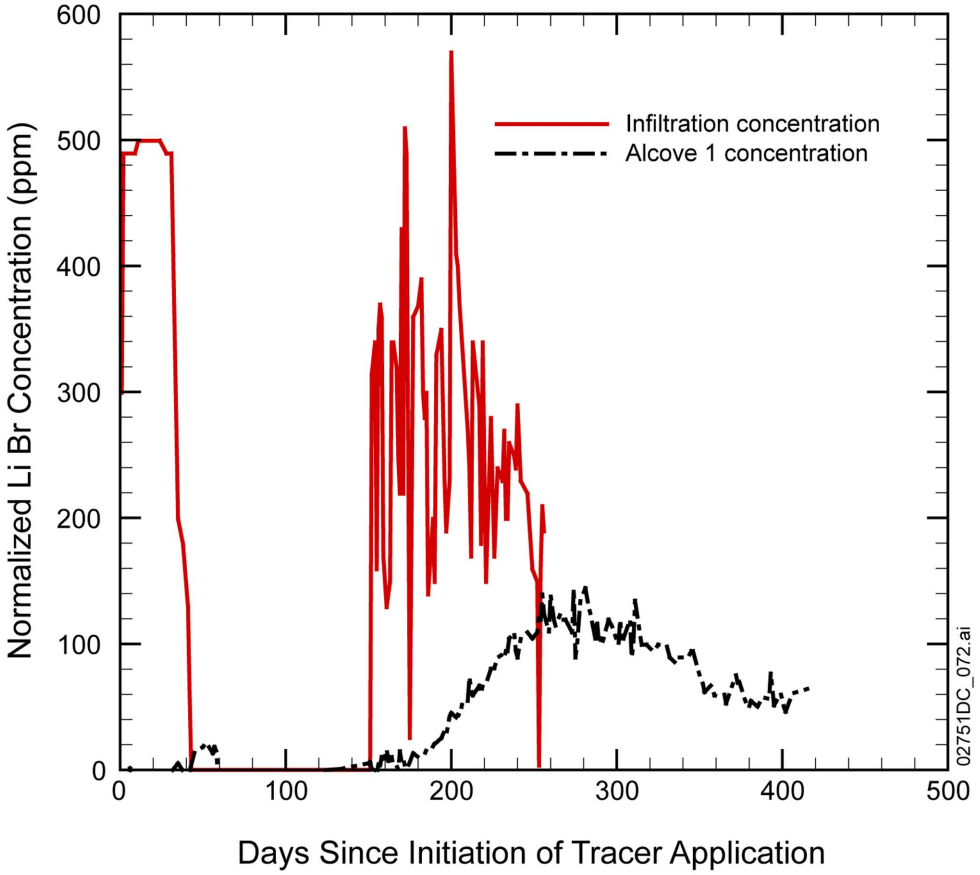

NOTE: Tracer initiated on May 18, 1999 (day 1 of figure); applied tracer ends January 28, 2000 (day 256 of figure); collection of tracer concentrations in Alcove 1 seepage water ends on July 5, 2000 (day 415 of figure). Tracer concentrations normalized to a background concentration of 21 ppm.

Figure 1.1. Tracer Concentrations in Applied Infiltrating Water and Seepage Water in Alcove 1

1.2.2 Estimated Minimum Transport Time

A characteristic minimum transport time may be estimated by assuming that water flow and tracer transport occurs entirely in the fractures without any interaction with the rock matrix. This is the expected water transport time because the prewetting of the test bed prior to initiating tracer transport results in negligible matrix imbibition and means that most of the introduced water is limited to flow through fractures. Flow and transport confined to the fractures forces the water and tracer to move through the minimum area available for flow and transport processes, and therefore results in the shortest transport time. This is characteristic of a "fast" transport process for the Alcove 1 system, but cannot be expected to estimate the absolute minimum transport time because of spatial heterogeneity of fracture pathways and spatial and temporal variations in the infiltration rate will also affect the absolute minimum transport time.

To calculate the characteristic minimum transport time, the average percolation flux, q, and fracture water content, θ_f are needed. The fracture water content is equal to the fracture

porosity, ϕ_f, times the fracture water saturation, S_f. The equation for the estimated minimum transport time is given by:

$$T_{\min} = \frac{L\theta_f}{q} \quad \text{(Eq. 1)}$$

Where L is the distance from the ground surface to Alcove 1 (30 m) (BSC 2004a, Section 6.12.5.1). The average percolation flux may be estimated using the measured infiltration rates. The time period corresponding to the second tracer application is day 587 to the last data reported on about day 775 after initiating water release. Over this period, an approximate average infiltration rate is about 1.9 cm/day.

The water saturation for fracture-only flow can be estimated by treating the process as gravity-driven, unit gradient flow. In this case, the effective hydraulic conductivity of the fractures to water equals the average percolation flux (SNL 2007a, Equation A-3 and p. A-2). The effective hydraulic conductivity, K_{fe}, is related to the vertical fracture permeability, k_f, and relative permeability, k_{rf} by *UZ Flow Models and Submodels* (SNL 2007a, p. A-2):

$$K_{fe} = \frac{\rho g k_f k_{rf}}{\mu} \quad \text{(Eq. 2)}$$

where g is gravitational acceleration (9.81 m/s^2), ρ is the density of water, and μ is the dynamic viscosity of water. The density and dynamic viscosity of water at 20°C are 1,000 kg/m^3 and 1×10^{-3} kg/m-s, respectively.

The fracture relative permeability is given in *UZ Flow Models and Submodels* (SNL 2007a, Equation A-11):

$$k_{rf} = S_{ef}^{(1+\gamma)/2}\left[1-\left\{1-S_{ef}^{(1-\gamma)/m_f}\right\}^{m_f}\right]^2 \quad \text{(Eq. 3)}$$

where γ is the active fracture parameter, m_f is the van Genuchten pore-size distribution parameter, and S_{ef} is the normalized fracture water saturation given in *UZ Flow Models and Submodels* (SNL 2007a, Equation A-8):

$$S_{ef} = \frac{S_f - S_{rf}}{1 - S_{rf}} \quad \text{(Eq. 4)}$$

where S_{rf} is the residual water saturation of the fractures.

Hydrogeologic parameters were estimated for Alcove 1 through calibration to seepage observations. Two calibrations were conducted and the second calibration is used here because it

is based on the most seepage data. The calibrated parameters for Alcove 1 are shown in Table 1-1.

Table 1-1. Fracture Properties for Alcove 1

k_f (m^2)	m_f	γ	ϕ_f	S_{rf}
3.08×10^{-11}	0.633	0.21	0.03	0.01

The fracture water saturation may be computed by setting the effective hydraulic conductivity in Equation 2 to the average percolation flux of 1.9 cm/day. This is done using Equations 3 and 4, along with the specified parameter values. Doing this, the fracture water saturation is found to be 0.129. With this value of fracture water saturation and the fracture porosity, the fracture water content is found to be 0.0041. Using Equation 1, the estimated minimum transport time is about 6.5 days. Note that the minimum transport time is comparable with the observed water travel time estimated as the time difference for the first peak in the infiltration-rate and first peak in the seepage rate 560 days after initiating water release.

1.2.3 Estimated Maximum Transport Time

A characteristic maximum transport time may be estimated by assuming that water flow and tracer transport fully equilibrates between the fractures and rock matrix. This forces the water and tracer to move through the maximum area available for flow and transport processes, and therefore results in the longest transport time. This is characteristic of a "slow" transport process for the Alcove 1 system, but cannot be expected to estimate the absolute maximum transport time because of spatial heterogeneity of fracture pathways and spatial and temporal variations in the infiltration rate will also affect the absolute maximum transport time. Furthermore, the absolute maximum transport time will be associated with tracer transport that is confined solely to the rock matrix. However, this maximum transport time cannot be representative of all tracer pathways because the low-permeability rock matrix cannot transmit the entire percolation flux that occurred during the test. Therefore, only a small fraction of introduced tracer could potentially travel entirely through rock matrix from the surface to Alcove 1.

To calculate the characteristic maximum transport time, the average percolation flux, q, and fracture water content, θ_f, and matrix water content, θ_m are needed. The fracture water content is defined in Section 1.2.2 and the matrix water content is equal to the matrix porosity, ϕ_m, times the matrix water saturation, S_m. The equation for the estimated maximum transport time is given by:

$$T_{\max} = \frac{L\left(\theta_f + \theta_m\right)}{q} \qquad \text{(Eq. 5)}$$

where L is the distance from the ground surface to Alcove 1 (30 m) (BSC 2004a, Section 6.12.5.1). As discussed in Section 1.2.2, the average percolation flux is estimated to be 1.9 cm/day.

To calculate the water content of the fractures and rock matrix, the equilibrated water saturations in the fractures and rock matrix must be computed. Equilibrium flow means that the capillary pressures in the fractures and rock matrix are equal. The capillary pressures for the rock matrix and fractures are given by *UZ Flow Models and Submodels* (SNL 2007a, Equations A-7 and A-10, respectively),

$$P_m = \frac{1}{\alpha_m}\left[S_{em}^{-\frac{1}{m_m}} - 1 \right]^{1-m_m} \quad \text{(Eq. 6)}$$

$$P_f = \frac{1}{\alpha_f}\left[S_{ef}^{\frac{\gamma-1}{m_f}} - 1 \right]^{1-m_f} \quad \text{(Eq. 7)}$$

where α_m and α_f are the rock matrix and fracture van Genuchten capillary strength parameters, respectively; m_m is the van Genuchten pore-size distribution parameter for the rock matrix; S_{em} is the normalized water saturation in the rock matrix; and other parameters are defined in Section 1.2.2. The normalized water saturation in the rock matrix is given by *UZ Flow Models and Submodels* (SNL 2007a, Equation A-8):

$$S_{em} = \frac{S_m - S_{rm}}{1 - S_{rm}} \quad \text{(Eq. 8)}$$

where S_{rm} is the residual water saturation of the rock matrix. The rock matrix water saturation can be expressed as a function of the fracture water saturation by equating P_m and P_f given in Equations 6 and 7.

The water saturation for equilibrium flow can be estimated as for fracture-only flow by treating the process as gravity-driven, unit gradient flow. As before, the effective hydraulic conductivity of the equilibrated fractures and rock matrix system to water equals the average percolation flux. The effective hydraulic conductivity, K_e, is related to the vertical fracture and rock matrix permeabilities and relative permeabilities through the sum of the effective hydraulic conductivities of the fractures and rock matrix, i.e.,:

$$K_e == \frac{\rho g}{\mu}\left(k_f k_{rf} + k_m k_{rm} \right) \quad \text{(Eq. 9)}$$

where k_m is the vertical rock matrix permeability and k_{rm} is the rock matrix relative permeability. The relative permeability for the rock matrix is given by SNL (2007a, Equation A-9):

$$k_{rm} = S_{em}^{\frac{1}{2}}\left[1 - \left\{ 1 - S_{em}^{\frac{1}{m_m}} \right\}^{m_m} \right]^2 \quad \text{(Eq. 10)}$$

The parameter values needed in addition to those given in Table 1-1 are given in Table 1-2,

Table 1-2. Additional Fracture and Rock Matrix Properties for Alcove 1

α_f (Pa^{-1})	α_m (Pa^{-1})	k_m (m^2)	m_m	ϕ_m	S_{rm}
2.43×10^{-3}	1.90×10^{-5}	1.01×10^{-15}	0.346	0.164	0.06

The fracture water saturations may be computed by setting the effective hydraulic conductivity in Equation 9 to the average percolation flux of 1.9 cm/day. This is done using Equations 3, 4, 6, 7, and 8, along with the specified parameter values. Doing this, the fracture water saturation is found to be 0.129. The corresponding rock matrix water saturation is computed using Equations 7 and 8 to give, 0.926. With these values of water saturation and the corresponding porosities, the sum of the fracture and matrix water content is found to be 0.156. Using Equation 5, the estimated maximum transport time is 246 days.

1.2.4 Comparison of Transport Times

Sections 1.2.1 to 1.2.3 showed that the observed, minimum, and maximum transport times are 103, 6.5, and 246 days, respectively. A comparison of these times indicates that transport during the Alcove 1 test consisted of a mixture of transport through fractures and rock matrix. The degree of fracture–matrix interaction is significant in that the observed characteristic transport time is about 16 times longer than the characteristic minimum transport time for transport exclusively through fractures. By comparison, the characteristic maximum transport time, representing fracture–matrix equilibrium, is only about 2.4 times longer than the observed characteristic transport time. Even the breakthrough time of 28 days, which is characteristic of the fastest tracer transport observed in the test, is 4 times longer than the characteristic minimum transport time. Therefore, the travel time results are consistent with the conclusions that matrix diffusion has a significant effect on tracer transport in fractured rock.

1.3 ESTIMATES OF TRACER RELEASE IN INFILTRATING WATER AND RECOVERY IN ALCOVE 1 SEEPAGE WATER

The overall tracer mass released and collected is summarized in this section. However, the seepage water with tracer was still being recovered in significant quantities when the test was terminated. Therefore, an overall mass balance between tracer released and tracer collected in Alcove 1 is not expected.

1.3.1 Tracer Released

Estimates of tracer release in infiltrating water at Alcove 1 can be made from the measurements for infiltration rates and for tracer concentrations. As discussed in Section 1.1, tracer release occurred in the latter part of the test after about 14 months of water release without tracer. Tracer was released for two distinct periods; however, because all chemical analyses of Alcove tracer samples were for the longer-duration second release time period, the estimate for tracer mass release and recovery will address this time period. The total mass release is computed from the product of the average infiltration rate times the tracer concentration and time period for each

time interval to give the tracer mass released for each time interval. The infiltration water contained a low-level background concentration of lithium bromide. Therefore, all tracer concentrations for evaluation of the tracer transport test have been normalized relative to a background lithium bromide concentration of 21 ppm. The sum of the tracer mass released for each interval is then scaled by the infiltration plot area to give the total mass of tracer released. The resulting total mass of tracer released is about 43 kg. Note that the footprint of the infiltration plot, which completely overlies the footprint of the water and tracer collection area in Alcove 1, is about 2.1 times larger than the Alcove 1 collection area (BSC 2004a, Sections 6.12.5.1 and Figure 6-167). Therefore, for vertical flow, the tracer released that may be expected to arrive at Alcove 1 is about 21 kg, assuming that the average infiltration rate for the portion of the infiltration plot that lies above Alcove 1 is the same as the average infiltration rate for the remainder of the infiltration plot.

1.3.2 Tracer Collected in Alcove 1

Tracer collection in Alcove 1 may be estimated in a similar manner to that estimated for the amount of tracer released in the infiltration plot using measured seepage rates and tracer concentrations in Alcove 1. As discussed in Section 1.3.1, all tracer concentrations have been normalized relative to a background lithium bromide concentration of 21 ppm. The total mass collected is computed from the product of the average seepage rate times the tracer concentration and time period for each time interval to give the tracer mass collected for each time interval. The sum of the tracer mass collected for each interval gives a total mass of tracer collected of 5.4 kg. This is about 13% of the total tracer released in the infiltration plot and about 26% of the tracer released in the portion of the infiltration plot overlying Alcove 1.

1.4 EXPLANATION FOR TEMPORAL VARIABILITY IN THE INFILTRATION RATE AND TRACER CONCENTRATION IN INFILTRATING WATER

The fluctuations in infiltration rate were a result of the complexities of applying water to a sloping surface without inducing runoff. When the near surface was saturated, infiltration rates were reduced to ensure water was not moving laterally. Furthermore, adjustments were made to infiltration rates to determine the effects on seepage into Alcove 1. Other factors affecting the infiltration rates were: (1) frozen flow lines that ruptured; (2) equipment failure; (3) clogged drippers; and (4) animals chewing lines.

The lithium bromide tracer concentrations applied at the ground surface for the Alcove 1 transport tests also displayed relatively high amplitude fluctuations, from about 150 to 600 ppm as shown in Figure 1.1. The samples collected to analyze the bromide concentrations were taken from the drip lines used to distribute the source water and tracer in the infiltration plot. The bromide concentration fluctuations were caused by: (1) supersaturation of bromide solution resulting in precipitation of bromide in the solution supply bucket; (2) incomplete mixing of the lithium bromide in the supply solution bucket; and (3) batch bromide analyses that introduced a time delay (on the order of a week) in correcting deviations in solution concentration.

The fluctuations in infiltration rate and tracer concentration for the Alcove 1 test-bed model were accounted for in the numerical modeling by using directly the measured infiltration rates and

tracer concentrations as model boundary conditions. Therefore, these fluctuations did not have an adverse impact on comparisons of model results with test data.

2. COMMITMENTS TO THE NRC

None

3. DESCRIPTION OF PROPOSED LA CHANGE

None

4. REFERENCES

BSC (Bechtel SAIC Company) 2004a. *In Situ Field Testing of Processes.* ANL-NBS-HS-000005 REV 03. Las Vegas, Nevada: Bechtel SAIC Company. ACC: DOC.20041109.0001; DOC.20051010.0001; DOC.20060508.0001.

BSC 2004b. *Analysis of Hydrologic Properties Data.* ANL-NBS-HS-000042 REV 00. Las Vegas, Nevada: Bechtel SAIC Company. ACC: DOC.20041005.0004; DOC.20050815.0003; LLR.20080416.0162; LLR.20080522.0162.

SNL (Sandia National Laboratories) 2007a. *UZ Flow Models and Submodels.* MDL-NBS-HS-000006 REV 03 AD 01. Las Vegas, Nevada: Sandia National Laboratories. ACC: DOC.20080108.0003; DOC.20080114.0001; LLR.20080414.0007; LLR.20080414.0033; LLR.20080522.0086.

SNL 2007b. *Calibrated Unsaturated Zone Properties.* ANL-NBS-HS-000058 REV 00. Las Vegas, Nevada: Sandia National Laboratories. ACC: DOC.20070530.0013; DOC.20070713.0005; LLR.20080423.0015; LLR.20080527.0082.

RAI Volume 3, Chapter 2.2.1.3.7, First Set, Number 9:

Explain how the transport of irreversible colloids from the EBS to the UZ is represented, particularly with regard to nonseeping drift conditions that appear to favor the release of radionuclides to the matrix continuum. If the colloids are released from the EBS directly to the UZ matrix continuum by the EBS-UZ interface model, describe how the initiation of transport in the matrix affects the transport of irreversible colloids compared to initiation of transport in fractures.

Basis: DOE did not provide details in SAR (2008) or in supporting AMRs to describe how the mass flux of irreversible colloids is handled by the advective and diffusive flux-splitting approaches implemented at the interface between the EBS and the UZ. In particular, it is not apparent how DOE models the subsequent transport of irreversible colloids in the UZ if they are released to the matrix from nonseeping drifts in the EBS. The information is needed to verify compliance with 10 CFR 63.114(a) and (b).

1. RESPONSE

1.1 TRANSPORT OF IRREVERSIBLE COLLOIDS FROM THE EBS TO UZ UNDER NONSEEPING CONDITIONS.

Irreversible colloids are released from the EBS directly to the unsaturated zone fracture and matrix continua by the EBS-unsaturated zone interface model. Transport under nonseeping conditions is discussed at the end of this section.

SAR Figure 2.3.7-8, reproduced here as Figure 1, shows the flow pathways (F1 through F8) in the EBS. The flow pathway between the invert and unsaturated zone is F8 in SAR Figure 2.3.7-8. F8 is the sum of F6 and F7, which are modeled as separate pathways as clarified in Figure 2.

Table 1 lists the four radionuclide fluxes in pathway F8 as shown in SAR Figure 2.3.7-47 (reproduced as Figure 3):

Table 1. Radionuclide Fluxes in SAR Figure 2.3.7-47, Pathway F8

Fluxes in SAR Figure 2.3.7-47	Pathway in SAR Figure 2.3.7-8
Advective flux from the invert to the unsaturated zone fracture, middle column, row 1, cell	F6
Diffusive flux between the invert and the unsaturated zone fracture, middle column, row 1, cell	
Advective flux from the invert to the unsaturated zone matrix, middle column, row 1, cell	F7
Diffusive flux between the invert and the unsaturated zone matrix, middle column, row 1, cell	

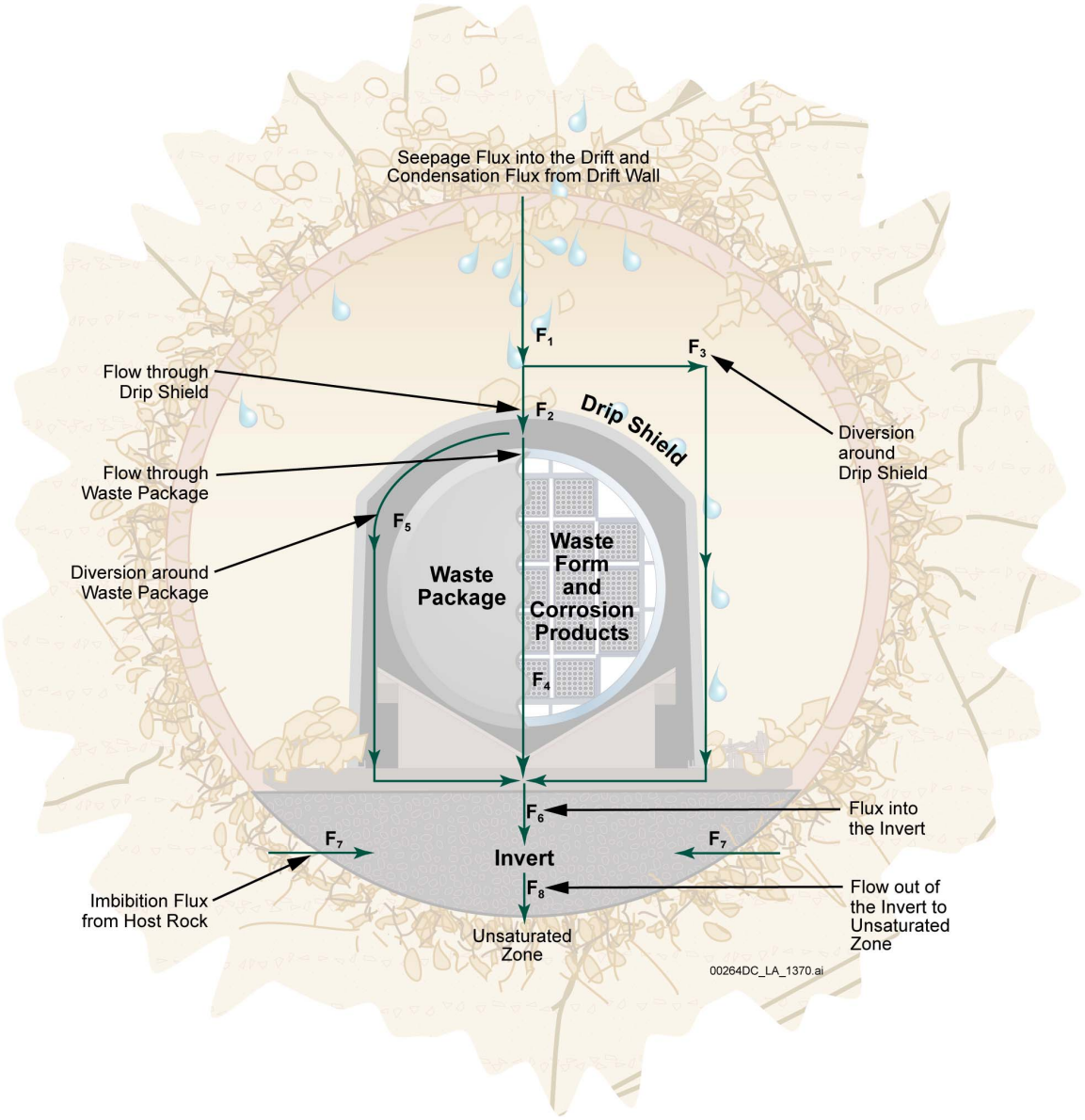

Source: SAR Figure 2.3.7-8.

NOTE: Flow paths are labeled F1 to F8.

Figure 1. Potential Flow Pathways in the Engineered Barrier System

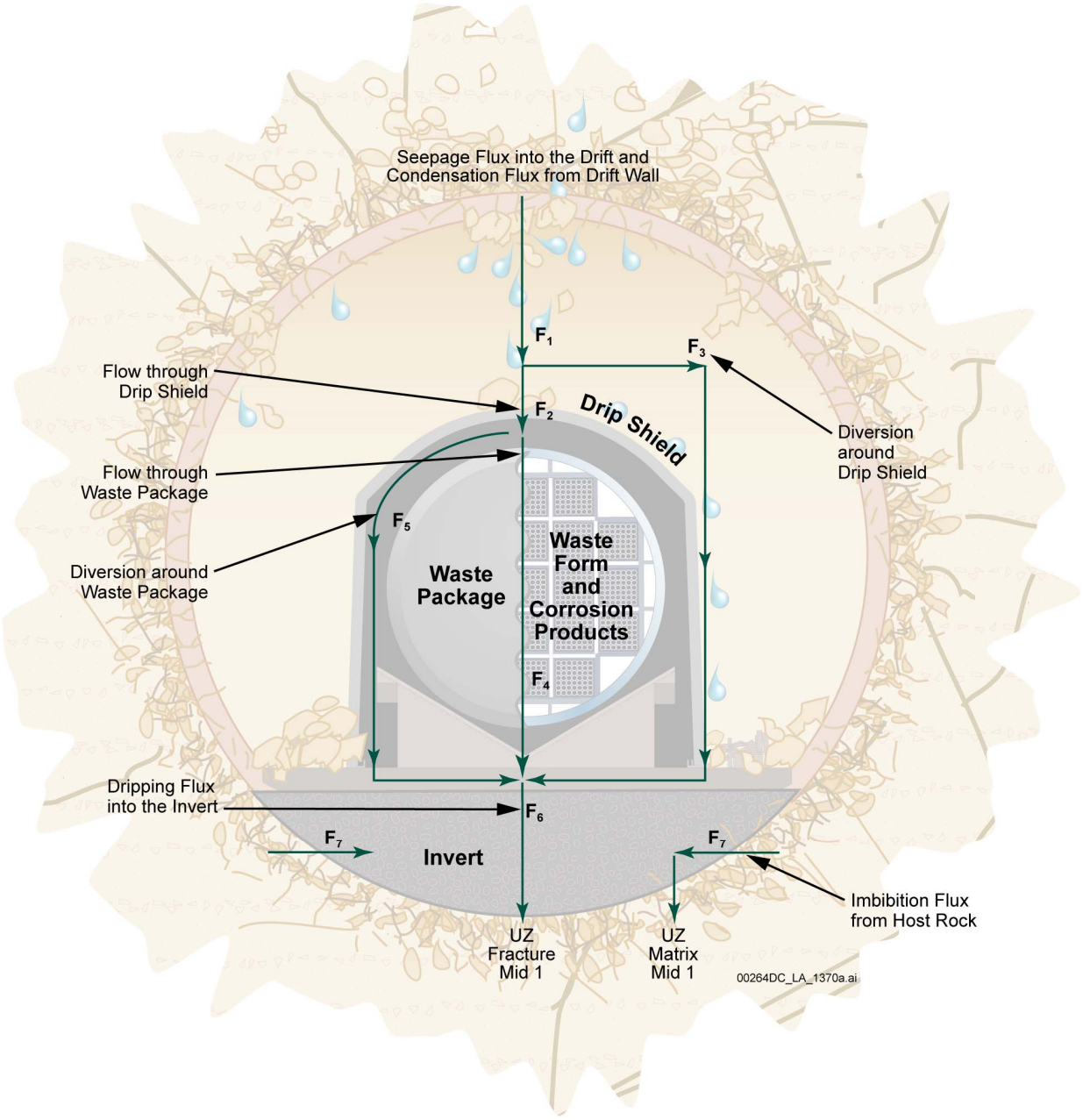

Source: Modified from SAR Figures 2.3.7-8 and 2.3.7-47.

Figure 2. Potential Flow Pathways in the EBS, Clarifying Flow Pathways F6 and F7

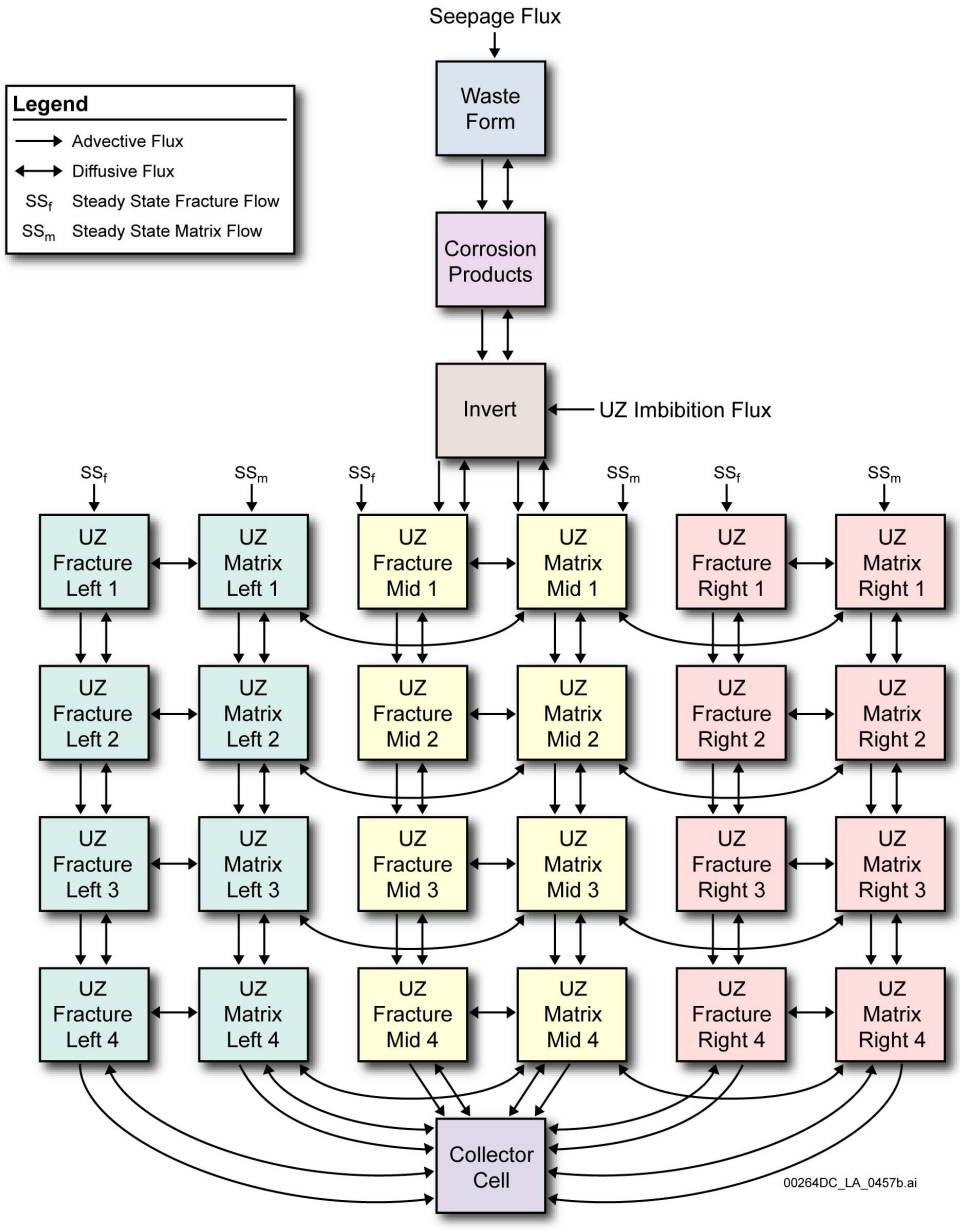

Source: SAR Figure 2.3.7-47.

Figure 3. Computational Grid in the Engineered Barrier System–Unsaturated Zone Interface Model

Figure 3 illustrates the discretization of the EBS-unsaturated zone interface model. The invert, "UZ Fracture Mid 1" (UZ fracture middle column, row 1 of SAR Figure 2.3.7-47), and "UZ Matrix Mid 1" (UZ matrix middle column, row 1), are all modeled as mixing cells within the EBS-unsaturated zone interface model. Radionuclides may transport between invert cell and unsaturated zone cells in the two flow pathways as four different fluxes. Advective radionuclide fluxes are determined by the radionuclide concentration within the invert cell and the flow rates into the two unsaturated zone cells. Diffusive radionuclide fluxes are determined by the

concentration gradients between the invert cell and unsaturated zone cells and the transport parameters of the diffusive pathways between these cells. Thus, the radionuclides entering the invert mixing cell along flow path F6 mix with the imbibition water entering the invert along flow path F7, and then transport out of the invert into the unsaturated zone fractures along flow path F6 and into the unsaturated zone matrix along flow path F7.

Radionuclides, both dissolved and colloidal, can transport between the EBS and the unsaturated zone, along pathway F6, by advection and diffusion into the unsaturated zone fracture continuum. The dripping water flux in pathway F6 is composed of the seepage flux and the drift wall condensation flux. Within the nonseeping environment the seepage flux is zero, but there may be advection from the EBS to the unsaturated zone due to drift wall condensation. When condensation is also zero, there is no advective flux into the unsaturated zone fractures, but diffusive flux based on the concentration gradient between the invert and unsaturated zone fractures may occur.

Radionuclides, both dissolved and colloidal, can transport between the EBS and the unsaturated zone, along pathway F7 (flow imbibed from the host rock and transported by gravity to the unsaturated zone matrix), by advection or diffusion into the unsaturated zone matrix continuum. There is no size exclusion at the EBS–unsaturated zone matrix interface, so all sizes of irreversible colloids are transported into the unsaturated zone matrix. Imbibition along F7 may provide a small advective flux into the unsaturated zone matrix in both the seeping and nonseeping environments. Diffusion between the invert and unsaturated zone matrix depends on the concentration gradients, with colloids diffusing much slower than dissolved species due to their larger size.

In the case of no dripping flux (i.e., there is no seepage or condensation (F1 is 0)), then radionuclides can only move out of the waste package by diffusion through continuous films of water along pathway F4 into the invert mixing cell. From the invert cell, the radionuclides may diffuse along pathway F6 into the unsaturated zone fractures, diffuse along pathway F7 into the unsaturated zone matrix, and advect along pathway F7 in to the unsaturated zone matrix. The splitting of diffusive flux between F6 and F7 is determined by the concentration gradients and the transport parameters of the diffusive pathways between the invert and unsaturated zone cells, and favors flux into the matrix in the nonseeping case.

1.2 INITIATION OF TRANSPORT OF IRREVERSIBLE COLLOIDS IN THE UNSATURATED ZONE

Once radionuclides have been passed from the EBS into the unsaturated zone fractures and matrix, they are transported through the unsaturated zone as described in SAR Section 2.3.8. In particular, the irreversible colloids that enter the unsaturated zone matrix can undergo advective transport within the matrix and advective transport from the matrix to the fracture. Colloid matrix diffusion is conservatively excluded because of the low diffusivities for most colloids. Advective transport from the fractures into the matrix has size exclusion. Retardation of irreversible colloids, due to colloid attachment/detachment processes, within the fracture continuum is modeled, but retardation within the matrix continuum is conservatively excluded. Even so, in the northern region where 71% of the repository release nodes reside, the rate of flow in the

fractures is so much faster than in the matrix that the irreversible colloids travel faster within the fracture continuum than the matrix continuum.

SAR Figure 2.3.8-49 compares the unsaturated zone breakthrough curves for ^{99}Tc released from the EBS at the fracture node and the matrix node at both the northern and southern release locations. Even though ^{99}Tc undergoes matrix diffusion, while irreversible colloids do not, this figure and associated text are informative. They show that in the northern release location ^{99}Tc released into a matrix node is transported through the unsaturated zone much more slowly than that released into a fracture node (SAR Figure 2.3.8-49a). This is due to the time needed for ^{99}Tc to diffuse from the matrix to the fracture, where transport is fast. With irreversible colloids, there is no diffusion from the matrix to the fracture so they remain within the matrix where they are slowly transported by advection either back to the fracture or to the water table. Accordingly, the difference in travel time for colloids in the north between the fracture or matrix release would be even larger than the difference seen for ^{99}Tc. In the southern region, it makes little difference whether ^{99}Tc is released to the unsaturated zone at a fracture or a matrix node (SAR Figure 2.3.8-49b). This is because flow through the Calico Hills non-welded (CHn) vitric rock matrix controls radionuclide transport in the southern region, which is slow. Transport through the CHn matrix should be similar for irreversible colloids, since there is no retardation within the matrix for either ^{99}Tc or irreversible colloids. However, some differences will be present because irreversible colloids do not diffuse within the matrix as ^{99}Tc does, and once released into the fractures in lower units, irreversible colloids are retarded on the fracture walls where ^{99}Tc is not. Thus, in the north, there would be a large difference in irreversible colloid unsaturated zone transport between initiation in the fracture or matrix. In the south, unsaturated zone transport is slower and less dependent on the location of initiation of transport.

In summary, the initiation of transport in the matrix generally slows the transport of irreversible colloids compared to initiation of transport in the fractures.

Finally, a minor error was noted in SAR Section 3.2.7.12.3.2 that is corrected in Section 3. Although related to this RAI response, the error and correction do not affect this RAI response.

2. COMMITMENTS TO NRC

The DOE commits to update the license application as described in Section 3. The change to be made will be included in a future license application update.

3. DESCRIPTION OF PROPOSED LA CHANGE

In SAR Section 2.3.7.12.3.2, p 2.3.7-81, the text:

> All the water that is imbibed from the rock matrix by the invert (*F7*) is assumed to flow subsequently into the unsaturated zone matrix, along with any condensation and seepage flux.

will be replaced with:

> All the water that is imbibed from the rock matrix by the invert (*F7*) is assumed to flow subsequently into the unsaturated zone matrix.

RAI Volume 3, Chapter 2.2.1.3.7, First Set, Number 10:

Reconcile apparent differences in the SAR regarding arrival time for plutonium associated with irreversible colloids.

Basis: Modeling results presented in the SAR indicate that plutonium is transported more readily through the UZ as a solute or reversible colloid than as an irreversible colloid. The modeled arrival time of irreversible colloids is longer than and contributes less to ^{242}Pu activity releases from the UZ than the dissolved and reversible colloids in the UZ (e.g., SAR Fig. 2.4-108). However, results presented elsewhere in the SAR indicate that irreversible colloids have short travel times in the UZ (e.g., SAR Section 2.3.8.5.4). The information is needed to verify compliance with 10 CFR 63.114(a) and (b).

1. RESPONSE

This response primarily consists of a synthesis of information contained within SAR Sections 2.3.8.5.4 and 2.4, as well as information in *Particle Tracking Model and Abstraction of Transport Processes* (SNL 2008b). The crux of the response is two-fold: (1) it is not appropriate to compare results from two different samplings of the uncertain unsaturated zone parameters (SAR Figure 2.4-108 was created with a different parameter sampling than SAR Figures 2.3.8-47 and 2.3.8-48) and (2) the TSPA realization in Figure 2.4-108 is for a diffusive release case wherein plutonium on irreversible colloids is released at a much lower rate than aqueous plutonium, which appears to result in a shorter transport time for irreversible colloids given the truncated *y*-axis scale of Figure 2.4-108—replotting Figure 2.4-108 on expanded scales more clearly shows the relative travel times.

1.1 PARAMETER SAMPLING

SAR Figure 2.4-108 is part of a detailed discussion of a single realization out of 9,000 in the 1,000,000-year seismic ground motion modeling case (SAR Section 2.4.2.2.3.2.2). Its purpose is for TSPA model validation to enhance confidence that there is consistent behavior between the total system model and the submodels that comprise it. This particular realization represents epistemic uncertainty vector 155, which is a particular sampling of uncertain parameters in all submodels of the TSPA model (SNL 2008a), including parameters related to retardation of slow irreversible colloids in the unsaturated zone, as well as other flow and transport properties of the unsaturated zone (e.g., it sampled the 30th-percentile infiltration scenario and a value of about 36 for the unsaturated zone colloid retardation factor). Figures 2.3.8-47 and 2.3.8-48 from SAR Section 2.3.8.5.4 represent a different sampling of the unsaturated zone parameters, as shown in SAR Table 2.3.8-9, including the 10th-percentile infiltration scenario and a colloid retardation factor of 26. Because of the wide uncertainty range of key unsaturated zone parameters, such as the matrix diffusion coefficient and the sorption coefficient (e.g., see SAR Figure 2.3.8-53), it is not generally possible to directly compare the relative behavior of colloidal and aqueous transport between realizations. A more appropriate comparison is to consider either the full range of this behavior or the mean of the behavior.

For example, consider SAR Figures 2.3.8-47a and 2.3.8-48a, which show the normalized breakthrough curves for aqueous ^{242}Pu and irreversible ^{242}Pu (slow (retarded or filtered) (Ic^{242}Pu) and fast (unretarded) (If^{242}Pu)), respectively, from both northern and southern release locations for a representative case that used median values from the unsaturated zone parameter uncertainty distributions. It is clear on SAR Figure 2.3.8-47a for this particular parameter sampling that aqueous ^{242}Pu released into the fracture continuum at the top of the unsaturated zone in the northern locations transports more quickly through the unsaturated zone than Ic^{242}Pu (with 50% breakthrough times of about 20 years and 100 years, respectively). This is the opposite behavior as that implied in the RAI. For the southern release locations, where mass releases are dominated by travel through the vitric CHn matrix, aqueous ^{242}Pu has a 50% breakthrough time greater than 1,000,000 years, compared to the much shorter Ic^{242}Pu breakthrough time of about 1,000 years (If^{242}Pu is not discussed in the foregoing, because it represents only 0.168% of the ^{242}Pu mass transported by irreversible colloids (SNL 2008a, Section 6.3.8.3).)

An even better demonstration of why it is more appropriate to compare full uncertainty ranges, rather than two specific realizations, is shown by comparing SAR Figure 2.3.8-53a with Figure 1(a) . These two figures show the transport behavior of ^{240}Pu as a function of the uncertainty range of several key transport parameters, which will be the same as the transport behavior of ^{242}Pu except for radioactive decay effects. SAR Figure 2.3.8-53a for the GT10 flow field indicates that the aqueous ^{240}Pu travel time through the unsaturated zone from a northern release location varies between about 20 and 1000 years, depending on the sampled values of matrix diffusion coefficient and plutonium sorption coefficient. Figure 1(a) shows that for the GT10 flow field the Ic^{240}Pu mean travel time through the unsaturated zone from a northern release location can vary between about 25 and 3,000 years, depending on the value of the colloid retardation factor. Thus, for northern release locations, there is no general characterization of whether transport is faster for aqueous ^{240}Pu or for slow irreversible ^{240}Pu (The fast irreversible ^{240}Pu will always be transported more quickly than either of the previous two forms of ^{240}Pu, but it represents a very small fraction of the overall mass of ^{240}Pu released from the EBS (SNL 2008a, Section 7.7.1.4[a])).

Although there is no significant difference in the simulated transport of dissolved and irreversible slow colloids in the northern portion of the repository block, there is a significant difference in the southern portion. For those locations, a general conclusion can be drawn that aqueous ^{240}Pu transport is always much slower than Ic^{240}Pu transport (and similarly for ^{242}Pu). This is apparent by a comparison of SAR Figure 2.3.8-54, showing mean travel times of ^{240}Pu (aqueous) for the southern release location as a function of log (Dm) and Kd, with Figure 1(b), showing mean travel times of ^{240}Pu (irreversible on colloids) for the southern release location as a function of colloid retardation factor. The mean travel times of ^{240}Pu (aqueous) (SAR Figure 2.3.8-54) for the southern release location range from less than 50,000 years to greater than 500,000 years. The mean travel times of ^{240}Pu (irreversible on colloids) (Figure 1(b)), range from around 1,000 to 4,000 years. This large contrast in travel-times over a wide range of parameter values highlights the much more rapid transport of ^{240}Pu (irreversible on colloids) compared to ^{240}Pu (aqueous) in the southern portion of the repository.

1.2 ANALYSIS OF SAR FIGURE 2.4-108

SAR Figure 2.4-108 (see Figure 2) contains three sets of curves. One set is comprised of the EBS, unsaturated zone, and saturated zone cumulative releases of ^{99}Tc. The second set is comprised of the EBS, unsaturated zone, and saturated zone cumulative releases of ^{242}Pu migrating as a combined dissolved phase and reversibly sorbed to a smectite colloid phase. The third set is comprised of the cumulative EBS, unsaturated zone, and saturated zone releases of ^{242}Pu irreversibly sorbed to both waste-form colloids and iron oxyhydroxide colloids. The irreversibly sorbed ^{242}Pu travels through the Lower Natural Barrier (unsaturated zone and saturated zone features) as both slow (retarded) and fast (unretarded) irreversible colloids (SAR 2.3.8.5.4). The curves in SAR Figure 2.4-108 designated as "irreversible on colloids" represent the sum of the releases from the slow and fast irreversible colloids.

The initial part of the cumulative breakthrough curves must be examined to compare the relative travel times of ^{242}Pu migrating as dissolved and reversibly sorbed in local equilibrium (^{242}Pu (aqueous)) with the travel time of ^{242}Pu migrating as irreversibly sorbed onto colloids (^{242}Pu (irreversible on colloids)). To do this, it is necessary to expand both the *y*- and *x*-axis scales of SAR Figure 2.4-108 so that the entire transport history of both sets of ^{242}Pu transport curves can be seen (see Figures 3 and 4). As can be seen in Figures 3 and 4, EBS releases for both ^{242}Pu (aqueous) and ^{242}Pu (irreversible on colloids) actually begin at the same time (24,500 years), which is the time of the first damaging seismic event to codisposal waste packages. This was not apparent in SAR Figure 2.4-108 because of the axis scaling. Also, the early-time cumulative mass for irreversible colloids released from the EBS is much lower than the aqueous phase releases, which apparently causes the aqueous phase arrival times to appear earlier on SAR Figure 2.4-108 with the particular *x*- and *y*-axis scales shown in that figure. The expanded scales shown in Figures 3 and 4 eliminates this graphical effect. Note that on Figures 3 and 4 the unsaturated zone releases appear to start at the same time as the EBS releases, which reflects the fact that the cumulative release curve is integrated over 500-year timesteps at 24,500 years, which is too large to distinguish initial EBS releases from initial unsaturated zone releases. These initial unsaturated zone releases represent mass transported with a relatively fast travel time through the northern portion of the repository for both aqueous ^{242}Pu and irreversible ^{242}Pu.

The much larger EBS aqueous release compared to irreversible colloid release in SAR Figure 2.4-108 is attributable to differences in the transport properties between aqueous and colloidal phases for early diffusion-dominated EBS releases from damaged waste packages in the seismic ground motion modeling case (i.e., diffusive transport of colloids is a very slow transport mechanism), which means that ^{242}Pu release on irreversible colloids is very small. The relative difference in the amount of mass transported from the EBS as dissolved/reversibly-sorbed versus irreversibly sorbed can be seen in SAR Figures 2.4-104 and 2.4-106. Also, as is apparent from these figures, these early releases of irreversible colloids are only from codisposal waste packages (which are the only breached packages at early times in this single realization) and therefore they are waste-form or glass colloids. Furthermore, as shown in SAR Figure 2.4-104, the concentration of ^{242}Pu irreversibly attached to codisposal glass waste-form colloids is very low in the first 50,000 years, indicating an unstable colloid suspension due to the high ionic strength, which is characteristic of diffusive release scenarios. This low concentration implies much lower release rates than for aqueous ^{242}Pu. The high ionic strength in the

codisposal waste package corrosion products domain is shown in Figure 5. Comparing this figure to the upper right stability plot on Figure 6.3.7-12 in *Total System Performance Assessment Model /Analysis for the License Application* (SNL 2008a), shows that the ionic strength prior to about 50,000 years is higher than about 0.4 mol/kg, which is the stability limit for a glass colloid suspension.

1.3 SUMMARY

This response reconciles perceived differences in the SAR regarding arrival time for dissolved plutonium and plutonium associated with irreversible colloids. The crux of the response is two-fold: (1) it is not necessarily appropriate to compare results from two different samplings of the uncertain unsaturated zone parameters (SAR Figure 2.4-108 was created with a different parameter sampling than SAR Figures 2.3.8-47 and 2.3.8-48), and (2) the TSPA realization in Figure 2.4-108 is for a diffusive release case wherein plutonium on irreversible colloids is released at a much lower rate than aqueous plutonium, which appears to result in a shorter transport time for irreversible colloids given the truncated *y*-axis scale of Figure 2.4-108 replotting Figure 2.4-108 on expanded scales more clearly shows the relative travel times.

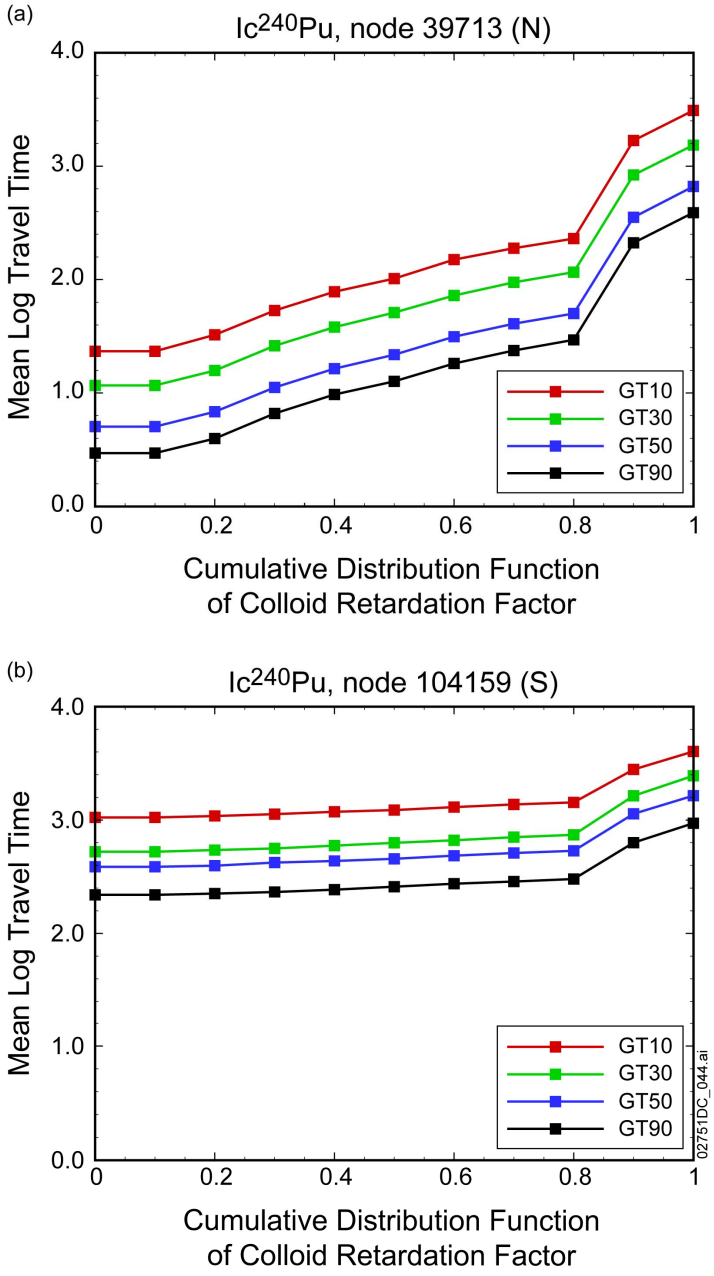

Source: SNL 2008b, Figure 6.8.2-23[c] (#2)

Figure 1. Mean Travel Time of $Ic^{240}Pu$ as a Function of Colloid Retardation Factor for the Glacial-Transition Climate Condition, with Colloid Filtration: (a) is the northern release location and (b) is the southern release location

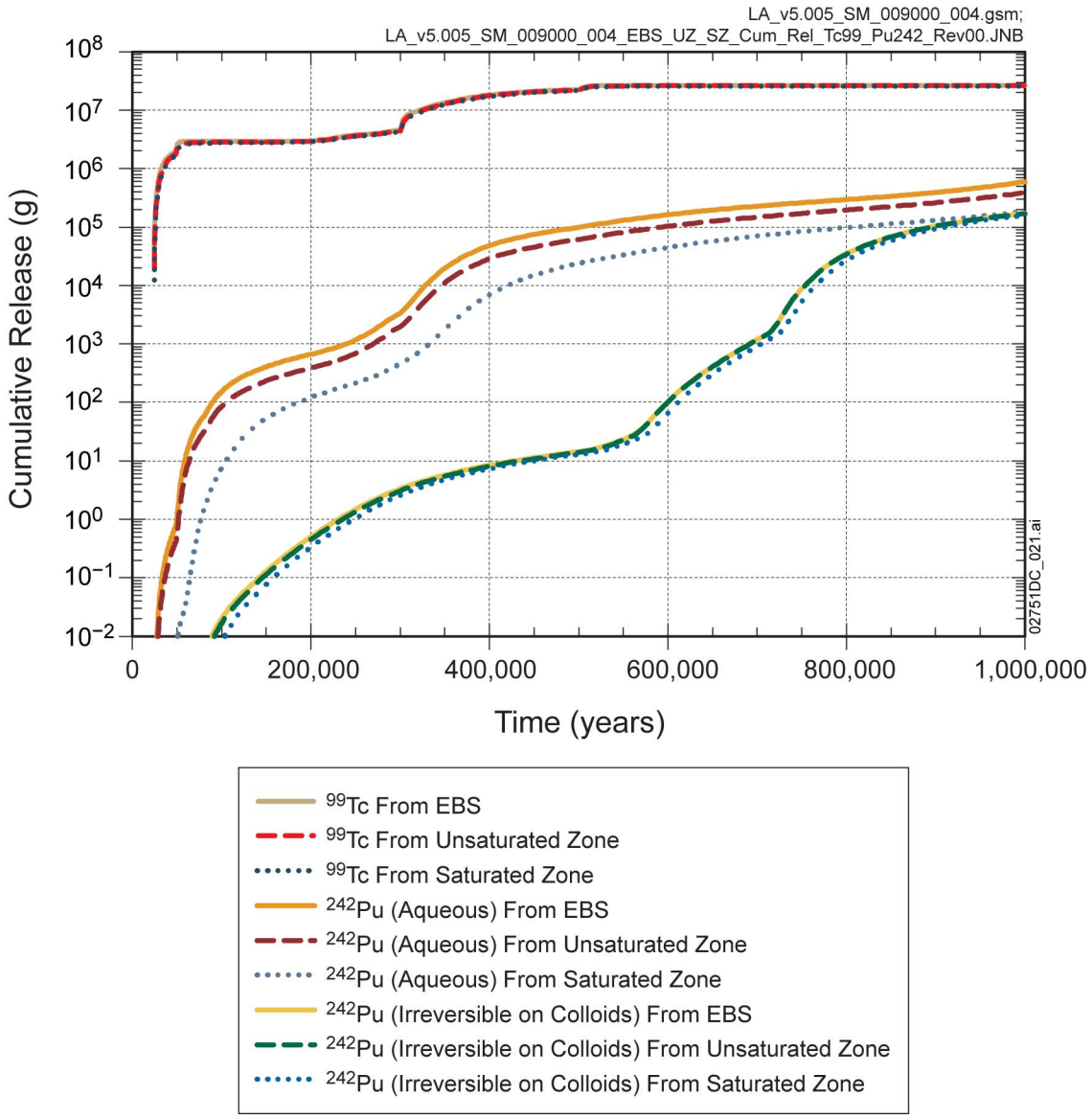

Source: SNL 2008a, Figure 7.7.1-71[a].

NOTE: Plutonium dissolved and reversibly associated with colloids is denoted as aqueous.

Figure 2. Cumulative Mass Released of ^{99}Tc and ^{242}Pu from the Engineered Barrier System, Unsaturated Zone and Saturated Zone for Realization 4,641 of the Seismic Ground Motion Modeling Case for the 1-Million-Year Period after Repository Closure (SAR Figure 2.4-108)

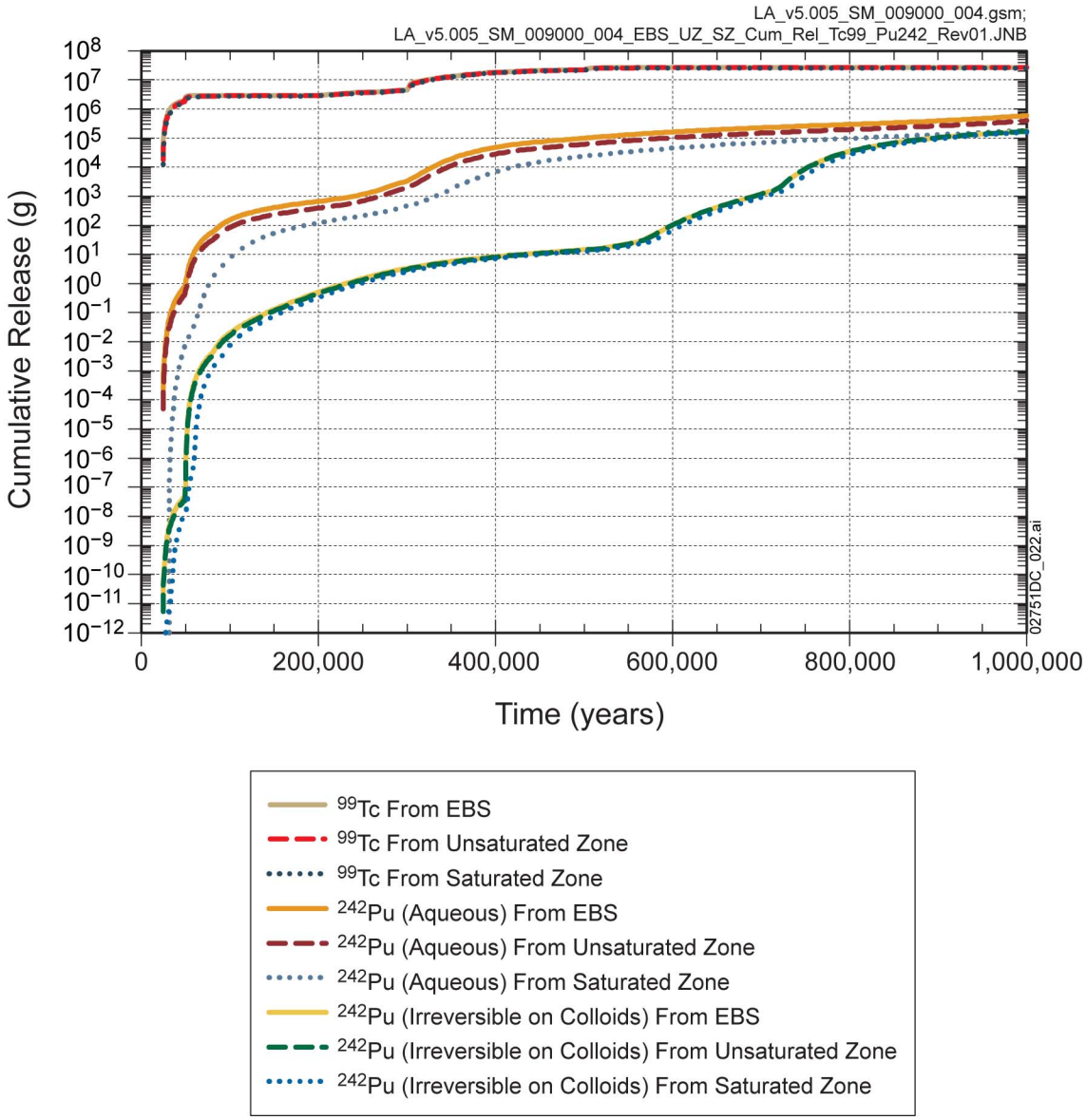

Source: SNL 2008a, Figure 7.7.1-71[a].

NOTE: Plutonium dissolved and reversibly associated with colloids is denoted as aqueous.

Figure 3. Cumulative Mass Released of ^{99}Tc and ^{242}Pu from the Engineered Barrier System, Unsaturated Zone and Saturated Zone for Realization 4,641 of the Seismic Ground Motion Modeling Case for the 1-Million-Year Period after Repository Closure (with Cumulative Release Scale Expanded) (modified from SAR Figure 2.4-108)

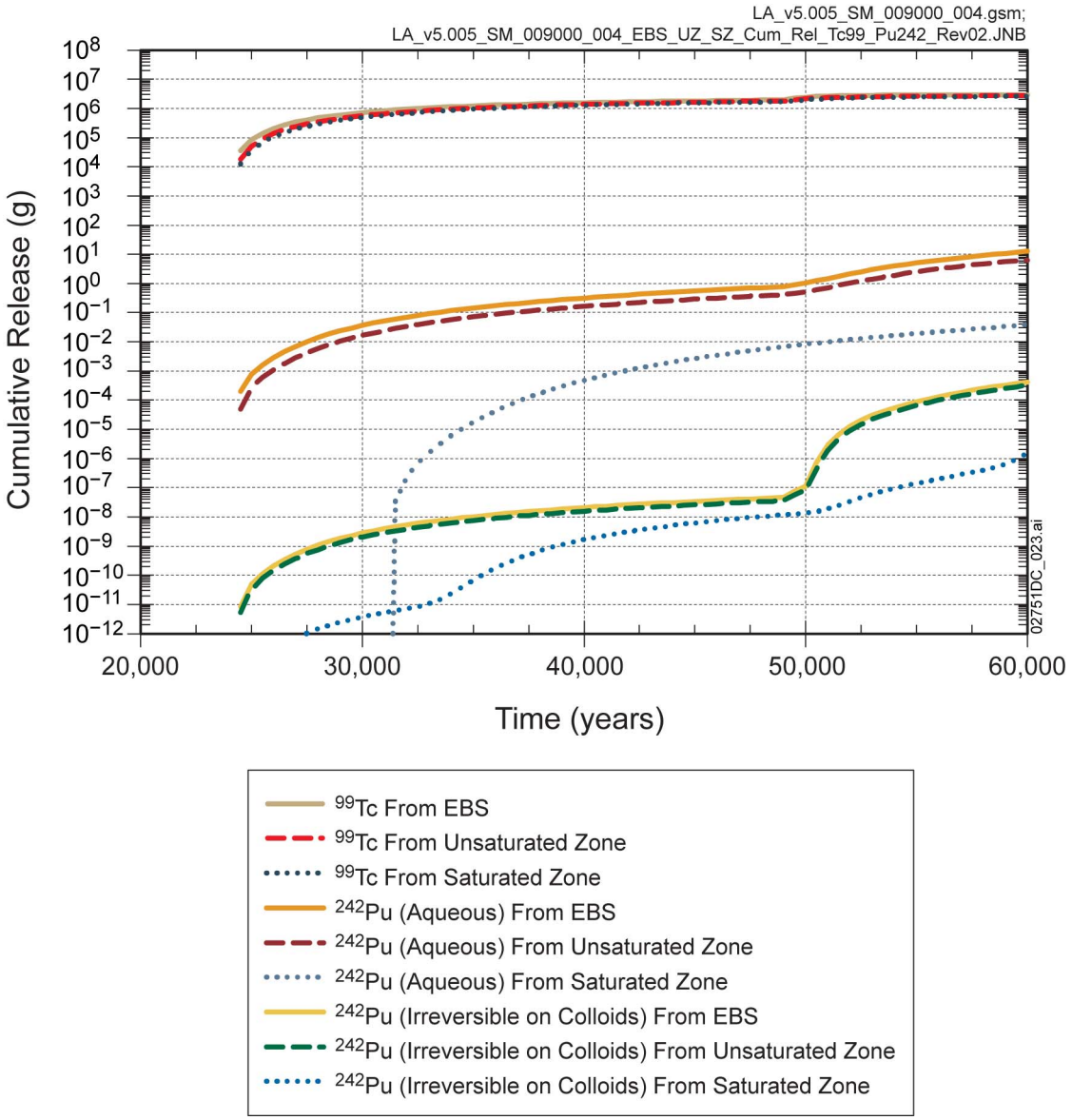

Source: SNL 2008a, Figure 7.7.1-71[a].

NOTE: Plutonium dissolved and reversibly associated with colloids is denoted as aqueous.

Figure 4. Cumulative Mass Released of ^{99}Tc and ^{242}Pu from the Engineered Barrier System, Unsaturated Zone and Saturated Zone for Realization 4,641 of the Seismic Ground Motion Modeling Case for the 1-Million-Year Period after Repository Closure (with Cumulative Release Scale Expanded and Range of Time Scale Reduced) (modified from SAR Figure 2.4-108)

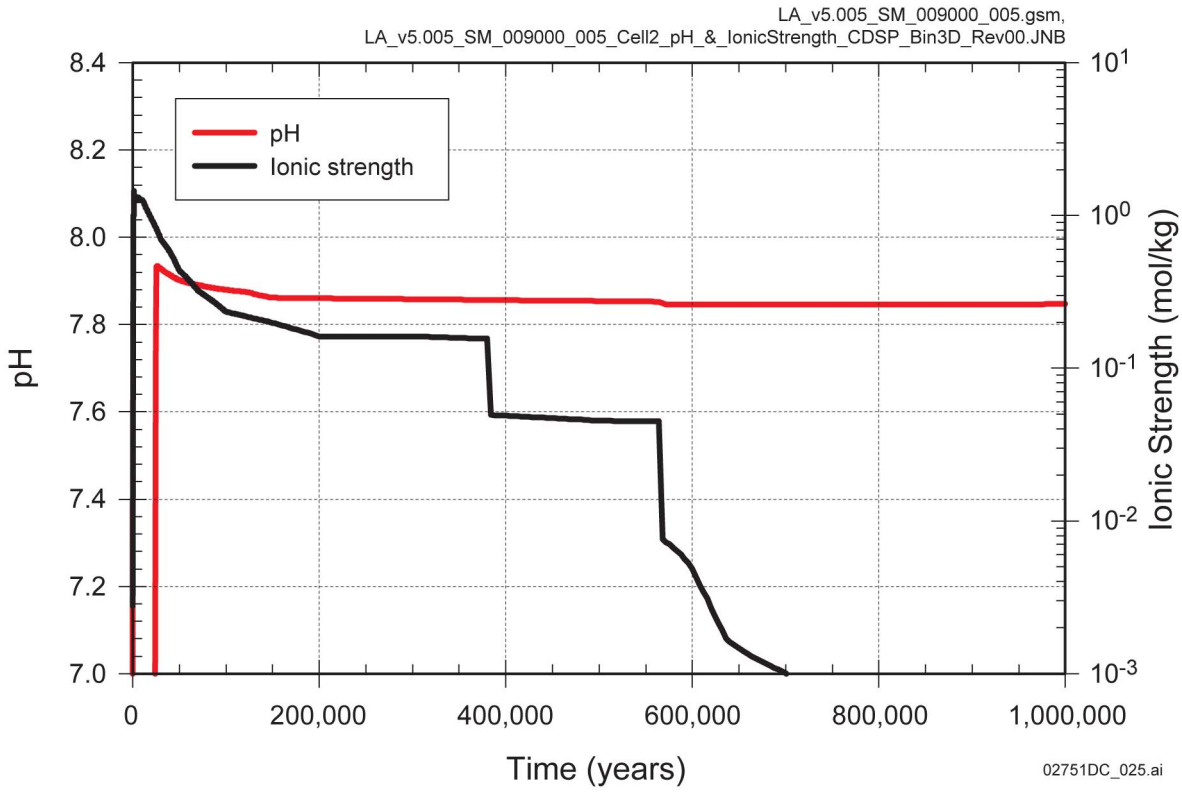

Figure 5. pH and Ionic Strength Profiles in the Corrosion Products Domain for Codisposal Waste Packages in Percolation Subregion 3 Seeping Environment for Realization 4,641 of the Seismic Ground Motion Modeling Case for the 1-Million-Year Period after Repository Closure

2. COMMITMENTS TO NRC

None.

3. DESCRIPTION OF PROPOSED LA CHANGE

None.

4. REFERENCES

SNL (Sandia National Laboratories) 2008a. *Total System Performance Assessment Model /Analysis for the License Application.* MDL-WIS-PA-000005 REV 00 AD 01. Las Vegas, Nevada: Sandia National Laboratories. ACC: DOC.20080312.0001; LLR.20080414.0037; LLR.20080507.0002; LLR.20080522.0113.

SNL (Sandia National Laboratories) 2008b. *Particle Tracking Model and Abstraction of Transport Processes.* MDL-NBS-HS-000020 REV 02 AD 02. Las Vegas, Nevada: Sandia National Laboratories. ACC: DOC.20080129.0008; DOC.20070920.0003; LLR.20080325.0287; LLR.20080522.0170.

RAI Volume 3, Chapter 2.2.1.3.7, First Set, Number 11:

Explain how TSPA represents the status of irreversible colloids that are permanently filtered at a matrix - matrix interface if the interface becomes saturated when water table rises due to future climate change.

Basis: DOE states that colloid transport is more important to waste isolation in the saturated zone than in unsaturated zone, but no explanation is provided in the SAR for the potential effects of remobilization of irreversible colloids trapped at a UZ interface by colloid exclusion if saturation and flow rates at the interface change. The information is needed to verify compliance with 10 CFR 63.114(a) and (b).

1. RESPONSE

Unsaturated zone matrix–matrix interface filtration was not implemented in the final TSPA-LA model (SNL 2008a). The only colloid filtration implemented in TSPA-LA in the unsaturated zone is "physical straining at fracture-matrix interfaces resulting in size exclusion and preferential transport of colloids within the fracture domain" (SAR Section 2.3.8.4.5.4). Note that the fracture–matrix straining model does not use the colloid size used in the matrix–matrix filtration model, but a size exclusion factor for each rock unit based on the percent of pores greater than 100 nm (SNL 2008c, Section 6.5.10). Irreversible colloids excluded from the matrix due to size, are modeled to remain in the fracture where they transport in the unsaturated zone as described in SAR Section 2.3.8. If the fractures and matrix become saturated when the water table rises due to future climate change, then the irreversible colloids are modeled to be transported in the saturated zone as described in SAR Section 2.3.9.3.3.3.4.

Particle Tracking Model and Abstraction of Transport Process (SNL 2008b) indicates that an error in the implementation of FEHM in GOLDSIM results in the particles being assigned a size of zero. Since zero is smaller than any sampled pore size, there is no chance of matrix–matrix filtration. This document provides additional simulations comparing unsaturated zone breakthrough curves with and without matrix–matrix filtration of irreversible colloids. The effect of removing colloid matrix-matrix filtration is negligible in the northern area because of fast travel times (SNL 2008b, p. 3 and Figures 6.6.2-6[c]a and c). In the southern area the effect is more pronounced but conservative. Without matrix-matrix filtration, a greater portion of the radionuclides attached to colloids exit the unsaturated zone flow system before decaying, resulting in slightly higher dose. The case without matrix-matrix filtration is the version of the unsaturated zone abstraction model that was implemented in TSPA-LA.

In summary, TSPA does not model irreversible colloids to be permanently filtered at a matrix-matrix interface. Colloids that are filtered by size exclusion at the fracture–matrix interface are not trapped, but transported within the fractures. Therefore there is no "remobilization of irreversible colloids trapped at an unsaturated zone interface by colloid exclusion if saturation and flow rates at the interface change."

2. COMMITMENTS TO NRC

None.

3. DESCRIPTION OF PROPOSED LA CHANGE

None.

4. REFERENCES

SNL 2008a. *Total System Performance Assessment Model /Analysis for the License Application*. MDL-WIS-PA-000005 REV 00 AD 01. Las Vegas, Nevada: Sandia National Laboratories. ACC: DOC.20080312.0001; LLR.20080414.0037; LLR.20080507.0002; LLR.20080522.0113.

SNL 2008b. *Particle Tracking Model and Abstraction of Transport Processes*. MDL-NBS-HS-000020 REV 02 AD 02. Las Vegas, Nevada: Sandia National Laboratories. ACC: DOC.20080129.0008; DOC.20070920.0003; LLR.20080325.0287; LLR.20080522.0170.

RAI: Volume 3, Chapter 2.2.1.3.7, First Set, Number 12:

Explain why uncertainty about the fraction of irreversible colloids that travel unretarded (i.e., the fast irreversible colloid fraction) is not propagated in the UZ transport abstraction.

Basis: DOE assigned a fixed value (0.00168) in TSPA to represent the fraction of fast irreversible colloids in the transport abstraction. DOE acknowledged that the selected value is uncertain. DOE identified a cumulative distribution function for this parameter but did not provide a technical basis or sensitivity analysis to support the use of a constant value for all transport calculations. The information is needed to verify compliance with 10 CFR 63.114(b).

1. RESPONSE

Uncertainty about the fraction of irreversible colloids that travel unretarded (i.e., the fast irreversible colloid fraction) is not propagated in the unsaturated zone transport abstraction because this uncertainty is handled by using a conservative fixed value. In addition, it is shown below that the dose from the fast fraction is insignificant when represented with a conservative fixed value; therefore, it does not need to be modeled by an uncertainty distribution.

A conservative approach for managing uncertainty (NRC 2003, Section 2.2.1) was used in selecting the fixed value of the irreversible colloid fast fraction, as described in *Saturated Zone Colloid Transport* (BSC 2004, Section 6.6). As noted in the statement of the RAI, the fixed value of fast fraction of irreversible colloids used in TSPA transport abstractions is 0.00168. Table 6-4 of *Saturated Zone Colloid Transport* (BSC 2004, p. 6-18[a]) gives the fast fraction (termed "Unretarded Fraction, colfrac" in the table) as a function of the travel time. The value of 0.00168 corresponds to an interpolated travel time value of approximately 52 years. This is the combined travel time through the unsaturated and saturated zone in the lower natural barrier. The median value of travel time through the saturated zone alone among all realizations of the glacial-transition climatic conditions for fast fraction of irreversible colloids, as given in Table 6-10[a] of *Saturated Zone Flow and Transport Model Abstraction* (SNL 2008a) is 60 years. Hence the value of 52 years for the combined unsaturated zone-saturated zone travel time is a conservative choice.

In addition to the aforementioned use of a conservative value for the fixed value of the irreversible fast fraction, a risk-informed analysis given below shows that the contribution of fast irreversible colloids to plutonium mass releases and plutonium dose (and therefore to total dose), is insignificant. Figure 8.1-3[a] of *Total System Performance Assessment Model/Analysis for the License Application* (SNL 2008c) shows that for 10,000 years and post-10,000 years, the Seismic Ground Motion and Igneous Intrusion Modeling Cases are the most important contributors to total mean annual dose. Mass releases from the saturated zone in the first 10,000 years for ^{239}Pu irreversibly

attached to the "slow fraction" of colloids for the Igneous Intrusion Modeling Case are given in Figure K6.5.1-1, and the contribution of the ^{239}Pu irreversibly attached to the fast fraction of colloids for the same modeling case and time frame is given in Figure K6.5.1-4 of *Total System Performance Assessment Model/Analysis for the License Application* (SNL 2008c, Appendix K). Similar results for the post-10,000 years saturated zone releases for the Igneous Intrusion Modeling Case for the slow colloids are given in Figure K6.5.2-1, and those for fast fraction of colloids are given in Figure K6.5.2-2 of *Total System Performance Assessment Model/Analysis for the License Application* (SNL 2008c, Appendix K). For the Seismic Ground Motion Modeling Case, the 10,000-year saturated zone mass release rate for ^{239}Pu irreversibly attached to slow colloids is given in Figure K7.5-1, and that for the fast fraction of colloids for the same modeling case and time frame is given in Figure K7.5-2 of *Total System Performance Assessment Model/Analysis for the License Application* (SNL 2008c, Appendix K). Comparison of these pairs of figures shows that the release fraction resulting from the fast fraction of colloids is about 500 times smaller than that resulting from the slow colloids (corresponding to the fast fraction ratio of 0.00168). Since the biosphere dose conversion factor (BDCF) is the same regardless of how the plutonium is transported through the groundwater, the Pu doses from these two types of colloids will also be in this ratio. Similar conclusions apply to other isotopes of Pu as well. This shows that the dose from the fast fraction is insignificant when represented with a conservative fixed value; therefore, it does not need to be modeled by an uncertainty distribution.

Finally, Table 6-4 of *Saturated Zone Colloid Transport* (BSC 2004, p. 6-18[a]) gives the highest value of the unretarded fraction as 0.00932 (corresponding to a travel time of 1 year), which is about 5.5 times larger than the value of 0.00168 used in the TSPA calculations. Even if this extreme value of 0.00932 were used in the dose calculations, the contribution due to the fast fraction would still be smaller than that of the slow fraction by a factor on the order of 100. This further confirms that the dose from the fast fraction is insignificant when represented with a conservative fixed value, and, therefore, it does not need to be modeled by an uncertainty distribution.

Note: SAR (Sections 2.3.8.5.2.5, 2.3.8.6, and 2.3.9.3.2.3.5) states that the value for the fast fraction corresponds to a 100-year transport time based on the parent document of *Saturated Zone Colloid Transport* (BSC 2004). This value will be revised to show a fast fraction value time of approximately 52 years to be consistent with ERD 01 of that document. The SAR updates will be reflected in a future license application update.

2. COMMITMENTS TO NRC

DOE commits to update the license application as described in Section 3. The changes to be made to the license application will be included in a future license application update.

3. DESCRIPTION OF PROPOSED LA CHANGE

SAR, Sections 2.3.8.5.2.5, p. 2.3.8-65; 2.3.8.6, p. 2.3.8-81; and 2.3.9.3.2.3.5, pp. 2.3.9-77 and 2.3.9-78 will be modified to state that the value of the fast fraction corresponds to an

interpolated 52-year transport time. The changes to be made to the license application will be included in a future license application update.

4. REFERENCES

BSC (Bechtel SAIC Company) 2004. *Saturated Zone Colloid Transport.* ANL-NBS-HS-000031 REV 02. Las Vegas, Nevada: Bechtel SAIC Company. ACC: DOC.20041008.0007; DOC.20051215.0005; LLR.20080527.0086.

NRC (U.S. Nuclear Regulatory Commission) 2003. *Yucca Mountain Review Plan, Final Report.* NUREG-1804 REV 02. Washington, D.C.: U.S. Nuclear Regulatory Commission, Office of Nuclear Material Safety and Safeguards.

SNL (Sandia National Laboratories) 2008a. *Saturated Zone Flow and Transport Model Abstraction.* MDL-NBS-HS-000021 REV 03 AD 02. Las Vegas, Nevada: Sandia National Laboratories. ACC: DOC.20080107.0006; LLR.20080408.0256.

SNL 2008b. *Particle Tracking Model and Abstraction of Transport Processes.* MDL-NBS-HS-000020 REV 02 AD 02. Las Vegas, Nevada: Sandia National Laboratories. ACC: DOC.20080129.0008; DOC.20070920.0003; LLR.20080325.0287; LLR.20080522.0170.

SNL 2008c. *Total System Performance Assessment Model/Analysis for the License Application.* MDL-WIS-PA-000005 REV 00 AD 01. Las Vegas, Nevada: Sandia National Laboratories. ACC: DOC.20080312.0001; LLR.20080414.0037; LLR.20080507.0002; LLR.20080522.0113.

RAI Volume 3, Chapter 2.2.1.3.7, First Set, Number 13:

Describe how the UZ transport model represents the transport of irreversible colloids in the matrix after they are admitted there by advective transport from fractures.

Basis: DOE excludes matrix diffusion of irreversible colloids, but the colloid size exclusion process allows a fraction of small colloids to enter the matrix advectively under some conditions. It is not apparent how the transport of irreversible colloids in the matrix is implemented by the UZ transport model, particularly with respect to colloid filtration at matrix-matrix interfaces. The information is needed to verify compliance with 10 CFR 63.114(a) and (b).

1. RESPONSE

This response describes how the unsaturated zone transport model represents the transport of irreversible colloids in the matrix after they are admitted there by advective transport from fractures, based on a synthesis of existing information in SAR Sections 2.3.7 and 2.3.8, *Radionuclide Transport Models Under Ambient Conditions* (SNL 2007a), *EBS Radionuclide Transport Abstraction* (SNL 2007b), *Total System Performance Assessment Model/Analysis for the License Application* (TSPA-LA) (SNL 2008a), and *Particle Tracking Model and Abstraction of Transport Processes* (SNL 2008b).

1.1 DESCRIPTION OF TRANSPORT OF IRREVERSIBLE COLLOIDS FROM EBS TO THE UNSATURATED ZONE

Once irreversible colloids are released from the EBS, they may be transported either by advection or diffusion into the fractures and matrix of the unsaturated zone, which is conceptualized as a dual continuum. Models used for these transport processes are presented in SAR Section 2.3.7.12. Advection is the more important transport mechanism, since the diffusion coefficient of colloid particles is generally small compared to the diffusion coefficient of dissolved radionuclides (SNL 2007b, Section 6.3.4.4). In areas of seepage, the irreversible colloid release from the EBS is dominated by advective transport from the invert into the fractures of the unsaturated zone at the base of the invert.

1.2 DESCRIPTION OF TRANSPORT OF IRREVERSIBLE COLLOIDS IN THE UNSATURATED ZONE

As described in TSPA-LA (SNL 2008a, Section 6.3.9.1), colloid transport in the unsaturated zone is primarily within the fractures because colloids are limited in their capacity to diffuse into rock matrix as reflected in the low values for diffusion coefficients (SNL 2007a, Section 6.18.2). In the unsaturated zone transport model, diffusion of colloids between the fractures and rock matrix is conservatively assumed to be negligible, while advective transport between the fractures and rock matrix is modeled explicitly. In particular, colloids can be transported between fractures and the rock matrix and through the rock matrix by advection as long as the colloids are smaller than matrix pores. However, if the colloid particles are larger than the matrix pores, then

colloid transport into the rock matrix is limited by size exclusion. Thus, when there is a component of flow from the fractures into the matrix, some colloids that would otherwise migrate from the fracture continuum to the matrix continuum are excluded due to their size relative to the matrix pore size. This colloid size-exclusion process is implemented for irreversible colloids in the TSPA-LA model through the use of an exclusion factor, fc, based on the percentage of pores that are smaller than the expected colloid size of 0.1 μm (100 nm) (SNL 2008a, Section 6.5.10). Each colloid particle has a chance of being excluded from entering the matrix based on a probability, equal to the fraction of matrix pores that are smaller than the expected colloid size. The colloid exclusion factors used in the TSPA-LA model are presented in Table 6.3.9-10 of *Total System Performance Assessment Model/Analysis for the License Application* (SNL 2008a).

Irreversible colloids can also travel by advection (but not diffusion) back into the fractures, if the flow is in the direction of matrix to fractures. This happens at interfaces where a matrix-dominated flow situation transitions to fracture-dominated flow in the model. No filtration of colloid particles based on particle size versus pore size occurs in the rock matrix units or between the rock matrix units (SNL 2008b). DOE takes no credit for colloid filtration within a matrix or at matrix-matrix interfaces. Those irreversible colloid particles (and their imbedded or attached radionuclides) that remain within the rock matrix units will travel at the matrix pore velocity. Furthermore, the irreversible colloids filtered by size exclusion at the fracture-matrix interface remain in the aqueous phase in the unsaturated zone fractures.

As described above, size exclusion from fractures to matrix is treated on the basis of effective colloid and matrix pore diameters, where a colloid is excluded from entry into a pore that is smaller than the colloid. The matrix pore size distributions for different rock types were developed from moisture retention curve measurements on rock matrix samples taken from 16 different hydrogeologic units between the repository host rock and the water table at Yucca Mountain (SNL 2008b). The pore-size distribution data for each hydrogeologic unit were compared to the average effective colloid diameter of 0.1 μm (100 nm), giving the expected fraction of colloids excluded from entering the rock matrix in that unit.

2. COMMITMENTS TO NRC

None.

3. DESCRIPTION OF PROPOSED LA CHANGE

None.

4. REFERENCES

SNL (Sandia National Laboratories) 2007a. *Radionuclide Transport Models Under Ambient Conditions.* MDL-NBS-HS-000008 REV 02 ADD 01. Las Vegas, Nevada: Sandia National Laboratories. ACC: DOC.20050823.0003; DOC.20070718.0003; DOC.20070830.0005; LLR.20080324.0002.

SNL 2007b. *EBS Radionuclide Transport Abstraction.* ANL-WIS-PA-000001 REV 03. Las Vegas, Nevada: Sandia National Laboratories. ACC: DOC.20071004.0001; LLR.20080414.0023.

SNL 2008a. *Total System Performance Assessment Model/Analysis for the License Application.* MDL-WIS-PA-000005 REV 00 ADD 01. Las Vegas, Nevada: Sandia National Laboratories. ACC: DOC.20080312.0001; LLR.20080414.0037; LLR.20080507.0002; LLR.20080522.0113.

SNL 2008b. *Particle Tracking Model and Abstraction of Transport Processes.* MDL-NBS-HS-000020 REV 02 AD 02. Las Vegas, Nevada: Sandia National Laboratories.
ACC: DOC.20080129.0008; DOC.20070920.0003; LLR.20080325.0287; LLR.20080522.0170.

RAI: Volume 3, Chapter 2.2.1.3.7, First Set, Number 14:

Provide details for how DOE selected the range of $K_{d,coll}$ values that are used to model sorption of radionuclides onto montmorillonite/smectite.

Basis: The colloid sorption coefficients ($K_{d,coll}$) for reversible sorption of Pu and Am onto smectite differ by several orders of magnitude from those used to model sorption of Pu and Am onto the matrix of identified rock types in the UZ transport model. Provide additional information about the technical basis for the selection of the $K_{d,coll}$ distribution of values, including, if relevant, the information reported in "Colloidal Sorption Coefficients for Pu, Am, Th, Cs, and Pa" (DOE Data Tracking No. MO0701PASORPTN.000). The information is needed to verify compliance with 10 CFR 63.114(a) and (b).

1. RESPONSE

The method of selection of the colloid sorption coefficient ($K_{d,coll}$) ranges is explained and cited in Section 1.1 with an emphasis on the selection of the ranges for plutonium and americium. The ranges for plutonium and americium are compared in Section 1.2.1 to the sorption ranges selected for tuff in the unsaturated zone. Reasons for the differences in sorption ranges are provided in Section 1.2.2.

The basis of the NRC request is that the $K_{d,coll}$ ranges used for plutonium and americium are much different than the tuff K_d ranges used in the unsaturated zone transport model. To address this basis statement these differences are analyzed and discussed in detail for plutonium and americium. This level of detail is not presented for the other radionuclides identified in the basis (thorium, cesium, and protactinium) because they appear to be included in the RAI only because they are in the title of the cited reference where additional information is requested if relevant and because the RAI is focused more generally on the technical basis for the selection of the ranges rather than the selection of the ranges for each radionuclide.

1.1 RADIONUCLIDE SORPTION ONTO GROUNDWATER COLLOIDS

Groundwater seepage colloids are modeled as particles of montmorillonite, a smectite clay (SAR Section 2.3.7.11.2.3). "Montmorillonite" and "smectite" are terms that are used interchangeably in this model and in this response. Sorption onto montmorillonite colloids is modeled as linear and reversible (SAR Section 2.3.7.11.3). The concentration of each radionuclide sorbed to these colloids is estimated based on the value of an effective distribution coefficient ($K_{d,coll}$), which is typically estimated from laboratory measurements as discussed below. The $K_{d,coll}$ value represents a constant ratio of sorbed concentration to aqueous concentration that is independent of the aqueous concentration. Thus, as $K_{d,coll}$ increases, the radionuclide fraction sorbed to the colloids increases.

1.1.1 Method of Selection of Sorption Ranges

The relevant information and $K_{d,coll}$ values documented in "Colloidal Sorption Coefficients for Pu, Am, Th, Cs, and Pa" (DTN: MO0701PASORPTN.000) and used in the TSPA-LA model are based on project data, literature data, and professional judgment (as stated in the *Readme.doc* file of DTN: MO0701PASORPTN.000). The degree of professional judgment depended on the availability of data for each radionuclide. Factors considered during the selection of the $K_{d,coll}$ ranges included the availability of sorption data for the specific radionuclide, the qualification of the available data, and, if adequate data were unavailable, the appropriateness of data from analogues.

The $K_{d,coll}$ distributions presented in Table 1-3 of DTN: MO0701PASORPTN.000 for plutonium, americium, thorium, protactinium, and cesium consist of four to six intervals. The range of each distribution was intended to cover the entire range of the available data (SNL 2007a, p. 6-59). Emphasis was placed on the higher intervals of the distributions for two reasons. First, the data used in the analyses included data for colloids as well as larger particles; it is believed that K_d values for colloids (i.e., $K_{d,coll}$ values) are higher than K_d values for larger particles due to the higher specific surface area of colloids (SNL 2007a, p. 6-59). Second, measured K_d values tend to overpredict desorption over time (i.e., they underpredict retention by colloids) (SNL 2007a, p. 6-59). For example, redox changes can result in the irreversible association of plutonium with some mineral surfaces. In the case of plutonium, the upper bound of the $K_{d,coll}$ distribution was lowered because of the potential of oxide precipitation on the surface (SNL 2007a, p. 6-62).

1.1.2 Plutonium Sorption Range

Qualified Pu(IV) and Pu(V) sorption distribution coefficient data measured at 2,880 minutes (48 hours) of contact or longer range from 3.2×10^3 to 1.4×10^6 mL/g. These data are plotted as a cumulative distribution function (CDF) in Figure 2.3.7-41a of the SAR.

The range of $K_{d,coll}$ for plutonium was set at 10^3 to 10^5 mL/g (SAR Table 2.3.7-23). This range overlaps the range of measurements in the CDF but is offset to lower bounds. As stated above, the maximum value was reduced due to the potential for precipitation of oxides on the colloid surfaces in the experiments (SNL 2007a, p. 6-62). This selected lower range, however, is higher in comparison to other project and independent data where precipitation on the surfaces is not suspected. Project measurements of plutonium-montmorillonite colloid K_d values range from 1.6×10^3 to 2.7×10^4 mL/g. In addition, an independently estimated range for Pu(V) $K_{d,coll}$ for groundwater colloids in the vicinity of Yucca Mountain is 9×10^2 to 2×10^4 mL/g (SAR Table 2.3.7-24). These data support the plutonium $K_{d,coll}$ range selected for the model.

1.1.3 Americium Sorption Range

Qualified project data for americium sorption onto montmorillonite colloids after ten days of contact was measured on colloid concentrations ranging from 10 to 1,000 mg/L. They are plotted as a CDF in Figure 2.3.7-41a of the SAR. The minimum and maximum measurements are 1.9×10^4 and 1.5×10^6 mL/g.

The selected range of the americium $K_{d,coll}$ was set at 10^4 to 10^7 mL/g (SAR Table 2.3.7-23). This range is also used for thorium and protactinium because qualified data for thorium and protactinium, which have adsorption similarities to americium, were limited (SNL 2007a, Section 5.1). The upper limit of this range was set to a value nearly ten times higher than the maximum americium measurement to account for increased sorption of thorium (SNL 2007a, Section 5.1).

The selected $K_{d,coll}$ range of 10^4 to 10^7 mL/g for americium (and thorium and protactinium) is supported by additional data for different temperatures and desorption. The overall range of these additional data is 1.8×10^4 to 2.7×10^5 mL/g.

Independent data from the literature also support the selected range. An independently estimated range for Am(III) $K_{d,coll}$ for groundwater colloids in the vicinity of Yucca Mountain is 10^4 to 10^7 mL/g (SAR Table 2.3.7-24), which is identical to the TSPA-LA range selected. In addition, thorium and protactinium sorption onto montmorillonite is within the 10^4 to 10^6 mL/g range, as shown in Figure 2.3.7-41a of the SAR.

1.2 COMPARISON TO SORPTION ON TUFF

1.2.1 Sorption on Tuff

The K_d values used for the rock matrices in the unsaturated zone were measured on tuff samples that were crushed and sieved to produce 75- to 500-µm fractions (SNL 2007b, Section A5). These samples were classified into three rock types: zeolitic tuff, devitrified tuff, and vitric tuff (SNL 2007b, Section A2). Because there are uncertainties in project and literature *Kd* value measurements, uncertainties were incorporated into the model distributions with a conservative bias toward the low ends of the data ranges (SNL 2007b, Section A6). Limiting the upper range of the tuff K_d distributions is conservative because lower *Kd* values increase the mobility of radionuclides in the geosphere, which increases the calculated dose to the biosphere.

For plutonium sorption on tuff, the range of the measured K_d values is approximately 10^1 to 10^4 mL/g (SNL 2007b, Figures in Section A8.4). However, to ensure the values were conservative, the range was set to 10^1 to 2×10^2 mL/g for each of the rock types (SAR Table 2.3.8-2).

For americium sorption on devitrified tuff, the range of the measured K_d values is approximately 10^2 to 10^4 mL/g (SNL 2007b, Figures in Section A8.1.1). For sorption onto zeolitic tuff, the measured americium K_d range is approximately 10^3 to 10^5 mL/g (SNL 2007b, Figures in Section A8.1.2). For vitric tuff, the measured K_d range is approximately 10^3 to 10^6 mL/g (SNL 2007b, Figures in Section A8.1.3). In comparison, the ranges of the selected K_d distributions for these rock types are 10^3 to 10^4 mL/g for devitrified and zeolitic tuff and 10^2 to 10^3 mL/g for vitric tuff (SAR Table 2.3.8-2). The maximum values of each of these tuff K_d distributions is conservative relative to the data.

1.2.2 Explanation for Modeled Sorption Differences

The K_d distributions used in the TSPA-LA model for plutonium and americium onto colloids and tuff are compared in Table 1-1. As noted in the RAI, the ranges are much higher for colloid sorption than for sorption to tuff.

There are two major reasons for this large difference. First, the ranges of the data (Sections 1.1.2 and 1.1.3) show that in general, the colloid K_d measurements ($K_{d,coll}$) are larger than the tuff K_d measurements. The larger K_d measurements for the colloids are likely primarily due to differences in specific surface areas. Montmorillonite has a specific surface area in the range of 10 to 100 m^2/g while specific surface area measurements of the devitrified, zeolitic, and vitric tuff samples are in the range of 1 to 30 m^2/g.

The second major reason for the differences in the colloid and tuff K_d distributions in Table 1-1 is the bias of the tuff K_d values toward conservatism (Section 1.2.1). Bias toward lower K_d distributions for tuff is conservative because sorption to tuff will decrease the mobility of radionuclides in the geosphere.

Table 1-1. Comparison of Plutonium and Americium K_d Ranges Used for Colloids and Tuff

Parameter	Sorbent	Plutonium	Americium
$K_{d,coll}$ (mL/g)	Smectite colloids	10^3 to 10^5	10^4 to 10^7
K_d (mL/g)	Zeolitic tuff Devitrified tuff	10^1 to 2×10^2	10^3 to 10^4
K_d (mL/g)	Vitric tuff	10^1 to 2×10^2	10^2 to 10^3

Source: SAR Tables 2.3.7-23 and 2.3.8-2

1.3 SUMMARY

Details are provided in Section 1.1 for how DOE selected the range of $K_{d,coll}$ values that are used to model sorption of radionuclides onto montmorillonite/smectite. The general methodology is presented in Section 1.1.1. Because the NRC request specifically points out the differences in the selected ranges of $K_{d,coll}$ for plutonium and americium compared to the selected sorption ranges onto rock types of the unsaturated zone (tuff), specifics for the selection of the $K_{d,coll}$ ranges of these radionuclides are provided in Sections 1.1.2 and 1.1.3. In Section 1.2.1 these ranges are compared to the selected tuff K_d ranges for plutonium and americium, and in Section 1.2.2 reasons for the larger values of the $K_{d,coll}$ ranges are provided.

2. COMMITMENTS TO NRC

None.

3. DESCRIPTION OF PROPOSED LA CHANGE

None.

4. REFERENCES

MO0701PASORPTN.000. Colloidal Sorption Coefficients for Pu, Am, Th, Cs, and Pa. Submittal date: 04/17/2007.

SNL (Sandia National Laboratories) 2007a. *Waste Form and In-Drift Colloids-Associated Radionuclide Concentrations: Abstraction and Summary*. MDL-EBS-PA-000004 REV 03. Las Vegas, Nevada: Sandia National Laboratories. ACC: DOC.20071018.0019; LLR.20080325.0281.

SNL 2007b. *Radionuclide Transport Models Under Ambient Conditions*. MDL-NBS-HS-000008 REV 02 ADD 01. Las Vegas, Nevada: Sandia National Laboratories.
ACC: DOC.20050823.0003; DOC.20070718.0003; DOC.20070830.0005; LLR.20080324.0002.